Master thesis: Investigation into the preparation of supported nickel nanoparticles for CO_2 hydrogenation via colloidal synthesis

February 15, 2022

A master thesis by Just Pé Jonasse
Daily supervisors: Nienke Visser & Dr. Oscar Daoura
First Examiner: Dr. Jessi van der Hoeven
Second Examiner: Prof. Dr. Petra de Jongh

Utrecht University

Department of Chemistry
Material Chemistry and Catalysis
Debeye Institute for Nanomaterials Science
University Utrecht
Netherlands

Abstract

The conversion of CO_2 into CH_4 using H_2 can become an important part of the reduction of our carbon footprint, turning a 'waste' molecule into a usable feedstock. This reaction can be catalysed by nickel (Ni) nanoparticles (NPs). The behaviour of supported nickel catalysts depends on many factors, such as nickel nanoparticle size and the type of support used [1]. The preparation of monodisperse Ni nanoparticle catalysts with well-defined particle sizes on various types of supports is difficult using standard catalyst preparation methods, thereby hampering our understanding and the development of Ni catalysts for CO_2 hydrogenation. A promising approach to address these challenges is the use of colloidal synthesis, where the metal nanoparticles are prepared separately before depositing them on a support [2]. This thesis demonstrates the successful application of colloidal synthesis to prepare Ni nanoparticles supported on several materials.

Control over the size of Ni nanoparticles is typically achieved using phosphorous containing ligands. However, these ligands are difficult to remove from the Ni NP surface even at high temperatures (500 °C) and phosphorous often is incorporated in the Ni nanoparticles. In this work we present the synthesis of phosphorous-free Ni nanoparticles via colloidal synthesis. Using a literature procedure, monodisperse phosphorous-free Ni nanoparticles of 4 and 7 nm were synthesized suspension using a seed-mediated approach by reduction of $Ni(acac)_2$ using a borane tert-butylamine complex [3]. The Ni NPs dispersed in toluene were deposited on a carbon or silica support via sonication-assisted deposition and rapidly dried. 4.2 ± 0.9 nm Ni/SiO_2, 4.9 ± 0.8 nm Ni/C, 8.8 ± 2.8 nm Ni/SiO_2 and 8.0 ± 1.7 nm Ni/C were successfully obtained in this manner. A mild thermal treatment was developed in this thesis, comprising a calcination step in O_2 at 250 °C and a subsequent reduction step in H_2 at 350 °C. Successful ligand removal on both support types was confirmed by IR spectroscopy and TGA-MS. Oxidation and reduction behaviour of the Ni NPs was extensively investigated using (*in situ*) TEM, TPR and XRD.

Catalytic activity and catalyst stability were tested for Ni/SiO_2 and Ni/C during high pressure CO_2 hydrogenation at 30 bar and at temperatures varying from 240 °C to 340 °C, revealing much higher activities for silica support Ni NPs compared to carbon supported nanoparticles. Significant sintering was observed for the Ni NPs supported on SiO_2, leading to Ni NPs of up to 100 nm. A comparable colloidal synthesis using TOP was performed to investigate the potential difference caused by changing this ligand. This resulted in the formation of nanoparticles containing phosphorous, which were not active for the reaction. This again illustrates the importance of developing a synthesis method to created Ni nanoparticles without using phosphorous containing ligands.

To conclude, our methodology can be extended to other supports, and allows detailed investigations of the Ni nanoparticle size- and support effects on the catalytic conversion of CO_2 to CH_4.

List of commonly used abbreviations

2θ	Bragg angle (°)
BET	Brunauer-Emmett-Teller
IWI	Incipient wetness impregnation
Ni	Nickel
NiO	Nickel oxide
NP	Nanoparticle
GNP	Graphene nanoplatelets
EDX	Energy-dispersive X-ray spectroscopy
GHSV	Gas Hourly Space Veloctiy (mL g^{-1} h^{-1})
HAADF-STEM	High-angle annular dark field scanning transmission electron microscopy
P	Phosphorous
TEM	Transmission electron microscopy
TPR	Temperature programmed reduction
TGA	Thermogravimetric analysis
MS	Mass spectrometry
BTB	borane *tert*-butylamine complex
IR	Infrared spectroscopy
XRD	X-ray diffraction
S	Supersaturation
TOP	trioctylphosphine
ODE	1-octadecene
OAm	Oleylamine
OAc	Oleic acid
Ni(acac)$_2$	Nickel(II)acetylacetonate
RPM	Revolutions per minute
wt-%	Weight loading (%)
ICP-OES	Inductively coupled plasma - optical emission spectrometry

Contents

Chapter 1

Introduction

In the modern world, the chemical industry is indispensable. A common type of material used in this industry is the catalyst. In its simplest sense, a catalyst is a material which enables a more favourable reaction mechanism for reactants to form their product, while the catalysts themselves remain unaltered. Of the products produced in chemical industry, at least 85 % has seen a catalyst during their processes [4,5]. Modern catalytic processes typically make use of nanomaterials. In the case of heterogeneous catalysis, these materials often consist of metallic nanoparticles supported on support materials, typically metal oxides. A gas or liquid feed of reactants is passed over these materials, yielding a desired product [2]. Chemical research towards heterogeneous catalysis typically focusses on developing and understanding catalysts, as well as the processes that occur on their surface [2].
One such process is the hydrogenation reaction of carbon dioxide (CO_2) to methane (CH_4). This reaction, known as the Sabatier reaction, could prove to be a highly interesting reaction to convert a molecule commonly regarded as waste, into a highly useful chemical CH_4, typically used as an energy carrier. This could be a useful application for intermittent energy sources like solar and wind power in addition to hydrogen (H_2). At the same time, this will allow us to make use of the existing energy grid [6,7]. Methanation of CO_2 is usually performed using a nickel (Ni) catalyst, although other metals, such as ruthenium (Ru) and Rhodium (Rh), are also used [1,8–12]. The main advantage of Ni over these metals is its price, and relative abundance in the earth's crust [13,14]. However, the reaction is energetically unfavourable, and much more research needs to be done to result in an economically feasible way to convert CO_2 into CH_4. Finding a way to understand this reaction in detail might help reach the goal of running affordable methanation reactions.
The mechanism of methanation is not yet understood, and the possible mechanisms are thought to be determined by the type of catalysts, including metallic particle size and shape [1,15–23]. Another factor is the potential effect of the support material itself. The mechanism is thought to proceed through either a carbon monoxide (CO) or via a formate intermediate ($COOH^-$) [1,19,20,24]. Taking into account these many possible parameters that can influence the mechanism, methods need to be developed to consistently and reproducibly synthesize catalysts with well defined metallic nanoparticles of various sizes on various supports. This is a significant challenge.
Colloidal synthesis is a method which can be used to prepare well-defined nanoparticles in suspension. These particles can be deposited onto various support materials, whilst maintaining their size and shape [2,25]. Using this approach, the effects of particle size and support materials might be further elucidated. However, methods for developing catalysts in this manner are not yet optimized. In the case of colloidal Ni NP synthesis, typically phosphorous containing ligands are used [26,27]. These phosphorous-containing ligands can introduce several issues in catalysts synthesis [27]. Phosphide can be incorporated into the Ni lattice, which is very difficult to remove [27]. This prevents study of the desired Ni NPs. Therefore, preparation of phosphorous-free colloidal Ni NPs, their deposition on different supports and an investigation into their catalytic performance are highly interesting for understanding CO_2 methanation.

First, the fundamental aspects of CO_2 methanation will be discussed, to illustrate the necessity for the synthesis of well-defined particles in different shapes. Then, an introduction to colloidal synthesis is given in addition to existing examples for Ni colloids from literature. Finally, the research aims of this thesis are summarized.

1.1 Fundamentals of CO_2 methanation

The Sabatier reaction, discovered by Paul Sabatier and Jean-Baptiste Senderens in 1897, is the reaction of CO_2 and H_2 at elevated temperatures and pressures to form CH_4 and H_2O and is otherwise known as CO_2 methanation [13]. The reaction, shown in Equation (1.1), can be viewed as a combination of the reverse water-shift reaction (RWGS) and the CO methanation reaction, shown in Equations (1.2) and (1.3), respectively [13].

$$CO_2 + 4H_2 \rightarrow CH_4 + 2H_2O \qquad \Delta H = \text{-164 kJ mol}^{-1} \text{ (at 298 K)} \tag{1.1}$$

$$CO_2 + H_2 \rightarrow CO + H_2O \qquad \Delta H = 41 \text{ kJ mol}^{-1} \text{ (at 298 K)} \tag{1.2}$$

$$CO + 3H_2 \rightarrow CH_4 + H_2O \qquad \Delta H = \text{-206 kJ mol}^{-1} \text{ (at 298 K)} \tag{1.3}$$

1.1.1 Reaction mechanism

The reaction mechanism for CO_2 methanation over catalysts is still under debate and so far two major potential pathways are proposed for this reaction. These two pathways can generally be separated based on their main intermediate. The first pathway concerns the conversion of adsorbed CO_2 into a CO intermediate via the reverse water gas shift reaction (Equation (1.2)). The adsorbed CO is then either further dissociated to C and then hydrogenated to CH_4, or it is directly hydrogenated to CH_4. The second pathway concerns the conversion of the CO_2 into an adsorbed formate intermediate [1,19,28,29]. The nature of the support materials appears to have a significant influence on both the performance of the catalysts, as well as the dominant reaction mechanism [24,28,30–34]. Ilsemann et al investigated Ru catalysts supported on a variety of metal oxides for the hydrogenation of CO_2 and showed a dependence on surface basicity, with TiO_2 and ZrO_2 as non rare earth metal oxides performing best [31]. Liang et al investigated the influence of basic/acid sites on various Ni catalysts and demonstrated that Ni/SiO_2 performed best in CO_2 methanation in the presence of medium basic sites, similar to what Ilsemann et al found for Ru catalysts [35]. This is a result of strong adsorption of CO_2 on these basic sites [28].

In addition, the structure and size of the nanoparticles used also appears to influence the activity and reaction mechanism [1,15,23,36]. For example, Lin et al demonstrated the superior activity of 8 nm Ni nanoparticle supported on CeO_2 compared to 4 and 2 nm nanoparticles [23]. Vogt et al demonstrated that the particle diameter of Ni nanoparticles supported on SiO_2 influenced the reaction mechanism and activity [1]. However, Beierlein et al claimed that CO_2 methanation over 14-88 Ni wt-% Ni/Al_2O_3 catalysts was independent of metal-support interactions and nanoparticle size [37].

To summarize, the CO_2 methanation reaction mechanism over Ni-based catalysts is not completely understood and appears to be highly influenced by support material and the structure and size of the active metal used [28]. Therefore, the development of well-defined catalyst systems is necessary to further elucidate this reaction mechanism.

1.1.2 Thermodynamics & kinetics

Equilibrium compositions at various temperatures and pressures calculated using HSC Chemistry illustrate the influence of these parameters on the equilibrium composition of the reaction. Shown in Figure 1.1a is the simulated equilibrium composition in mol-% of the reactions as a function of pressure at 300 °C, showing a higher CH_4 content for higher pressures. Figure 1.1b shows the equilibrium composition as a function of temperature at 30 bar, where CH_4 content decreases as a function of temperature. A comparison with calculations found in literature shows similar trends and compositions [38,39]. Gao et al, Sahebdelfar et al and the calculations performed with HSC Chemistry all indicate CH_4 selectivities close to 100% at 300 °C and 30 bar and CO_2 conversion of >95%, indicating that these are suitable reaction conditions for this reaction [38,39]. Although lower temperatures appear to be even better in this regard, an additional consideration needs to be made. Kinetics have a strong influence on the attainable CH_4 production, as studied extensively over commercial supported Ni catalysts [40,41]. Schmider et al found a rapid increase in CO_2 conversion from 5% at 500 K to about 95% at 600 K, illustrating the need for sufficiently high temperatures for CO_2 methanation [40].

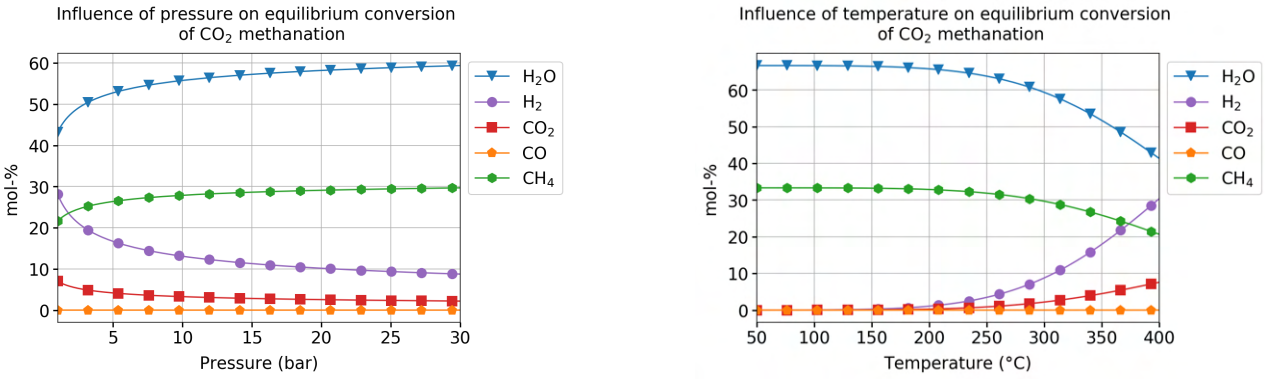

(a) (b)

Figure 1.1: HSC Chemistry equilibrium compositions of CO_2 methanation at variable pressures and temperatures. Calculations were performed with 1 kmol of CO_2 and 4 kmol of H_2 for 200 iterations with no inert gas present. a) Pressure influence on equilibrium composition at 300 °C. b) Temperature influence on equilibrium composition at 30 bar.

1.1.3 Catalyst materials

As briefly mentioned in Section 1.1.2, sufficiently high temperatures are necessary to obtain high CO_2 conversions [40,41]. Another method through which conversion can be improved is by using a catalyst material. Reactions such as the Ni-catalysed Sabatier reaction typically occur on the surface of metal particles [2]. Therefore, obtaining a high surface area of active metal usually results in high activity. Contemporary catalyst research focusses on developing well-defined nanoparticles with a high surface area. However, these small particles are significantly less stable than their larger counterparts due to the relatively high surface-to-volume ratio and thus require some sort of stabilization [2,25]. In a typical catalyst used for heterogeneous catalysis, small metal nanoparticles are anchored onto a material that is known as a support material. A support material is used to stabilize the smaller metal nanoparticles and allows for the use of the high surface area of the small nanoparticles at elevated temperatures and pressures [2].

Vannice et al determined the active metals that can be used for CO_2 and CO methanation, which include many of the group VIII elements [42]. The relative activity and selectivity orders of the various metals for CO_2 methanation are shown below [42]:

$$\begin{aligned} &Activity: && Ru > Fe > Ni > Co > Rh > Pd > Pt > Ir \\ &Selectivity: && Pd > Pt > Ir > Ni > Rh > Co > Fe > Ru \end{aligned}$$

Taking into account the relative costs of the metals, Ni-based catalysts are the most suitable materials for the Sabatier reaction as only very expensive metals such as palladium (Pd), platinum (Pt) and iridium (Ir) are more selective than Ni [42]. Additionally, Ni still has a high activity, making it the most widely used active metal in methanation catalysts [13,43,44].

Several types of Ni-based methanation catalysts are investigated in literature, including unsupported catalysts like Raney nickel [45] and supported Ni nanoparticles like those discussed in this thesis [1,3,46,47]. In the case of supported Ni nanoparticles, the materials used as a support need to have specific properties to function as an ideal support for the Sabatier reaction. These include sufficient stability under reaction conditions, so under high temperature, pressure and in the presence of water, as well as a large surface area to be able to disperse the active metal NPs and a strong enough interaction with the metal nanoparticles to anchor them to the support [44]. Support materials can also directly influence catalytic results due to these metal-support interactions [31]. For example, in the case of Ru-catalysed CO_2 methanation, the influence of Brønsted basicity of different supports on catalysis was investigated, resulting in a significantly different CH_4 yield [31]. Catalysts studied in this work consisted of similarly sized Ru nanoparticles supported on samarium oxide (Sm_2O_3), gadolinium oxide (Gd_2O_3), yttrium oxide (Y_2O_3), titania (TiO_2), ZrO_2, alumina (Al_2O_3), Magnesium oxide

(MgO) and silica (SiO_2). The authors of this work hypothesize that the presence of certain types of basic sites in some supports enhanced the CO_2 conversion and indicate the possibility of hydrogenation pathways on the support materials themselves, in addition to those taking place on the Ru nanoparticles [31]. Therefore, the choice of a suitable support for the desired application is also key in obtaining a well performing catalyst. One of the most widely used commercial catalyst support materials for methanation reactions is alumina (Al_2O_3), specifically γ-$Al2_2O_3$, due to its high surface area and excellent thermal stability [44]. However, most alumina supports suffer from limited stability in the presence of water [44]. Alternative support materials include other metal oxides, SiO_2, ZrO_2, CeO_2 and TiO_2 or different classes of materials, like carbon-based supports such as activate carbon [48], zeolites [34] and metal-organic frameworks (MOFs) [49].

Graphitic nanoplatelets

A unique support material used in this thesis are graphene nanoplatelets (GNP500) and their oxidized counterparts (Ox-GNP500), where the number 500 indicates the average BET surface area of the pristine carbon. This type of carbon has several distinct features, most prominently its large surface area of 500 m^2/g. Like many carbon-based support materials, it can also be functionalized to tune the surface properties [50–52]. Furthermore, the structure is stable at high temperatures (under inert conditions), shows resistance against acidic and basic media, have excellent thermal conductivity and allow for easy reclamation of expensive metals by burning away carbon [52]. Compared with most metal oxides typically used as support materials, like silica, titania, ceria an alumina, carbon materials typically show less reactivity and influence on catalytic processes, allowing for fundamental research [52]. A major drawback of these nanoplatelets is their limited stability under hydrogenation and oxidation conditions at high temperatures [52,53].

Silica

Silica is highly diverse material with many different variants [2,44]. Typical silica-based supports show high surface areas and exhibit excellent thermal stability, but do suffer from some instability in the presence of steam or alkaline or acidic media [2,44]. SiO_2 is also used in studies on the Sabatier reaction [1,3,13,44]. In this thesis, Davisil 643 (BET = 300 m^2/g) and Aerosil 380V (BET = 380 m^2/g), are used. These supports allow for treatments under oxidative and reductive atmospheres at higher temperatures, as well as investigation of carbon containing materials without the convolution present in GNP500.

1.2 Synthesis of supported Ni nanoparticles

Commonly used synthesis methods for the preparation of these supported nanoparticle catalysts are co-precipitation (CP), deposition precipitation (DP) and incipient wetness impregnation (IWI) [2]. All of these methods share the difficulty of controlling the nanoparticle sizes and their size distributions [2]. Additionally, it is challenging to maintain a similar nanoparticle morphology, size and size distribution across different supports. Colloidal synthesis can be used to circumvent these problems and obtain monodisperse nickel nanoparticles of varying sizes, which could then be deposited onto a support material [2,25,26]. Colloidal synthesis is a solution-based method in which precursor molecules containing the desired metal or metal ion are suddenly decomposed or reduced in the presence of stabilizing molecules [25]. This leads to rapid increase of the saturation of the solution, which in turn can lead to nucleation of the metal atoms into the core of the nanoparticles [25]. These inorganic cores are stabilized in solution by various ligands [25]. Colloidal syntheses has some advantages over the other mentioned catalyst preparation methods. The foremost advantage is the unique size and shape control that can be achieved for the particles in solution separate from the support [2,25,54,55]. These particles can then be deposited onto different support materials using a wide variety of techniques [55]. If this is done using mild deposition methods, the particles retain their shape and size, allowing for in depth comparison of the same particles on different supports [55]. However, large concentrations of colloidal nanoparticles might lead to aggregation and precipitation. A commonly used method for deposition of these particles is thus wet impregnation, to ensure sufficiently low concentration and prevent aggregation [2]. However, this can lead to drying effects, where colloids migrate to low concentration areas due to the fact that drying takes place at the surface of support materials [2]. In some cases, this can lead to inhomogeneous distribution of the nanoparticles across the support. For example, cobalt nanoparticles supported on SBA-15 showed both regions filled with nanoparticles as well as empty regions [56]. Or, in another example, iron oxide nanoparticles are distributed

across two supports, MCM-41 and a γ-Al_2O_3 support. The particles distributed well on the MCM-41, but clustered together and deposited preferentially on the external surface of the γ-Al_2O_3 support [57]. Finally, the presence of the stabilizing molecules themselves might influence the activity of the catalysts [2,25,55].

To summarize, the colloidal synthesis of metallic nanoparticles is not that straightforward. To develop methods to obtain further control of the metal nanoparticle size and shape, a fundamental understanding of colloidal synthesis is helpful. To this end, an overview of the important concepts behind colloidal synthesis is given in Section 1.2.1.

1.2.1 Synthesis of colloidal metal nanoparticles

The synthesis of colloidal NPs can be divided into three distinct stages; induction, nucleation and growth [25]. These three stages are characterized by their values for supersaturation S [25]. The evolution of S with time is shown in Figure 1.2a and the various steps involved for formation of NPs are depicted in Figure 1.2b. These

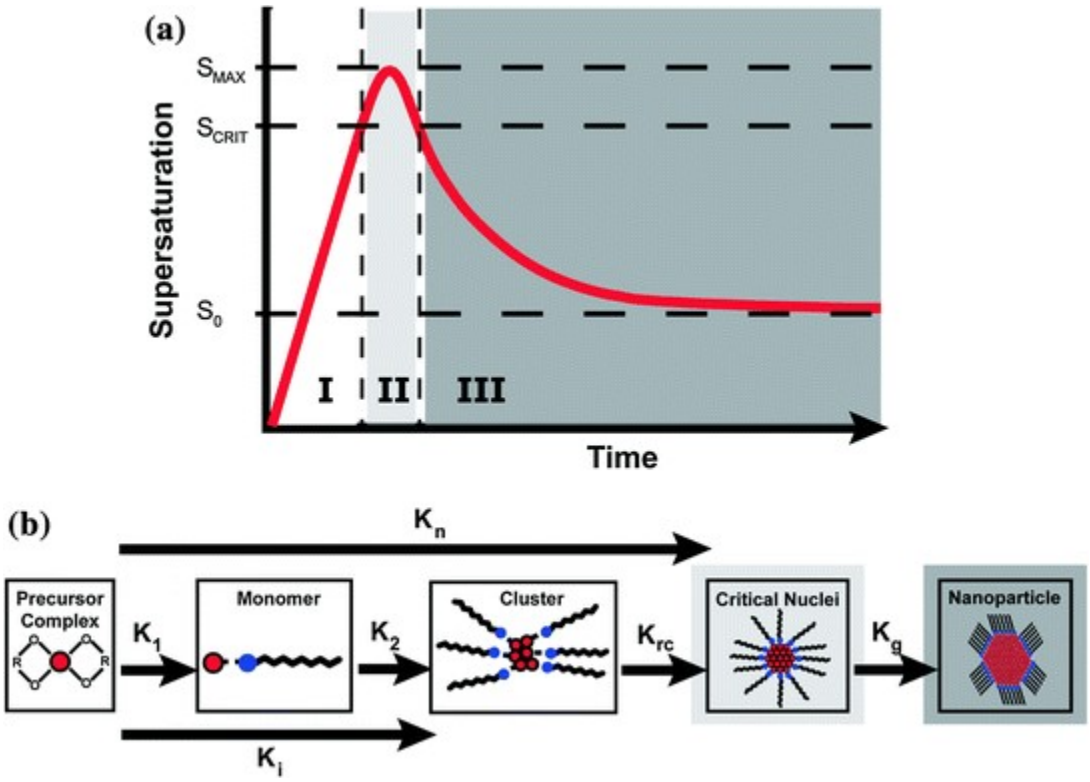

Figure 1.2: a) Figure 1.2a shows the change of the supersaturation of the solution with time. The three stages of NPs synthesis are indicated I, II III for induction, nucleation and growth respectively. S_0 indicates the solubility limit of the solutes, S_{CRIT} indicates the S level at which critical and super-critical nuclei can be formed. S_{MAX} indicates the maximum S the solution will reach before it starts to decline again. b) Here the various steps involved in NP synthesis are shown schematically, with K_1 the rate of monomer formation, K_2 the rate of cluster formation from monomers, K_{rc} the nucleation rate, K_n the effective nucleation rate and K_g the average growth rate. Reproduced from Donega et al [25].

stages will be discussed in detail below [25].

Induction stage

In this stage, first monomers are formed from the precursors. A monomer is a building block of the nanoparticles [25]. For example, in the case of synthesis of nickel NPs, a monomer could consist of a Ni^0 metal particle stabilized in solution with ligand molecules. As the monomer concentration increases, clusters of monomers

start to form and dissolve again, until a certain monomer supersaturation is reached [25]. At this point, the nucleation stage starts [25]. These two distinct steps, the formation of monomers from precursors and the formation of monomer clusters make up the induction stage [25]. Monomers can be formed from precursors following a variety of ways [55]. Here we will shortly discuss monomer formation through reduction of a metal salt and through thermal decomposition of a metal precursor complex [55].
In the case of reduction, a reductant is added to a solution of a metal precursor salt [55]. This leads to the formation of metal clusters in the presence of stabilizing molecules, as shown in equation Equation (1.4) [55].

$$xM^{n+} + nxe^{-} + stabilizer \rightarrow M^{0}_{n(cluster)} \tag{1.4}$$

Reducing agents can be varied extensively [55]. Typically, they consist of amines, carboxylic acids, alcohols, aldehydes or hydroquinones [3,58–63]. The stabilizing agents are used to prevent unwanted agglomeration of NPs and include ligands, surfactants and polymers [55]. The final size of nanoparticles synthesized using this strategy is determined by a variety of factors such as type of ligand, precursor or reducing agent, as well as temperature, reaction time and solvent used [55].
Another commonly used method to synthesize colloidal NPs is through thermal decomposition of a metal organic precursor [55].

Nucleation stage

The nucleation stage is the point at which the nuclei that are formed have equal probabilities of growth and dissolution [25]. These nuclei have certain radius, which is known as the critical radius r_C [25]. So, during the nucleation stage, nuclei with a radius r equal to or larger than r_C can be formed [25]. These nuclei can only be formed as a result of S of the solution by monomers reaching a particular critical supersaturation S_C value [25]. During the nucleation stage, precursor material is still being converted into monomers. Therefore, the monomer concentration remains high and will only start to drop when the nucleation of monomers into new nuclei consumes more monomers than are added to the solution [25]. When this happens, S starts to drop below S_C, and no more new nuclei are formed. Therefore, the length of the nucleation stage is in direct relation to the consumption and production of monomers [25]. To understand the nucleation stage and determine the important factors involved, we can use classical nucleation theory [25].
Critical nucleation theory describes nucleation using equation Equation (1.5) [25]:

$$\Delta G_{TOT} = \Delta G_V + \Delta G_S = \frac{3}{4}\pi r^3 \rho \Delta\mu + 4\pi r^2 \gamma \tag{1.5}$$

Here ΔG_{TOT} is the difference in free energy for formation of a nanoparticle nucleus from monomers in solution [25]. ΔG_V is the difference in volume free energy and is represented by $\frac{3}{4}\pi r^3 \rho \Delta\mu$, with r the radius of the crystalline NP, ρ the density of the crystalline phase and $\Delta\mu$ the difference in chemical potential between monomers in solution and in the crystalline phase [25]. ΔG_S is the difference in surface free energy and is represented by $4\pi\ r^2\gamma$, with γ the interfacial tension between the crystal and the solution [25]. ΔG_V has a r^3 dependence and ΔG_S has a r^2 dependence [25]. Shown in figure Figure 1.3, ΔG_V and ΔG_S compete [25]. ΔG_V shows a decrease in volume free energy, whereas ΔG_S shows an increase in surface free energy [25]. In this figure, it can be seen that the ΔG_{TOT} first increases until it reaches a maximum ΔG_C, after which it starts decreasing [25]. ΔG_C corresponds to nuclei with a critical radius r_C, which implies that nanoparticle nuclei $r < r_C$ will dissolve to their monomers and nuclei with $r > r_C$ will grow to nanoparticles [25]. The critical radius is given by equation Equation (1.6) and shows us that higher supersaturation or temperature will lead to a smaller r_C [25]. Additionally, the amount of critical nuclei formed is in direction relation to the concentration of monomers in the solution [25].

$$r_C = -\frac{2\gamma}{\rho k T \ln S} \tag{1.6}$$

The rate of nucleation is influenced by the interfacial tension γ, the reaction temperature T and supersaturation S [25]. Control over these factors leads to control over the nuclei that are obtained [25]. To obtain many, small nuclei, fast nucleation is desired [25]. This can be achieved by a creating a solution which is supersaturated at a high temperature [25]. This leads to a high rate of nucleation, which subsequently decreases the supersaturation rapidly as well. Finally, this decrease in supersaturation leads to low nucleation rates [25]. This leads to separation between the nucleation stage and the growth stage [25]. This is desirable for obtaining monodisperse nanoparticles [25].

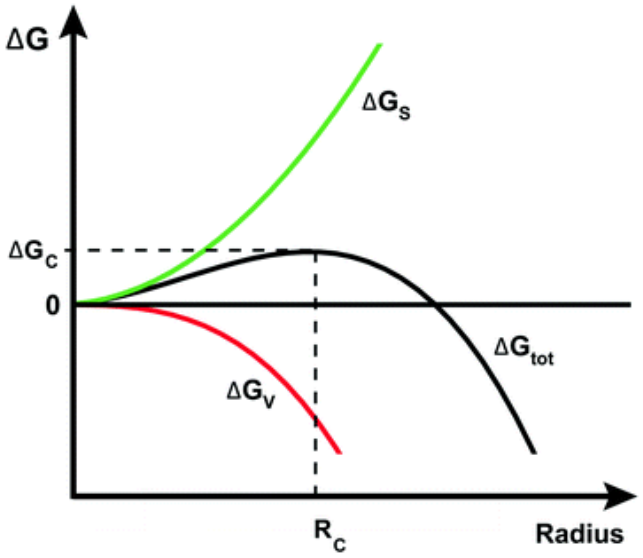

Figure 1.3: Diagram of the change of surface free energy ΔG_S, volume free energy ΔG_V and total free energy ΔG_{TOT} during the formation of a nanocrystal nuclei. ΔG_C indicates the activation barrier for nucleation. Reproduced from Donega et al [25].

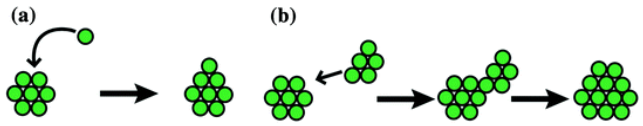

Figure 1.4: The two methods of growth for nanoparticles. a) Incorporation of a monomer into an existing NP. b) Aggregation of two NPs. Reproduced from Donega et al [25].

Growth stage

The final stage of NP synthesis is the growth stage, in which the nuclei which were formed during the nucleation stage grow to mature nanoparticles by incorporation of monomers present in the solution, or by incorporating other smaller nanoparticles [25]. Growth of nanoparticles will continue until equilibrium, however this is generally not desired [25]. If growth continues until equilibrium, larger nanoparticles with a broader size distribution will be obtained [25]. This is due to a process known as Ostwald ripening [25]. Ostwald ripening involves the growth of larger nanoparticles by dissolution of smaller nanoparticles [25]. To prevent this, typically a growth reaction is quenched by cooling down of a reaction mixture or by addition of a large amount of solvent [25]. Nanoparticles grow faster with increasing monomer concentration and temperature [25]. Ligands also strongly influence the growth speed of nanoparticles, as they limit the availability of the nanoparticle surface for monomer incorporation [25]. As shown in figure Figure 1.4, there are two distinct ways for a NP to grow; either by incorporation of a monomer into the NP or by aggregation of two NPs [25]. In the first case, two distinct steps are found [25]. First, the monomer needs to diffuse to surface of the NP and second, the monomer needs to be incorporated into the NP [25]. Donega et al suggest that this growth can either be reaction-controlled or diffusion-controlled [25]. Reaction-controlled growth describes the case where the rate-limiting step of nanoparticle growth is the incorporation of the monomers into the nanoparticles [25]. Diffusion-controlled growth is the case wheree the reaction rate of the growth is limit by diffusion of the monomers to the NP surface [25]. In general, growth is reaction-controlled at high monomer activities (activity is used instead of monomer concentrations, as the solutions described here are far from ideal solutions) [25]. Growth tends to be diffusion-limited when the concentration of monomers near the NPs is low, so at low monomer activities [25]. At high monomer activities, the critcal radius r_C is small [25]. This means that many nuclei will grow, with smaller NPs growing faster which results in smaller size distribution [25]. At lower monomer activities, Ostwald ripening may occur [25]. In this case, the smaller nanoparticles will dissolve to fuel the growth of the larger particles [25]. This leads to a broader size distribution [25]. A low monomer activity can be prevented by stopping the reaction

whilst the monomer activity is still high, or by continuously injecting precursor to maintain high monomer activity [25].

Ligands and reducing agents

Ligands and reducing agents are key parts of colloidal synthesis, yet the interplay between the many different parameters in colloidal synthesis makes it difficult to elucidate individual effects [62–64]. Excellent reviews on the role of ligands and reductants in colloidal synthesis can be found in literature [62–64]. Below, some general trends are briefly discussed.

Ligands have great influence on the various aspects of catalyst synthesis through colloidal chemistry. First ligands have influence on the three stages discussed for the colloidal synthesis of NPs [25]. Secondly, the ligands influence the deposition of these synthesized NPs onto support material [62]. Finally, the ligands need to be removed to ensure no blocking of catalytic test setup during catalysis. Another important aspect is the potential of ligands to block active sites of the metals, which is a separate reason why ligands might need to be removed [3]. Here, the role of ligands in colloidal synthesis will be discussed.

Ligands can act as stabilizing agents for metal NPs in solution [25] The choice of ligand is essential for the size and shape of NPs and should therefore be controlled and studied [25]. Additionally, the ligands influence the properties of the metal nanoparticle in solution [25]. There is a large library of different ligand molecules that can be used to form a shell around the metallic cores of NPs [25,62]. By choosing a suitable ligand, this shell can improve the interaction with either organic solvents or with water, allowing for customization of the solubility of the nanoparticles [62,64]. Strong ligands are those which bind strongly to the metal surface, which limit nanoparticle growth but stabilize a colloidal particle very well [25]. Shorter alkyl chains for hydrocarbon ligands lead to weaker metal-ligand bonds and weaker inter-ligand interactions [25]. Steric effects also influence the ligand-metal interaction strength, where bulkier ligands typically bind more strongly to the metal particle [25]. Generally, weaker ligands tend to bind on and off a surface at higher rates than stronger ligands would, and subsequently allow for faster growth as the surface of the nanoparticle is more available for monomer incorporation [25]. Ligands limit the available surface for monomer incorporation and thus the concentration of ligands also impacts growth [25]. Surfactants can also influence the nucleation rates by stabilizing monomers in solution or modifying precursor reactivity [25]. Highly interesting is the fact that ligands can also bind preferentially to certain facets, limiting their growth and facilitating growth of specific facets, leading to specific non-spherical shapes [25].

Reducing agent in colloidal synthesis

Reducing agents are those chemicals which reduce a metal ion to their metallic form (e.g. Ni^{2+} to Ni^0) by providing electrons to a redox reaction [63]. An overview of the steps is shown in Equations (1.7) to (1.9).

$$R_{red} \rightarrow R_{oxi} + ne^- \tag{1.7}$$

$$M^{n+} + ne^- \rightarrow M^0 \tag{1.8}$$

$$R_{red} + M^{n+} \rightarrow R_{oxi} + M^0 \tag{1.9}$$

Here R_{red} is the reducing agent, R_{oxi} the oxidized form of the reductant, M^{n+} the metal ion, M^0 the reduced meta and e^- the electrons. This equation is similar to Equation (1.4), where the stabilizers are taken into account. The concentration and nature of the reducing agent used in the synthesis influence the size of the colloidal nanoparticles [25,63]. If we return to the fundamentals explained in Section 1.2, we can conclude the choice of reducing agent/precursor combination is a key part of successful colloidal synthesis [63]. Typically, a strong reducing agent (e.g. readily donates electrons) results in faster nucleation and consequently more homogeneous nucleation [63]. However, the solubility of the reducing agent is equally important, as inhomogeneous nucleation will still occur if the reducing agent is not very soluble, as interaction with the metal precursor would be limited [63].

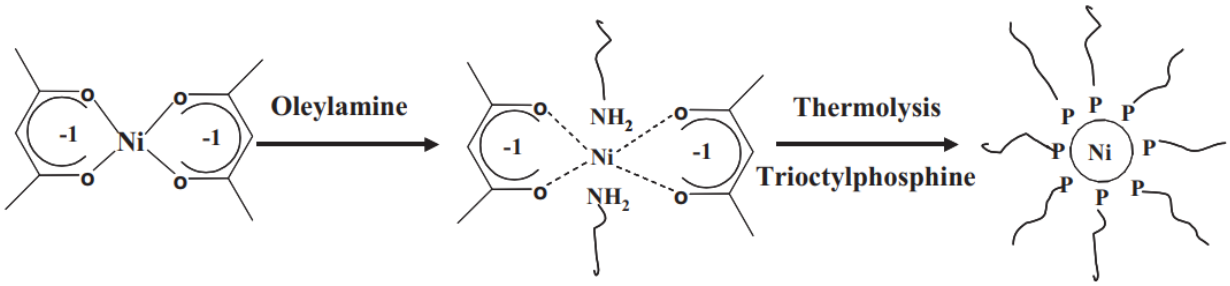

Figure 1.5: Synthesis of nickel nanoparticles through thermal decomposition of a Ni-oleylamine complex. First $Ni(acac)_2$ reacts with oleylamine to a Ni-oleylamine complex, which is then injected into a hot solution containing trioctylphosphine, which acts as a stabilizing agent for the metal Ni clusters that form. Reproduced from Park et al [67].

Strategies for the synthesis of colloidal nickel nanoparticles

Synthesis of colloidal Ni nanoparticles has extensively been investigated, changing a large variety of parameters. For example, in the case of Ni nanoparticles, several different ligands have been used, including TOP, TOPO, oleylamine (OAm), oleic acid (OAc), polyethylene glycol (PEG), poly(vinyl)pyrrolidone (PVP) [3,26,27,55,58–61,65–67]. Extensive research has been done on preparation of colloidal nickel nanoparticles using phosphorous-containing ligands [26,27,65–68]. Carenco et al obtained a tunable size range for nickel nanoparticles between 2 and 30 nm by using trioctylphosphine (TOP) as a ligand and oleylamine (OAm) as a reductant [26]. TOP coordinates to the nickel nanoparticle surface, stabilizing the molecule in solution [26]. It also limits further growth of the metallic nickel nanoparticle [26]. A schematic overview of this system is depicted in Figure 1.5. However, as result of using TOP as a ligand and the reaction conditions used in preparation of nickel nanoparticles, phosphorous is incorporated in these nanoparticles, forming Ni_2P [27]. In addition, Rinaldi et al found that the removal of TOP and TOPO from Ni surfaces through heat treatments was difficult [69]. Synthesis of nickel nanoparticles without making use of phosphorous ligands is therefore highly interesting to study the CO_2 hydrogenation reaction over nickel nanoparticles.
In literature, colloidal synthesis of phosphorous-free nickel nanoparticles of different sizes is reported [3,58–61], but not yet with the same size control as found for colloidal synthesis with phosphorous-containing ligands [26]. [60,70]. Zacharaki et al reported synthesis of small monodisperse nickel nanoparticles in a size range of 4 to 9 nm using oleic acid (OAc) as a surfactant [60]. In this case, the synthesis method relied on the usage of an extremely air-sensitive compound bis(1,5-cyclooctadiene)-nickel(0) ($Ni(cod)_2$), which complicates the synthesis significantly. They found a linear relation between the Ni-precursor to surfactant ratio and the size of the nanoparticles [60]. Thus the surfactant nature and concentration are both of potentially great influence on the final nanoparticle shape and size.
A different approach is the usage of strong reducing agents to induce fast and homogeneous nucleation. Reducing agents previously used for the synthesis of Ni NPs include borane tert-butylamine complex (BTB), OAm, TOP, Tetrabutylammonium bromide (TBAB), PEG, hydrazine, PVP and sodium borohydride ($NaBH_4$) [3,26,58,59,71]. Reduction of $NiCl_2$ by hydrazine yielded monodisperse 9.2 Ni nanoparticles [71]. It should be noted that many of these reducing agents are also employed as capping agents and solvents, often in the same synthesis [63]. A relatively mild reducing agent, BTB, is interesting for the synthesis of Ni nanoparticles, especially when compared to a more dangerous chemical like hydrazine. Metin et al demonstrated the synthesis of monodisperse 3 to 5 nm Ni seeds by changing the BTB/Ni precursor molar ratio and Vrijburg et al demonstrated a method to grow the Ni seeds even further to 8 nm [3,58]. The authors succeeded in this by modification of the synthesis approach, rather than changing the chemicals used [3]. Here, a seed-mediated growth approach was demonstrated. In this case, first small nanoparticles known as seeds are synthesized by hot-injection. These seeds are then further grown into larger nanoparticles by slowly adding additional precursor. The authors succeeded in extending the available size range for the Ni nanoparticles from 3.2 nm up to 8 nm [3]. This approach had the major advantage that no new chemicals (save octadecene, a solvent) are introduced, which keeps the synthesis of these different sizes of Ni nanoparticles comparable [3].

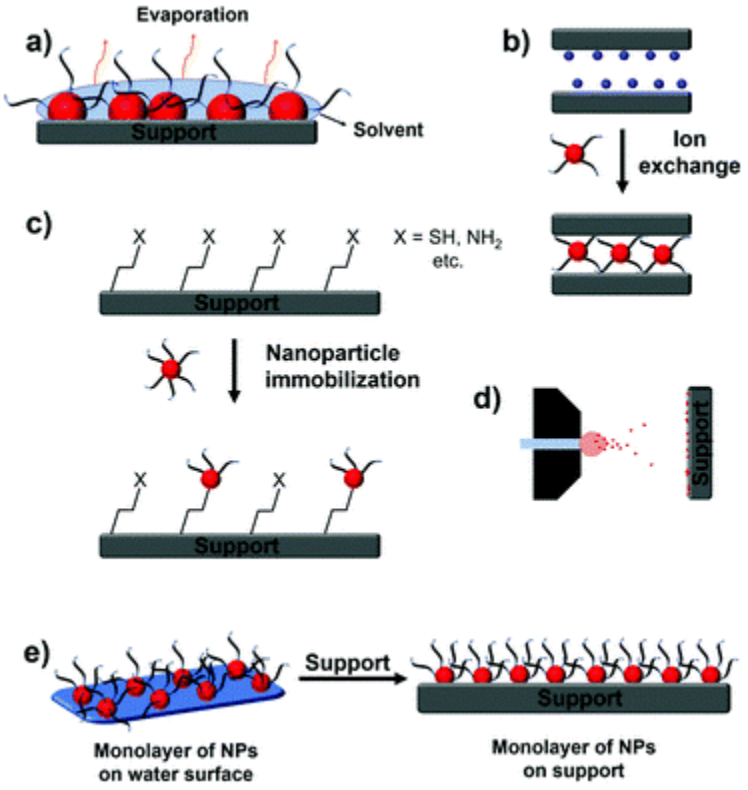

Figure 1.6: An overview of some methods that are applied for the deposition of colloidal metal nanoparticles on support materials. These are a) Direct colloidal deposition, b) Ion-exchange, c) Nanoparticle surface modification, d) Flame-spraying, e) Langmuir-Blodgett. Reproduced from Rossi et al [62].

1.2.2 Deposition

Colloidal metal nanoparticles need to be placed on a support material to be able to be used as a heterogeneous catalyst [2]. This step is known as deposition, and the choice of ligands, solvents, methods and support is key to controlling the obtained heterogeneous catalysts [2]. An overview of some commonly used deposition methods is given in Figure 1.6. Direct colloidal deposition is a relatively straightforward method in which a wet impregnation is performed using the colloidal suspension [55]. Typically, the powder is then filtrated and washed [72–75] and/or the excess solvent is evaporated [60,75]. Then, the support material is dried, under air [73,75], vacuum [74,75] or via freeze-drying [76]. Key during direct colloidal deposition are the mild reaction conditions that are employed, as these limit the amount of restructuring during deposition [55]. Other colloidal deposition methods include ion-exchange, surface modification, flame-spraying and Langmuir-Blodgett techniques [55]. Lee et al demonstrated applicability of direct colloidal deposition in preparing well dispersed Pt on silica xerogels as a comparison with *in situ* reduction of H_2PtCl_6 as well as sol-gel synthesis of the silica support in the presence of preprepared Pt nanoparticles [73]. Here, the authors demonstrated that wet impregnation with the Pt colloids led to superior dispersion of Pt nanoparticles. In this thesis, direct colloidal deposition through wet-impregnation is used, as this is a facile method to prepare well dispersed supported nanoparticle catalysts [55].

1.2.3 Catalyst activation

After the deposition of the colloidal nanoparticles onto support materials, the catalysts still need to be activated. In particular, residual organic material and ligands that are still attached to the Ni surface need to be removed. These might prevent access to active sites and thus limit catalytic activity [69,77,78]. Typical approaches to ligand removal are either thermal or chemical treatments [79]. Thermal treatment is a straightforward approach, where a sample is loaded into a reactor and treated at high temperatures (250-500 °C) under inert, oxidative or

reductive atmosphere which decomposes or desorbs the ligands in question, thereby removing them from the metal surface[79]. In most cases, this is then followed by an appropriate reduction step to obtain the active metal[79]. Chemical treatment is different approach in which the ligand stabilized Ni nanoparticles are treated with a solution containing small capping molecules[79]. In essence, these replace the larger organics typically used in colloidal synthesis[79]. The smaller molecules, like water and acetic acid, but also diethylamine and butylamine, are typically much easier to remove and interfere less with reactants during reactions[79]. For example, polyvinyl alcohol is easily removed from gold NPs by water, whilst at the same time no particle aggregation is observed[80]. Hydrophobic molecules like oleylamine are also removed from gold and platinum NPs using diethylamine without changes to particle morphology[81]. In this thesis, thermal methods are applied to remove ligands. These methods are typically straightforward, applicable to most support materials and allow for more direct comparison with existing incipient wetness impregnation catalysts, which are also thermally treated.

1.3 Research aims

The central goal of this thesis is to prepare active, well-defined Ni based hydrogenation catalysts through colloidal synthesis without using phosphorous-containing ligands. This large undertaking is divided into several parts, schematically shown in Figure 1.7.
The first part consists of the synthesis of Ni colloids in suspension. In Chapter 3, the results of different colloidal synthesis methods are presented. Here, the aim is to answer the following research questions:

- How can the Ni nanoparticle size be controlled through hot-injection and seed-mediated growth using OAm and OAc as ligands?
- In what way is it possible to controllably synthesize large (> 7 nm) Ni nanoparticles without using phosphorous-containing ligands?

The second part of the thesis is the deposition of these colloids on various supports. The third part discusses the heat treatments necessary to remove the ligands and activate the catalyst material. In Chapter 4, the deposition of the synthesized colloids is discussed and the influence of support and deposition method on deposition is described. In the same chapter, the removal of ligands and residual organic material using mild thermal treatments is also described.

- How can the deposition of different sizes of Ni colloids be controlled whilst maintaining their size and size distribution?
- In what way is it possible to remove ligands and activate the Ni catalyst prepared using colloidal methods maintaining their size and size distribution?

In Chapter 5, *in situ* transmission electron microscopy is used to identify oxidation and reduction behaviour of Ni/C catalysts. This is used to answer the following research question:

- How can *in situ* transmission electron microscopy be used to investigate the oxidation and reduction behaviour of carbon supported Ni nanoparticles?

The fourth and final part concerns the catalytic performance of the synthesized catalysts. In Chapter 6 high-pressure catalysis is used to understand the influence support materials, ligands choices and synthesis methods may have on catalytic CO_2 hydrogenation. These results are used to answer the following research questions:

- What is the influence of the support material on CO_2 hydrogenation?
- How do conventional impregnation catalysts compare to those prepared by colloidal synthesis?
- How do catalysts prepared using phosphorous-containing ligands compare to those prepared without phosphorous-containing ligands?

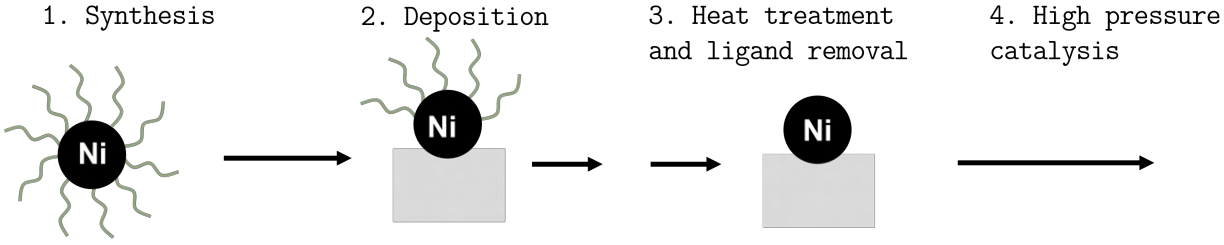

Figure 1.7: An schematic overview of the work presented in this thesis. It consists of four distinct parts; 1) Colloidal synthesis, 2) Deposition of colloids, 3) Removal of ligands and activation of prepared precatalysts and finally 4) high pressure catalysis.

Chapter 2

Experimental

In this chapter, the methods and chemicals used in this thesis are discussed in detail, including used calculations and devices.

2.1 Synthesis

2.1.1 Chemicals

Chemicals were purchased from the following vendors at the indicated purity and used as purchased unless indicated otherwise: Nickel(II)acetylacetonate ($Ni(acac)_2$, > 98 %, Sigma Aldrich), borane *tert*-butylamine complex (BTB, 97 %, Sigma Aldrich), oleylamine (OAm, >70 %, Sigma Aldrich), oleic acid (OAc, >99 %, Sigma Aldrich), toluene (tol, 90%, Fischer Scientific), Polyethylene glycol (PEG400, M_w = 400 g/mol, Sigma Aldrich), concentrated nitric acid (HNO_3, 65 %, VWR International), acetone (C_3H_6O, 99.8 % VWR Chemicals), ethanol (C_2OH, >99 %, VWR Chemicals), GNP500, (grade-c, 500 m^2/g, XG Sciences,), Davisil 643 silica gel (SiO_2, > 99 %, 300 m^2/g, Sigma Aldrich), nickel(II)nitrate hexahydrate ($Ni(NO_3)_2.6H_2O$, 97 %, Sigma Aldrich), trioctylphosphine (TOP, 90 %, Sigma Aldrich), 1-octadecene (ODE, 90 %, Sigma Aldrich), SBa200 alumina (Al_2O_3, 98 %, 200 m^2/g, Sasol) and Aerosil 380V silica (SiO_2, 380 m^2/g, Evonik).

2.1.2 Colloidal synthesis

The various colloidal synthesis methods are described below. Some general considerations that were applicable for all syntheses are described here. Temperatures reported in this thesis had all been measured with a thermocouple inside the solution. Temperature was kept constant by a second thermocouple in contact with the heating mantle. Syntheses were performed with a glass (Pyrex© Spinbar©) magnetic stirrer or a teflon coated magnetic stirring bar. The glass-coated magnetic stirring bar was used because the magnetic Ni colloids can migrate into the porous teflon coated magnetic stirring bars.

Synthesis using only OAm and $Ni(acac)_2$ through heating-up method

This synthesis method was based on a procedure demonstrated by Carenco et al[26]. A schematic depiction is shown in Figure 2.1a. A heating mantle (A) was preheated to 230 °C. Typically, 0.052 g of $Ni(acac)_2$ was weighed in a 100 mL round-bottomed flask with 4 connectors. 5 mL of OAm is added to the round-bottomed flask containing a magnetic stirrer, taking care to flush any $Ni(acac)_2$ remaining on the walls to the bottom of the flask. This flask was closed off and brought under N_2 atmosphere and connected to a condenser. The solution was stirred at 400 RPM. A thermocouple was placed in the solution to monitor the temperature. The solution was then heated to 110 °C using a heating mantle (B), degassed and any water was removed by repeatedly bringing the flask under vacuum and subsequently under N_2 atmosphere. This was repeated 5 times. After this, heating mantle (B) was replaced by the preheated heating mantle (A) and the time was monitored until the solution reaches 230 °C. After this temperature was reached, the solution was kept at this temperature for 10 min by changing the nitrogen flow. After 10 min had passed, the heating mantle (A) was removed and the reaction mixture was allowed to cool down. Typically, a clear solution was observed with a

black precipitate on the magnetic stirrer. The solution was then decanted and the magnetic stirrer was placed in a separate 15 mL plastic vial. To this vial, 10 mL of acetone was added. This mixture was then sonicated until a black solution remains. Typically, after removal from the sonication bath, the black solution became more and more transparent and the magnetic stirrer had more and more black precipitate attached to it. To obtain a as concentrated solution possible, the magnetic stirrer was removed from the vial whilst it was in the sonication bath using another magnetic stirrer. The obtained black solution was then centrifuged at 4000 RPM for 5 minutes. A black precipitate was typically observed at the bottom of the vial. The remaining clear acetone solution was then decanted. This was repeated once. The precipitate remaining after the second centrifugation step was then dispersed in 6 mL toluene and sonicated in the sonication bath until a black solution is obtained. This solution was kept in a 20 mL glass vial.

Synthesis using only oleylamine and $Ni(acac)_2$ through hot-injection

This synthesis method was based on a procedure demonstrated by Carenco et al [26]. A schematic depiction is shown in Figure 2.1a. 0.052 g of $Ni(acac)_2$ was weighed in a 100 mL round-bottomed flask (1) with 4 necks containing a magnetic stirrer. To this flask 2 mL of OAm was added. To a second 100 m round-bottomed flask (2) with 4 necks containing a glass stirring bar, 8 mL of OAm was added. The flask (2) was then connected to a water condenser. Both flasks (1 and 2) were degassed and water was removed at 110 °C by repeatedly evacuating the flasks (1 and 2) with a vacuum pump and subsequently bringing them under N_2 using a needle connected to a N_2 flow. Heating was done by heating-mantles and temperature control was obtained by using a connected thermocouple. The flask (1) containing the $Ni(acac)_2$ solution was kept at 110 °C, whereas the other flask (2) was heated to 230 °C. Upon reaching 230 °C in the second flask (2), the $Ni(acac)_2$ solution was rapidly injected into the second flask (2) using a syringe. While stirring vigorously, the solution was kept like this under N_2 for 10 min. After 10 minutes, the heating-mantle was removed and the solution was allowed to cool down to room temperature. Upon reaching room temperature, 5 mL of toluene was added. The mixture was then brought over into a 50 mL centrifuge vial and 30 mL of acetone was added. The mixture was centrifuged at 4000 RPM for 5 min, the supernatant was discarded and the precipitate was redispersed in 5 mL toluene. This was then repeated twice and the final resulting suspension was kept in a 20 mL glass vial.

Ni seeds synthesis by hot-injection with borane tert-butylamine complex

This synthesis method was based on a procedure as demonstrated by Vrijburg et al [3]. A schematic depiction is shown in Figure 2.1a. x g of $Ni(acac)_2$ was weighed in a four-necked 100 mL round-bottomed flask (1) containing a magnetic stirrer. To this flask, y mL of OAm was added. z g of BTB (with z corresponding to a 5:1 ratio of mol BTB:$Ni(acac)_2$) was added to a separate round-bottomed flask (2) also containing a magnetic stirrer and was dissolved in an equimolar amount of OAc and 2 mL OAm which was added using a Finn-pipet. Both solutions were stirred at 400 RPM, connected to a vacuum pump, brought under N_2 flow and heated to 110 °C. The solutions were then repeatedly brought under vacuum and subsequently again under N_2 to remove any air and water still present in the solutions. This was repeated five times, resulting in 30 minutes of which 15 minutes under vacuum and 15 minutes under N_2. After degassing, the solutions were brought to 90 °C. The BTB solution was then rapidly added to the $Ni(acac)_2$ solution by injection using a plastic syringe with a metallic needle. This solution was then kept at 90 °C for 1 hour. The heating mantle was then removed and the solution was allowed to cool down to room temperature while 8.5 mL of toluene was added. The mixture was then placed into two separate plastic 50 mL centrifuge vials. To both centrifuge vials, 20 mL of acetone was added and the resulting mixture was centrifuged at 8000 RPM for 20 minutes. The resulting supernatant was discarded and the precipitates were each redispersed in 5 mL toluene. An additional 35 mL acetone was added to both vials and the mixtures were then again centrifuged at 8000 RPM for 20 minutes. This was repeated twice. Finally, the resulting precipitates were each redispersed in toluene depending on the desired concentration of the final suspension and brought together into a 20 mL glass vial.

Large Ni NP synthesis by hot-injection and seed-mediated growth

This synthesis method was also based on a paper by Vrijburg et al [3]. A schematic depiction is shown in Figure 2.1b. First, the Ni seeds were synthesized according to Section 2.1.2. Instead of adding toluene and allowing the mixture in flask (1) to cool down after the synthesis of the seeds, the mixture was heated to 200

°C. While the flask (1) was cooling down, x g of $Ni(acac)_2$ was dissolved in an equimolar amount of OAc and y mL ODE in a four-necked 100 mL round-bottomed flask (3) containing a magnetic stirrer. This suspension was then heated to 110 °C and degassed in the same way as the mixtures in the other flasks (1 and 2). The solution was then brought into a large syringe and placed in a syringe pump. This was then slowly pumped into the flask containing the Ni seeds at a rate of 0.1 mL/min. Including addition time (which depends on the amount of injected solution), the reaction was left to react for 1.5 hours, after which the heating mantle was removed and the mixture was allowed to cool down. Upon reaching 150°C, an equal volume of toluene was added. The suspension was then allowed to cool down further to room temperature. The suspension was then divided over three plastic 50 mL centrifuge vials and to each vial, 25 mL of acetone was added. The suspensions were then centrifuged at 8000 RPM for 5 minutes. The supernatants were then discarded and the precipitates were redispersed in 5 mL toluene and an additional 35 mL of acetone was added. The suspensions were then centrifuged at 8000 RPM for 5 minutes. This was repeated twice. Finally, the resulting precipitates were each dispersed in 5 mL toluene and brought together in a 20 mL glass vial.

Large Ni NP synthesis by heating-up method using TOP

This synthesis method was based on a paper by Carenco et al[26]. A schematic depiction was shown in Figure A.1. 0.2568 g of $Ni(acac)_2$ was added to a four-necked round-bottomed flask (1) containing a magnetic stirrer and connected to a vacuum pump and a N_2 flow. To this flask (1), 3 mL of OAm was added and degassed at 110 °C for 30 minutes by repeatedly switching between N_2 flow and vacuum. 3.58 mL of OAm was then added to second four-necked flask (2) containing a magnetic stirrer. This flask (2) was then degassed at 110 °C by repeatedly switching between N_2 flow and vacuum. Then, 13.38 mL TOP was carefully added to flask (2) without exposing it to air. This flask (2) was then heated to 220 °C. Upon reaching this temperature, the solution in flask (1) was added to flask (2), again without exposing it to air. The new mixture was then kept at 220 °C for 2 hours. The sample was then allowed to cool down to RT by removing the heating mantle. The mixture was then centrifuged at 8000 RPM for 5 minutes in a 50 mL plastic centrifuge vial after adding 20 mL of acetone. The supernatant was discarded and the precipitate was redispersed in 5 mL toluene and 35 mL of acetone was added. This was then centrifuged at 8000 RPM for 5 minutes. This was repeated twice. The final precipitate was dispersed in 10 mL toluene.

Large Ni NP synthesis by heating-up method in PEG400

This synthesis was based on a paper by Tzitzios et al[59]. A schematic depiction was shown in Figure A.2. 0.1465 g of $Ni(NO_3).6H_2O$ was added to a 100 mL four-necked round-bottomed flask containing a glass magnetic stirrer. 0.48 mL OAc, 0.49 mL OAm and 10 mL PEG400 was added to the flask and it was stirred at 400 RPM. The solution was then brought under N_2 atmosphere. The mixture was then heated to 120 °C and kept at this temperature for 30 minutes. Then, the mixture was rapidly heated to 215 °C using a separate preheated heating mantle. After 1 hour at 205 °C, the reaction mixture was allowed to cool down to RT and 20 mL of EtOH is added. The resulting mixture was brought into two 50 mL centrifuge vial and was centrifuged at 8000 RPM for 5 minutes. The supernatants were discarded and the precipitates were redispersed in 2 mL toluene and 20 mL acetone was added. This mixture was then centrifuged at 8000 RPM for 5 minutes. This was repeated twice. Finally, the resulting precipitates were each dispersed in 3 mL toluene and kept in a 20 mL glass vial.

2.1.3 Deposition

Deposition of nanoparticles was achieved by two methods, a slow-evaporation method and a sonication-assisted deposition method.

Slow-evaporation

A schematic depiction of the slow-evaporation method is shown in Figure A.4. Typically, 1 g of support material was placed in a 100 mL three-necked round-bottomed flask containing a magnetic stirrer and dried under vacuum at 180 °C for 2 hours. Then, an amount of Ni colloids in toluene was added depending on the desired wt-% of the catalyst. An amount of extra toluene was added to have a constant concentration of 0.0025 g Ni/mL in the used suspension. The top neck of the flask was covered with aluminium foil with some holes.

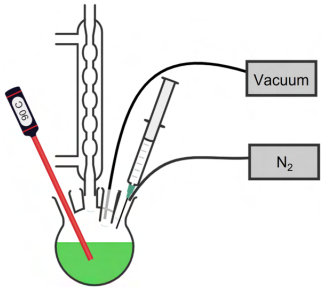

(a) Setup used for hot-injection and heating-up methods of colloidal synthesis, as described in Section 2.1.2

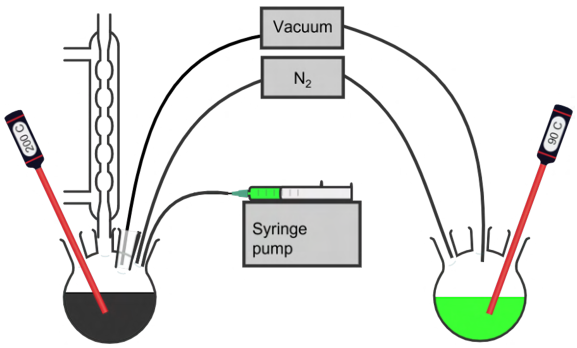

(b) Setup used for seed-mediated growth of Ni nanoparticles, as described in Section 2.1.2.

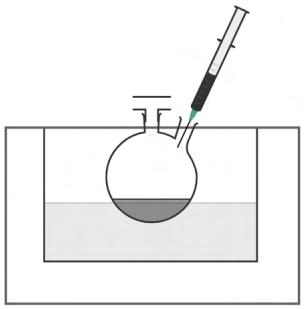

(c) Setup used for sonication-assisted deposition of Ni nanoparticles, as described in Section 2.1.3

Figure 2.1: Schematic overview of experimental setups used in this thesis.

The two remaining necks were blocked using a glass stopper. The mixture was then stirred at 60 RPM and heated to 90 °C using a heating mantle. The flask was left like this for 18 h, after which it was allowed to cool down to RT.

Sonication-assisted deposition method

A schematic depiction of the sonication-assisted deposition method is shown in Figure 2.1c. Typically, 1 g of support material was placed in a 100 mL two-necked round-bottomed flask and was dried at 180 °C for 2 hours. Then, the flask was lowered into a sonication bath and the sonication bath was turned on. After 10 minutes of sonicating the dry powder, a pre-prepared solution of 0.0025 g Ni/mL Ni colloids was added to the flask using a plastic syringe, taking care not to have any air be pulled in through the syringe by the vacuum in the flask. Once the support material was covered by the suspension, the flask was carefully exposed to air and left to sonicate for 30 minutes. After sonication, the flask was connected to a rotary evaporator and the excess solvent was quickly evaporated at 45 °C. When condensation of toluene in the condenser of the rotary evaporator stops, the powder was left to dry for an additional 30 minutes, to ensure complete solvent removal.

2.1.4 Catalyst activation

Calcination and reduction were performed using the setup shown in Figure A.3. Typically, the desired amount of catalyst precursor was loaded into a reactor (an image can be found in Figure A.6) with a top-down gas flow. A thermocouple was placed next to the outside of the reactor where the sample was located to ensure that the desired temperature was achieved. Calcination experiments were performed in 20 vol-% O_2 in N_2 and reduction experiments in 5 vol-% H_2 in N_2. Reactors were first taken to 40 °C and flushed with N_2 before a new gas was added and a new heat treatment was started. All samples are kept under N_2 atmosphere after heat treatments and were passivated before further experiments. Passivation was achieved by carefully creating a small opening to ambient atmosphere and keeping the sample like this overnight. For all samples, a total flow of 200 mL/g_{sample} was used.

Calcination treatments were performed at 250 °C or 500 °C for 2 hours, whereas reduction treatments were performed at 350 °C for 2 hours, both with heating ramps of 5 °C/min.

2.1.5 Catalyst synthesis through incipient wetness impregnation

Impregnation catalysts were also prepared. A solution of $Ni(NO_3)_2.6H_2O$ in MiliQ water (0.6566 mol/L) was prepared by weighing 1.91 g of $Ni(NO_3)_2.6H_2O$ in a 10 mL volumetric flask. 7 mL of MiliQ water was added to this flask. 65 µL of 63% HNO_3 is added to the flask and the $Ni(NO_3)_2.6H_2O$ was allowed to dissolve. After complete dissolution of the $Ni(NO_3)_2.6H_2O$, MiliQ water was added until the 10 mL line is reached. This results in 0.1 M HNO_3 $Ni(NO_3)_2.6H_2O$ in MiliQ solution. The $Ni(NO_3)_2.6H_2O$ was first completely dissolved

before adding the final MiliQ water to make sure all water in the $Ni(NO_3)_2.6H_2O$ was first released so that the concentration was known. 1.5 g of GNP500 (0.8002 mL/g) was then weighed and dried at 175 °C for 150 minutes. The density of the solution was measured by repeatedly weighing 1 mL of solution and taking the average of these measurements. The carbon was then impregnated through incipient wetness impregnation (IWI). 90% of the pore volume as determined by physisorption was impregnated. Using this volume and the density of the $Ni(NO_3)_2.6H_2O$ solution, the necessary mass of $Ni(NO_3)_2.6H_2O$ solution was weighed and added dropwise to the dried support while stirring. The sample was then dried overnight under vacuum at room temperature.

The impregnation sample was treated in two different ways, 1) first a heat treatment in N_2 at 350 °C with a ramp of 2 °C/min, then a calcination in O_2 at 250 °C with a ramp of 5 °C/min and a subsequent reduction in H_2 at 350 °C with a ramp of 5 °C/min and 2) a heat treatment in N_2 at 400 °C with a ramp of 2 °C/min and a reduction in H_2 at 350 °C with a ramp of 2 °C/min.

2.2 Characterization methods

This part briefly describes the characterization methods, what they were used for in this thesis and what methods were used to determine certain values.

2.2.1 Electron Microscopy

Electron microscopy (TEM) was performed using either a FEI Talos™ F200X set at 200 kV or a FEI Talos™ L120C at 120 kV.

Transmission Electron Microscopy (TEM)

Transmission Electron Microscopy was used to determine the average particle size of both the Ni colloids as well as the supported nanoparticles. Additionally, the shape and dispersion of nanoparticles across the support was investigated. The average particle size and particle size distribution was determined based on at least 100 counted particles per sample, for which ImageJ software was used. TEM samples were prepared by dropcasting a diluted suspension of colloids onto a carbon-coated copper TEM grid. Typically, a diluted colloidal suspension was prepared by dropping three drops of the concentrated colloidal suspension into 2 mL toluene. TEM samples of catalysts powders and deposited nanoparticles were prepared by repeatedly submerging the TEM grid in the desired sample powder, previously crushed using a mortar and pestle.

High-angle annular dark-field Scanning Electron Microscopy (HAADF-STEM)

HAADF-STEM was performed on the FEI Talos™ F200X to investigate Ni/SiO_2. Additionally, energy-dispersive X-ray spectroscopy (EDX) was used to determine the presence of phosphorous and nickel.

2.2.2 Temperature programmed reduction (TPR)

The influence of temperature on catalyst and support reduction behaviour was analyzed with the Micromeritics® AutoChem II Chemisorption Analyzer. Typically, a quartz glass tube reactor was loaded with some quartz wool. Then, 50 mg of sample with a sieve fraction > 38 µm was placed on top. Finally, some additional quartz wool was loaded on top of the sample to prevent it from being blown out of the reactor. The sample was heated to 120 °C with a ramp of 10 °C min^{-1} under a 50 mL min^{-1} argon (Ar) flow and dried for 10 minutes. The sample was cooled down to ambient temperature and the gas flow was switched to 5 vol-% H_2 in Ar. After switching the gas flow, the sample was heated to 900 °C with a ramp of 5 °C min^{-1}. The amount of H_2 leaving the reactor was measured using a thermal conductivity detector (TCD). A cold trap prepared using a thermal beaker filled with isopropanol and cooled down with dry ice was used to capture formed water. Equation (2.1) is used to calculate the weight percentage of Ni in Ni/SiO_2 samples.

$$\text{Ni wt-\%} = A_{peak} * M_{sample}/V_m * Mw_{Ni} \tag{2.1}$$

Here V_m is the molar volume, the A_{peak} corresponds to the peak area in amount of dm^3 H_2 that is consumed per gram of loaded sample, M_{sample} to the amount in grams of loaded sample and Mw_{Ni} to the molar mass of metallic Ni.

2.2.3 Thermogravimetric analysis coupled with mass spectrometry(TGA-MS)

Catalyst and support material behaviour, as well as ligand removal and Ni wt-% was investigated using thermogravimetric analysis coupled to a mass spectrometer. TGA measurements were performed using a PerkinElmer Thermogravimetric Analyzer TGA8000. Downstream mass spectrometry was performed using a Hiden Analytical HPR-20. Typically, 3-5 mg of sample was loaded onto a small plastic analyzing cup and brought under a 100 mL min^{-1} Ar flow. The sample was then heated to 120 °C with a ramp of 5 °C min^{-1}, where it was kept for 30 minutes and dried. Then, the gas flow was changed to a 20 vol-% O_2 in Ar with a total flow of 100 mL min^{-1}. The sample was then heated with a ramp of 5 °C min^{-1} to 800 °C, where it was kept for 2 hours in the case of carbon supports to burn away all the carbon present. An indication of the Ni wt-% in carbon supported Ni NPs could be obtained by using Equation (2.2):

$$\text{Ni wt-\%} = \frac{m_{tot}}{m_{Ni}} * 100\ \% \quad \text{and} \quad m_{Ni} = M_{Ni} * \frac{m_{remaining}}{M_{NiO}} \tag{2.2}$$

Here m_{tot} is the total mass of loaded sample, m_{Ni} is the calculated weight of Ni, M_{Ni} is the molar mass of Ni, $m_{remaining}$ is the amount of mass remaining at the end of the TGA measurement and M_{NiO} is the molar mass of NiO. It should be noted that although most carbon would burn and produce CO_2 or CO, some ash would still remain. This means that weight percentages determined in this way were typically slightly higher than the actual value should be. A sample where only the GNP500 support material was present was also measured in this manner.

2.2.4 Infrared spectroscopy (IR)

Infrared spectroscopy was performed using a PerkinElmer FT-IR Spectrometer using a Universal ATR Sampling Accessory. Typically, a small spoonful of sample was placed on the ATR crystal. Infrared light with a MIR (8000-30) cm^{-1} source was passed through a OptKBr (7800-400) cm^{-1} beamsplitter and detected using a $LiTaO_3$ detector.

2.2.5 X-ray diffraction (XRD)

Crystal phases and crystallite sizes of bulk material are identified using X-ray diffraction. X-ray diffraction patterns were acquired in air using a Bruker AXS D2 Phaser diffractometer. All diffraction measurements were performed using an X-ray source 30 kV and 10 mA. Samples were first crushed to a fine powder using a mortar and pestle. Co K$\alpha_{1,2}$ with $\lambda = 1.79026$ Å radiation was used to irradiate the samples. Measurement step sizes and times were varied from sample to sample to obtain sufficient resolution and signal-to-noise ratio. Crystallite sizes were determined using the Scherrer equation, shown in Equation (2.3):

$$d_c = \frac{0.89\lambda}{\beta \cos\theta} \tag{2.3}$$

Here d_c is the crystallite size, λ was the X-ray wavelength, β is the full width at half maximum of the investigated reflection and θ is the Bragg angle of the investigated reflection.

2.2.6 Inductively coupled plasma spectroscopy - optical emission spectroscopy (ICP-OES)

ICP-OES measurements were performed by Mikrolab, Mikroanalytische Laboratorium Kolbe c/o Fraunhofer-Insitut UMSICHT in Oberhausen. These measurements were used to determine the wt-% of Ni in some silica-based samples, as well as the C or P wt-% in some samples.

2.2.7 Nitrogen physisorption

The surface area of the samples were measured using Micromeritics® TriStar II Plus Physisorption Analyzer. Measurements were performed at 77.35 K after vacuum drying at 180 °C for 2 hours. Adsorption and desorption isotherms were used to determine the Brunauer-Emmett-Teller (BET) isotherm and its corresponding surface area. The influence of various heat treatments under N_2, O_2 and H_2 on the BET surface area was investigated. Pore volumes calculated using Barett-Joyner-Halenda (BJH) analysis were used to determine the impregnation volume for IWI.

2.3 Catalysis

2.3.1 Catalyst preparation

Catalytic test were performed using an Avantium Flowrence. This particular device was a parallel fixed bed reactor system, including 4 individual temperature blocks, each of which housed 4 reactors, for 16 reactors in total. Reactors have an inner diameter of 2.6 mm and an isothermal zone of up to 0.3 mL. Typically, the catalyst powder was first pelletized at 1 ton for 30-60 seconds, after which it was sieved into fractions of 75-150 µm.

The reactors were first loaded with 0.5 cm of silicon carbide (SiC) in a sieve fraction of 212-400 µm. A small amount of catalyst material (30 or 60 mg) was diluted with 4 times with SiC, to prevent the formation of hot spots during catalysis. The reactors were then loaded with this mixture and finally the reactors were loaded with approximately 3 cm of SiC. The difference in sieve fractions of the SiC and the catalyst allowed for easy separation after catalysis.

2.3.2 Catalytic testing

After loading the reactors, the catalysts were reduced again in a 20 % H_2/N_2 flow at 250 °C for 2 hours with a temperature ramp of 2 °C/min. This temperature was purposely chosen to be lower than the used reduction temperatures in the reduction treatment of the precatalyst to make sure the catalyst in the Flowrence remained as similar to the catalyst as loaded in the reactor before the re-reduction. Following this, the temperature was lowered to 140 °C, the flow was switched to a CO_2/H_2 with He as an internal standard mix and the setup was pressurized to 30 bar. The used reaction mixture was composed of a 4:1 H_2:CO_2 mixture with 5 vol-% He which was used as an internal standard. Reaction conditions were based on previous catalytic tests performed on carbon supported Ni NPs of similar wt-%. An appropriate volumetric flow rate of 100 mL/min of the premixed reaction mixture was divided using a glass chip over the 16 reactors, resulting in a flow rate of approximately 6.25 mL/min per reactor. The gas flows exiting the reactors were then diluted with N_2, which prevents backflow of the gases into the reactors and leads the reaction gases to the online Agilent Technologies 7890B Gas Chromatograph system. The components of gas stream were identified using a TCD and a flame ionization detector (FID). For a GC cycle, a single measurement was performed for each reactor. Each GC cycle took about 4 hours, with an individual measurement taking 14 minutes to complete. In each test, at least one reactor was loaded with only SiC and another with a reference catalyst.

Activity test

The influence of temperature on the catalytic performance of the loaded catalysts was tested. The used temperature program is shown in Section 2.3.2. First, the catalysts were reduced according to the treatment described above. Then, the catalysts were in order brought to 240 °C, 340 °C, 320 °C, 300 °C, 280 °C, 260 °C, 250 °C and finally again to 240 °C. This temperature program was chosen so that the catalysts experience the most extreme circumstances initially, as it was probable that most Ni NP restructuring would take place at this temperature. Four measurements were taken at the first two temperatures to monitor the potential variation in conversion and selectivity, and three measurements at each following temperature. A volumetric flow rate of 100 mL/min of reaction mixture was divided over the 16 reactors using a glass chip, resulting in a flow rate of approximately 6.25 mL/min per reactor. This corresponded to a gas hourly space velocity of approximately 6000 mL ${g_{cat}}^{-1}$ s^{-1}.

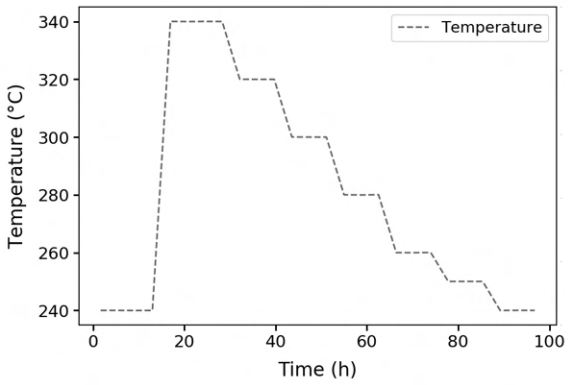

Figure 2.2: Temperature program used for activity tests.

Combined activity and stability test

In this test, several catalysts were tested according to the temperature program shown in Section 2.3.2 in addition to other catalysts at a constant 300 °C. This was done to simultaneously investigate activity and stability of different catalysts. This mixed test was achieved in the Flowrence by placing the 16 reactors in the four reactor blocks, which could be heated individually. So, the 8 reactors used for an activity test were placed in reactor blocks 1 and 2, and the 8 reactors used for a stability test could be placed in reactor blocks 3 and 4. For both sets of reactor blocks, a single reactor was present loaded with only SiC. The test was performed as such that the temperatures of the reactor blocks (3 and 4) reached either 300 °C for the stability test or 240 °C for the activity test (1 and 2) at the same time. A volumetric flow rate of 50 mL/min of reaction mixture was divided over the 16 reactors using a glass chip, resulting in a flow rate of approximately 3.125 mL/min per reactor. This corresponded to a gas hourly space velocity of 6000 mL ${g_{cat}}^{-1}$ s^{-1} for the silica catalysts and a gas hourly space velocity of 3000 mL ${g_{cat}}^{-1}$ s^{-1} for the carbon catalysts.

2.3.3 Data analysis

The catalytic data presented in Chapter 6 was analysed according to equations and definitions shown below.

CO_2 conversion

The conversion of CO_2 was determined according to the following formula:

$$X_{CO_2}\ (\%) = \frac{F_{CO_2,i} - F_{CO_2,f}}{F_{CO_2,i}} * 100\% \tag{2.4}$$

Here $F_{CO_2,i}$ is the initial CO_2 molar flow rate (mol/s) and $F_{CO_2,f}$ is the exiting molar flow rate. The molar flow rate was determined according to the following formula:

$$F_x(mol/s) = \frac{v_x}{V_M} \tag{2.5}$$

Here v_x is the volumetric flow rate (L/s) and V_M is the molar volume (L/mol) with a value of 22.414 L/mol at STP. The exiting volumetric flow rate of CO_2 was determined using a GC with He as an internal standard. The entering volumetric flow rate of gases was determined by using the exiting volumetric flow rate of He over the reactors filled with only SiC at the corresponding temperature.

Selectivity

Selectivities of catalysts towards certain products were determined by the following formula:

$$S_x\ (\%) = \frac{F_{x,f}}{\Sigma_i\ i * F_{C_iH_aO_b,f}} \tag{2.6}$$

Here $F_{x,f}$ iss the exiting molar flow rate of compound x, and $\Sigma_i\, i * F_{C_iH_aO_b,f}$ is the sum of all exiting molar flow rates of carbon containing compounds where each individual flow rate was multiplied by the amount of carbon atoms present in the relevant compound to account for stoichiometry.

Activity

The activity of a catalysts was expressed in mol CO_2 converted per second per gram of Ni (mol_{CO_2} s^{-1} g_{Ni}^{-1}) and calculated according to:

$$Activity\ (mol_{CO_2} s^{-1} g_{Ni}^{-1}) = \frac{F_{CO_2,i} - F_{CO_2,f}}{wt_{Ni} * mass_{cat}} \tag{2.7}$$

Here wt_{Ni} is the weight percentage of Ni in the loaded catalyst and $mass_{cat}$ is the amount of loaded catalyst in grams.

Turnover frequency

The turnover frequency (TOF) was expressed in the number of moles of CO_2 that were converted per mole of surface Ni per second and was calculated according to:

$$TOF\ (mol_{CO_2}\ mol_{surf\_Ni\_atoms}^{-1}\ s^{-1}) = \frac{F_{CO_2,i} - F_{CO_2,f}}{Ni_{surf\_atoms}} \tag{2.8}$$

Here Ni_{surf_atoms} is the amount of Ni surface atoms in moles for a given catalyst for a known weight loading and loaded amount of catalyst.

Nickel surface atoms

The amount of Ni surface atoms in a catalyst with a mass of $mass_{cat}$ (in g), a Ni weight loading of Ni_{wt} (in wt-%) and an average particle size of PZ (in nm) was calculated using the following formulas. First the amount of Ni in mol was calculated:

$$\text{Ni (mol)} = \frac{mass_{cat} * Ni_{wt}}{M_{Ni}} \tag{2.9}$$

Here M_{Ni} is the molar mass of nickel in g/mol. Next, the amount of particles (AOP) of size PZ necessary to obtain this amount of Ni was calculated:

$$\text{AOP (mol)} = \frac{Ni_{mol} * V_{Ni}}{PZ^3 * \frac{\pi}{6} * N_A} \tag{2.10}$$

Here V_{Ni} is the molar volume of Ni ($6.59*10^{21}$ nm^3/mol). Finally, the amount of surface particles could be calculated according to:

$$Ni_{surf\_atoms}\ \text{(mol)} = AOP * \frac{(PZ_{outer}^3 - PZ_{inner}^3) * \frac{\pi}{6}}{V_{Ni}} \tag{2.11}$$

Here PZ_{outer} is the measured particle size PZ and PZ_{inner} is the particle size without the outermost Ni atoms, which was equal to PZ - $2 * 0.124$ nm.

Activation energy

The activation energy E_a could be determined by first determining the specific reaction rate k through the Arrhenius equation:

$$k = A * e^{\frac{-E_a}{RT}} \tag{2.12}$$

Here A is a preexponential factor, E_a is the activation energy (J/mol), R is the universal gas constant (8.314 J mol^{-1} K^{-1}) and T is the temperature (K). Taking the natural logarithm of this equation, the following was obtained:

$$\ln k = \ln A - \frac{-E_a}{R} * \frac{1}{T} \tag{2.13}$$

Assuming first order reaction kinetics, where the specific reaction rate depends on the reaction rate (mol_{CO_2} s^{-1} g_{Ni}^{-1}) and the concentration [CO_2]. The specific reaction rate k could then be calculated assuming according to:

$$k = \frac{-r}{[CO_2]} \tag{2.14}$$

The concentration [CO_2] was determined based on the total volumetric flow rate v and the conversion of CO_2 for a specific catalysts at a specific temperature, according to:

$$[CO_2] = \frac{F_{CO_2,i}(1 - X_{CO_2})}{v} \tag{2.15}$$

Finally, plotting k against reciprocal temperature 1/T (K−1), a straight line was obtained, of which the slope is equal to $-E_a/R$. This allows for a straightforward calculation of the activation energy E_a.

Chapter 3

Colloidal synthesis of nickel nanoparticles

The use of colloidal nanoparticles in heterogeneous catalyst synthesis has several advantages over conventional catalysts preparation methods like co-precipitation, incipient wetness impregnation and deposition precipitation. Advantages include the excellent control that can be obtained over the size, shape and composition of the nanoparticles [2]. Many different parameters can be varied to influence nanoparticle size and shape, such as the nature of the reducing agent and ligand, as described in Section 1.2.1. Utilising a strong reducing agent typically improves nucleation rates, and thus yields smaller more monodisperse nanoparticles. Similarly, strongly binding ligands such as trioctylphosphine (TOP) also decreases the accessibility of a colloidal nanoparticle surface, limiting nanoparticle growth which results in small nanoparticles. However, changing the reducing agent or ligand introduces new potential problems. In the case of ligands, different ligand removal strategies might need to be employed. For Ni NPs synthesized by using TOP for example, the TOP is challenging to remove from the surface and phosphorous even is incorporated in the Ni nanoparticle lattice at low temperatures [27,69]. Therefore, to study Ni nanoparticles, it is interesting to attempt phosphorous-free colloidal synthesis. Experimental conditions, such as precursor, ligand and reducing agent concentration, temperature and heating ramps can also be varied, which have the advantage that no new chemicals are introduced in the system, allowing for easier comparison of various experiments. In this chapter, the results from the employed synthesis strategies described in Section 2.1.2 are presented. In order to control Ni nanoparticle size via colloidal synthesis, methods based on earlier works were used. Metin et al synthesized small 4 nm seeds by a hot-injection method where they rapidly added borane tert-butylamine (BTB) complex dissolved in oleylamine (OAm) to a solution of nickel acetylacetonate ($Ni(acac)_2$) in OAm and oleic acid (OAc) [58]. Vrijburg et al further developed this synthesis method and obtained 6-8 nm Ni nanoparticles through a seed-mediated growth method. Here, they grew the Ni seeds by slowly adding additional $Ni(acac)_2$ precursor in octadecene (ODE) and OAc at elevated temperatures [3]. Larger 20 nm Ni nanoparticles were obtained by Tzitzios et al through a heating-up method of $Ni(NO_3)_2.6H_2O$ in polyethylene glycol with a molecular weight of 400 g/mol (PEG400) [59]. Large polydisperse 50-80 nm Ni NPs were obtained by Carenco et al through heating up method of $Ni(acac)_2$ in OAm [26]. In addition, Carenco et al obtained a large size range (3-20 nm) of monodisperse Ni NPs by heating up method of $Ni(acac)_2$ in OAm and TOP [26]. The methods developed by Vrijburg et al and Metin et al were primarily used to obtain most colloidal Ni NPs used in further experiments, as they yielded different particle sizes of 4 and 8 nm. These particles were synthesized without using any phosphorous containing compounds. The various methods described are used to answer the following research questions:

- Can we control the Ni nanoparticle size and shape through hot-injection and seed-mediated growth using OAm and OAc as ligands?
  - What is the influence of the Ni precursor concentration on the final size and shape?
  - What is the influence of increasing the added Ni precursor?
- Can we controllably synthesize large (> 7 nm) Ni nanoparticles without using phosphorous-containing ligands?

- What influence does the ligand choice have on our final Ni nanoparticle size and shape?
- What influence does the synthesis method have on our final Ni nanoparticle size and shape?

The particles synthesized in this chapter were subsequently used to obtain the catalysts that are used in Chapter 6.

3.1 Results and discussion

3.1.1 Oleylamine route

Oleylamine only

The first method discussed to obtain Ni NPs was a heating-up method (Section 2.1.2). Here, a solution of $Ni(acac)_2$ in OAm was heated to 230 ˚C and kept at this temperature for 10 minutes. This resulted in particles with a mean size of 32.5 ± 7.6 nm, determined from the TEM image shown in Figure 3.1a. This was very similar to experiments done by Carenco et al, where similar large and polydisperse Ni NPs of various shapes were obtained when performing a heating-up type experiment using only OAm and $Ni(acac)_2$ [26]. The authors rationalise this by taking OAm to be a good reducing agent but a poor capping agent [26]. In the work by Vrijburg et al however, the particles remain small when only using OAm but including borane tert-butylamine complex as a reducing [3]. This indicates that although OAm is a sufficient capping agent, its function as a reducing agent is limited. A possible explanation for the observed broad size distribution could be that the nucleation of the Ni NPs already started at lower temperatures and proceeded inhomogeneously as the mixture was heated up to 230 ˚C. This results in limited separation of the nucleation and growth step (Phase II and III in Figure 1.2), yielding large particles with a broad size distribution. This hypothesis was tested by a hot-injection method (Section 2.1.2), where a solution of $Ni(acac)_2$ in OAm at a temperature of 90 ˚C was injected into preheated OAm, ensuring a fast temperature ramp and possibly more homogenous nucleation. TEM image of the experiment are shown in Figure 3.1b give a mean particle size of 19.2 ± 4.8 nm. A comparison between this result and the heating-up method shown in Figure 3.1a reveals many similarities. Both show polydisperse particles with a broad size distribution which agglomerate, although they remain separate particles. The particles obtained with the hot-injection method were smaller compared to the particles from the heating-up method, but their shape was still irregular. This indicates that the applied method is not effective in increasing the nucleation rate sufficiently to obtain monodisperse nanoparticles. In both cases, the supernatant found after centrifugation was still slightly greenish. This indicates incomplete reduction of the $Ni(acac)_2$ complex, which was observed as an emerald green fluid when dissolved in OAm. Both syntheses resulted in particles that were not very stable in suspension, as after several weeks, a large black solid was observed precipitated at the bottom of the glass vial with clear toluene, in stark contrast to the black suspension that was obtained directly after synthesis. Sonication did not redisperse the particles.

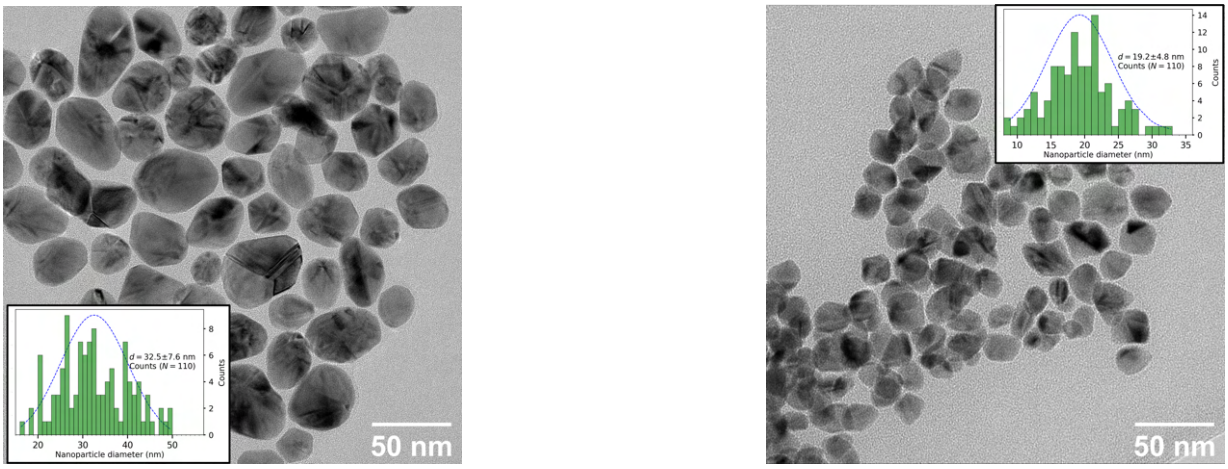

(a) (b) .

Figure 3.1: TEM images of Ni colloids. a) Sample was made by heating-up method (Section 2.1.2) at 230 ˚C. Clustered particles with a broad size distribution and various shapes were observed, with an average particle diameter of 32.5 ± 7.6 nm. b) Sample was obtained by hot-injection method (Section 2.1.2) at 230 ˚C. Clustered particles with a broad size distribution and various shapes were observed, with an average particle diameter of 19.2 ± 4.8 nm

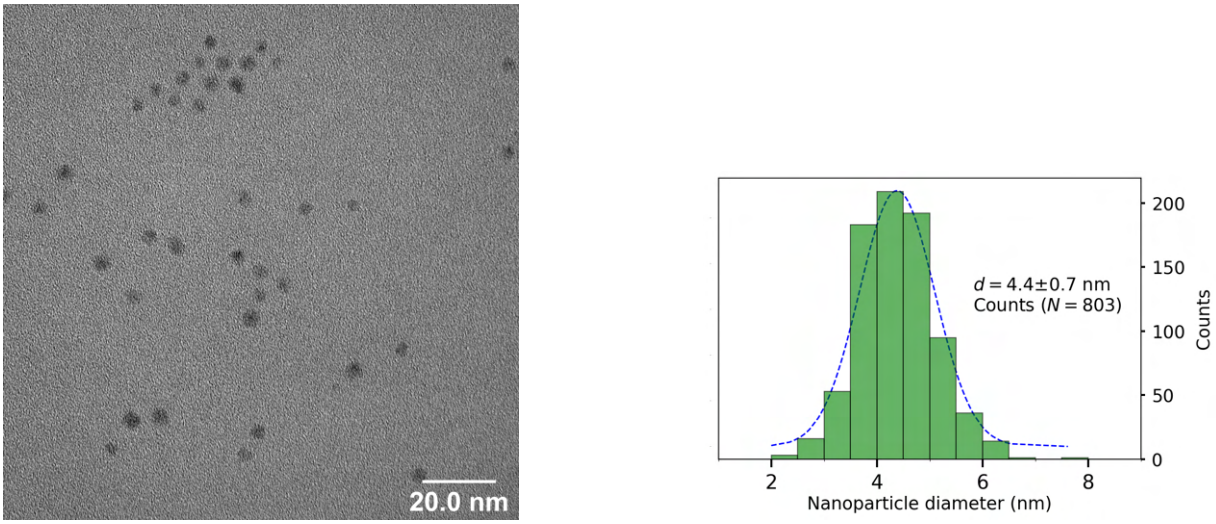

(a) (b)

Figure 3.2: TEM and corresponding Ni nanoparticle size distribution. Sample was made by hot-injection with BTB (Section 2.1.2) at 90 °C. a) TEM image of Ni colloids. Monodisperse Ni nanoparticles with a mean size of 4.4 ± 0.7 nm are found. b) Size distribution of Ni colloids shown in Figure 3.2a. Distribution corresponds to a normal distribution.

Hot-injection with borane tert-butylamine complex

To obtain smaller particles with a more narrow size distribution without resorting to phosphorous containing ligands, a different method was applied. This method, which was based on a literature procedure by Metin et al, involved the use of a reducing agent, BTB. This increased the nucleation rate of the reaction to and resulted in well-defined particles with a narrow size distribution [58]. Shown in Figure 3.2a is a TEM image of the particles obtained with a BTB/Ni(acac)$_2$ ratio of 5 at 90 °C after 60 min. The associated distribution is shown in Figure 3.2b These monodisperse particles had a mean particle size of 4.4 ± 0.7 nm, as determined using TEM. They were well separated and remained in suspension even after a long time. This was in stark contrast to the particles shown in Figures 3.1a and 3.1b. The small 4.4 nm Ni nanoparticles synthesized here (further referred to as Ni seeds) could only reliably be precipitated by centrifugation by using at least 8000 RPM and were readily redispersed in toluene. If the samples were centrifuged at lower RPM, the supernatant remained black, indicating the presence of still suspended Ni seeds. This is an indication of their small size, as smaller particles are more difficult to precipitate. Further experiments repeating this procedure consistently reproduced these small Ni seeds (Figures A.12 and A.13).

Seed-mediated growth

Larger Ni NPs were obtained through a seed-mediated approach as developed by Vrijburg et al [3]. The synthesis procedure, as described in Section 2.1.2, proved to be reproducible and robust, similarly to the Ni seeds synthesis. Depicted in Figure 3.3a is a TEM image of the larger Ni NPs synthesized by slowly adding additional Ni(acac)$_2$ precursor at a rate of 0.1 mL/min(here, double the amount of Ni(acac)$_2$ that was initially used for the seeds synthesis is added over time). This rate was slower than used by Vrijburg et al (0.5 mL/min), to enhance homogeneous growth of the Ni NPs. The particles had an average particle size of 6.5 ± 1.7 nm and remained well-separated. The size distribution is shown in Figure 3.3b, which was broader than that observed for the Ni seeds (a dispersion of 26% compared to 16%). Additionally, during centrifugation, the larger particles proved to be much easier to precipitate, although in most cases 8000 RPM was still used to centrifuge the larger Ni NPs. Two parameters were varied to increase particle size,. First, the concentration of Ni(acac)$_2$ in the growth solution was varied. Secondly, the ratio of the amount Ni precursor in the growth solution compared to the amount of Ni precursor in the seed solution was varied. The results of the concentration variation are shown in Figure 3.4 and the ratio variation in Figure 3.5. Corresponding

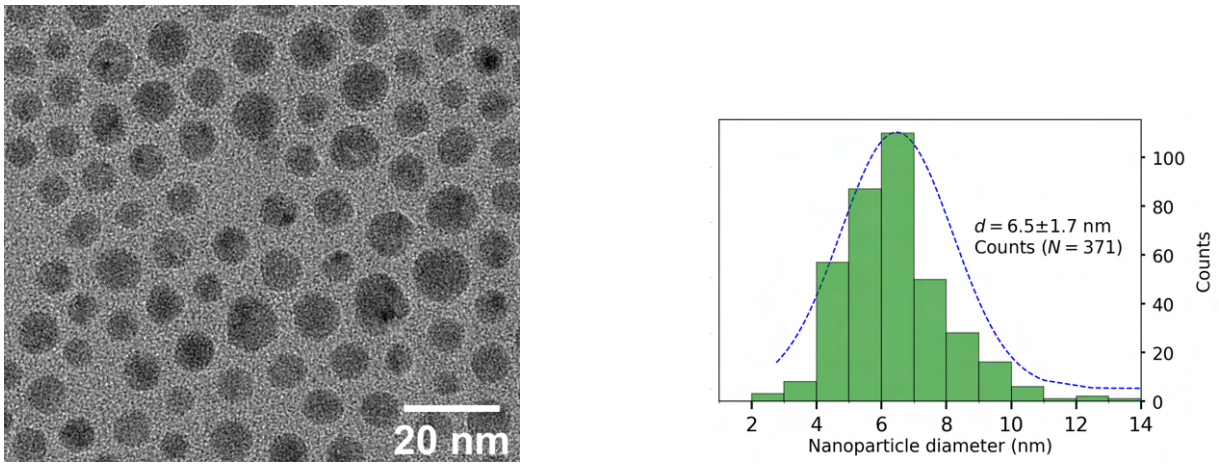

(a) (b)

Figure 3.3: Sample was made by hot-injection with BTB at 90°C and subsequent growth at 200°C by slow addition of $Ni(acac)_2$. Particles have a mean size of 6.5 ± 1.7 nm. a) TEM image of larger Ni colloids. b) Corresponding size distribution of larger Ni colloids.

TEM images and size distributions are shown in Figures A.7 to A.10. In all cases the temperature was kept at 200 ± 5 °C. This allows for direct comparison of different samples. The Ni nanoparticle size increased with increasing concentration of $Ni(acac)_2$ as seen in Figure 3.4. This can be related to the increasing growth rates at higher concentrations, according to Section 1.2.1. A broader size distribution is observed for the particles after seed-mediated growth, independent of whether the average size had increased. Higher concentrations of $Ni(acac)_2$ in the growth solution are difficult to achieve when using ODE, as dissolving the $Ni(acac)_2$ in ODE was already difficult even at 110 °C and after evaporation of water. Similarly to the Ni seeds, the larger Ni NPs also remained suspended in toluene even after several weeks and are thus stable in solution, in contrast to those synthesized according to Section 2.1.2. A complete overview of all colloids synthesized using this approach is given in Table 3.1. Decreasing the concentrations of $Ni(acac)_2$ in the growth solutions appeared to limit the growth rate so much that almost no particle growth was observed. Higher concentrations than those described could not be investigated due to the limited solubility of $Ni(acac)_2$ in ODE. Addition of more $Ni(acac)_2$ equivalents did not appear to grow much larger particles. It is possible that for larger sizes, much more $Ni(acac)_2$) needs to be added. To confirm this, a much larger amount of $Ni(acac)_2$ equivalents can be added for a future experiment.

3.1.2 Polyol route

To obtain even larger particles without using P-containing ligands, a synthesis based on a method proposed by Tzitzios et al [59] was attempted (Section 2.1.2). This resulted in the particles shown in Figures 3.6a and 3.6b. Particles had a large average size of 20 ± 5.0 nm and were irregularly shaped. Careful investigation of TEM images revealed separate, but strongly aggregated particles. This can be an indication of insufficient solubility of the PEG400 in toluene, or the magnetic properties of the Ni nanoparticles. The strong aggregation and broad distribution meant this particular method not a promising approach to controllably synthesize larger Ni nanoparticles.

3.1.3 Trioctyl phosphine route

For later comparison between catalyst materials, 7 nm Ni NPs were also synthesized using TOP via the method outlined in Section 2.1.2. This colloidal suspension was also readily precipitated by centrifugation at 8000 RPM and was easily redispersed in toluene.

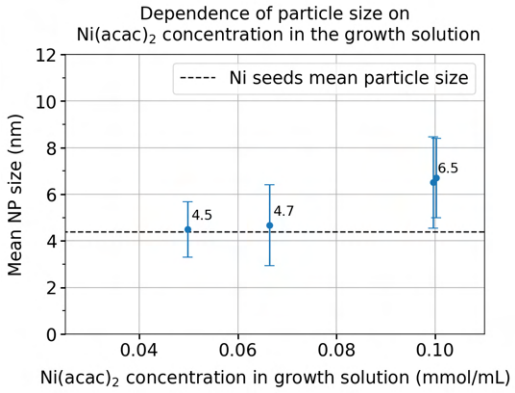

Figure 3.4: Average particle size plotted against $Ni(acac)_2$ concentration in the growth solution. The dotted black line indicates the average size of the Ni seeds. By varying the $Ni(acac)_2$ concentration in the growth solution, small size increase is observed relative to the nickel seeds. Corresponding TEM images and size distributions are shown in Figures A.7 and A.8

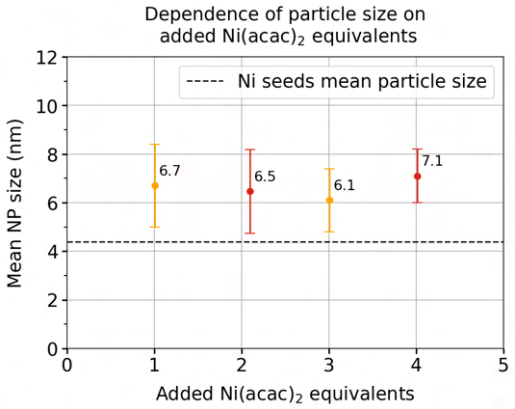

Figure 3.5: Average particle size plotted against the amount of added $Ni(acac)_2$ equivalents. The samples in red both had an initial concentration of approximately 0.20 mmol/mL and the samples in orange of 0.10 mmol/mL. No significant particle growth was observed as a function from added $Ni(acac)_2$ equivalents. Corresponding TEM images and size distributions are shown in Figures A.9 and A.10

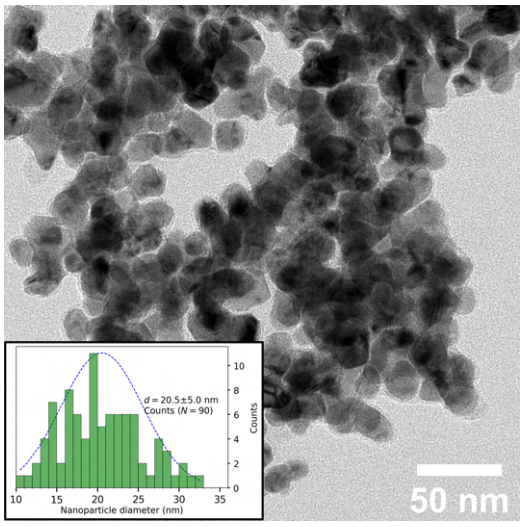

(a)

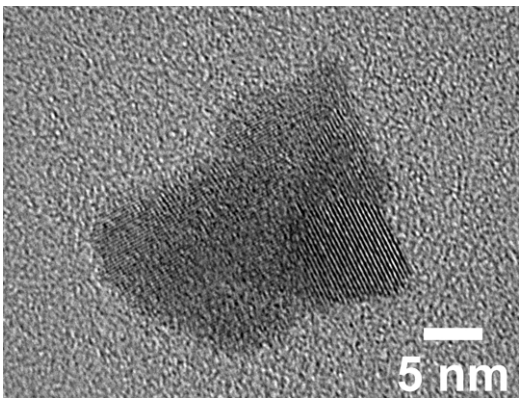

(b)

Figure 3.6: TEM images of Ni nanoparticles synthesized through polyol method at 215 °C. a) TEM image of Ni NPs with an average size of 20 ± 5.1 nm and irregular shapes. b) High resolution TEM image of a single Ni NP synthesized through polyol method. Ni lattice spacing appears visible in the bottom right of the NP.

Table 3.1: Overview of all seed-mediated growth samples

Mean size (nm)	Concentration in growth solution (mmol/mL)	Ni(acac)2 ratio growth/seeds
4.5 ± 1.2	0.05	1.00
4.7 ± 1.7	0.07	0.99
6.5 ± 2	0.10	1.00
6.7 ± 1.7	0.10	1.01
6.1 ± 1.3	0.10	3.01
6.5 ± 1.7	0.20	2.09
7.1 ± 1.1	0.20	4.01

3.2 Conclusions

In this chapter, the synthesis of colloidal Ni NPs through several methods is discussed. Through extensive experimentation, methods were developed to reliably and reproducibly synthesize Ni NPs. 4 nm Ni seeds were synthesized by hot-injection of BTB into a solution of $Ni(acac)_2$ in OAm and OAc. These particles proved to be stable in suspension in toluene. Using a seed-mediated growth method, larger 7 nm Ni NPs were synthesized by slow addition of $Ni(acac)_2$ dissolved in ODE. By changing the concentration of $Ni(acac)_2$ in ODE, larger particle could be obtained. Very low concentrations of $Ni(acac)_2$ (0.7 mmol/mL) resulted in almost no growth of the Ni seeds. Increasing the total amount of $Ni(acac)_2$ added via seed-mediated growth without changing the concentration appeared to have no discernible influence on the particle size. Large 30 nm Ni NPs with a broad size distribution and irregular shapes were also synthesized using a heating-up method in only OAm. Repeating this experiment and attempting a hot-injection method succeeded in decreasing the average particle size to 19 nm. This demonstrated the influence that a colloidal synthesis method can have on the growth of Ni nanoparticles in OAm. The particles still showed a broad size distribution and irregular shapes and aggregate into large clusters of Ni nanoparticles. Changing the ligand to PEG400, the precursor to $Ni(NO_3).6H_2O$ and performing a heating-up synthesis resulted in 20 nm particles with a broad size distribution. These particles also clustered together and were not well dispersed in toluene. We can conclude that the methods used to prepare larger Ni nanoparticles without using phosphorous-containing ligands were ineffective in obtaining monodisperse and well separated Ni nanoparticles. Finally, 7 nm Ni NPs were synthesized through a heating-up method where TOP was used a ligand and OAm as a reducing agent. To summarize, we were able to prepare 4 and 7 nm Ni nanoparticles without making use of phosphorous-containing ligands. These 4 and 7 nm Ni nanoparticles were then used to prepare catalysts as described in Chapter 4.

3.3 Outlook

Obtaining a broad size control of Ni NPs using colloidal synthesis without resorting to P-containing ligands remains a significant challenge and might thus be interesting for further research. Although a limited size control was achieved, both smaller (4 < nm) and larger (> 7 nm) monodisperse Ni NPs remain out of our reach. An additional seed-mediated growth experiment can be attempted where a very large amount of $Ni(acac)_2$ (relative to the $Ni(acac)_2$ used for the seeds synthesis) is added through slow-addition, which might yield larger particles. For future investigation, this synthesis procedure might also be attempted using different ligands. Preferably, these ligands should be long chain alkyl amines. This allows for easier adaptability of ligand removal strategies which are based on OAm. Sulphur and phosphorous-containing ligands should be avoided to prevent formation of nickel sulfides and nickel phosphides. Polyol synthesis was only performed here with PEG400. As the monodisperse size and size distrbution found in some polyol syntheses is generally ascribed to their viscosity [62], polyethylene glycol of higher molecular weight might improve Ni nanoparticle synthesis when using the polyol method. The nanoparticles now synthesized with PEG400 were dispersed in toluene. It might be interesting to see whether their dispersion improves when they are dispersed in water, as PEG400 is very soluble in water. Finally, the concentration of Ni colloids in the final solution obtained after washing is unknown, which complicates further catalyst synthesis. Developing a method to accurately quantify the Ni colloid concentration in a suspension could be of interest to further research.

Chapter 4

Preparation of supported nickel nanoparticles

This chapter highlights the majority of this thesis, which is the deposition of Ni colloids onto various supports, in addition to the activation of the deposited Ni NPs. Four different supports are investigated for colloidal deposition. This is done to study the potential different effects these supports may have on the deposition and activation steps, as well as to demonstrate the potential of colloids for research in heterogeneous catalysis. A final consideration made was that some supports allow for different types of characterization than others, broadening the potential information that can be obtained. The primary two supports were carbon based graphene nanoplatelets with an average BET surface area of 500 m^2/g and Davisil 643 silica with an average BET surface area of 300 m^2/g. The two other supports used here were alumina Al_2O_3 (200 m^2/g) support, which was chosen as alumina-based support materials are used for typical Ni methanation catalysts [44], and Aerosil 380V silica (380 m^2/g), which was used to approach the larger surface area of the GNP500 with a silica-based support material. A summary of measured physisorption data is shown in Table A.1. The methods used are described in Sections 1.2.3 and 2.1.3. This chapter aims to give answers to the questions shown below:

- Can we control the deposition of different sizes of Ni colloids whilst maintaining their size and size distribution?
  - What is the influence of the deposition method on the deposition of Ni colloids?
  - What is the influence of increasing the weight loading of Ni?
  - What is the influence of the support material?

Another key part of this chapter illustrates the removal of ligands and residual organic material that reside on the Ni nanoparticle surface after deposition. These ligands need to be removed to free up the Ni nanoparticle surface for access by reactants and to prevent the ligands from interfering with catalysis. In this thesis, thermal treatments are chosen to remove ligands, as these are easily applied across different supports and allow for comparison of the supported Ni nanoparticles synthesized through colloidal deposition with impregnation-based support Ni catalysts (which are also typically exposed to heat treatments). These heat treatments can influence the Ni nanoparticles and their effect on the prepared catalysts is also investigated. The chapter aims to answer the questions shown below:

- Can we remove the ligands and activate the Ni catalyst whilst maintaining their size and size distribution?
  - What is the influence of the heat treatments on the Ni NPs?
  - Can we remove the ligands and residual organic material by heat treatments?
  - What is the influence of the support material?

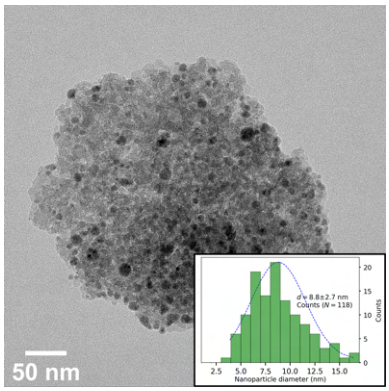

(a) TEM image of Ni(8.8)/SiO_2. Particles appear well-distributed across the support.

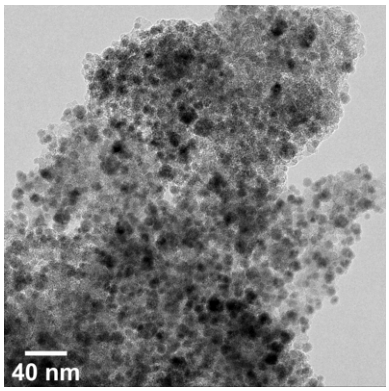

(b) TEM image of Ni(8.8)SiO_2. Particles appear well-distributed across the support. Some clustering is visible near the top and bottom right of this support particle.

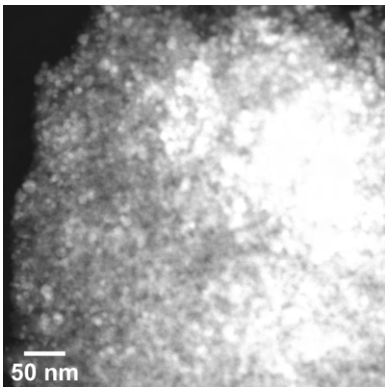

(c) HAADF-STEM image of 8.8 ± 2.7 nm Ni/SiO_2 with a wt-% of 0.81. This region was used for EDX-imaging.

Figure 4.1: TEM and HAADF-STEM images of 8.8 ± 2.7 nm Ni/SiO_2 with a Ni wt-% of 0.81 % prepared through a slow-evaporation method. wt-% is determined using ICP-OES. By comparison, TPR (using Equation (2.1) gave the same wt-% of 0.81). The corresponding TPR profile is shown in Figure A.15.

4.1 Results and discussion

4.1.1 Deposition of Ni NPs on various supports

The first attempt to deposit Ni colloids involved a slow-evaporation method, which was used to prepare supported Ni NPs. Experimental details are given in Section 2.1.3. In this method, a desired amount of support material is loaded into a flask, dried and a suspension of Ni colloids in toluene is injected into the same flask. The excess toluene is then evaporated overnight whilst stirring with a magnetic stirring bar. Shown in Figure A.11 are (S)TEM images of 4 nm nanoparticles supported on SiO_2. The supported Ni particles appear nearly identical to their colloidal counterparts shown in Figure 3.2a and have a similar size distribution (shown in Figure A.11d). Using TEM, an average particle size of 4.1 ± 0.8 nm was determined. No particles larger than 7 nm are found after deposition so maintaining the size of the Ni NPs was successful. EDX was performed on the particles visible in HAADF-STEM (shown in Figure A.11b) to confirm that these were indeed Ni nanoparticles, as shown in Figure A.11c. Some agglomerates of Ni in the (S)TEM images indicate that it is inhomogeneously distributed across the support. Visual inspection of samples prepared using the slow-evaporation method support this idea, as sample typically are grey to dark grey with some black spots, in contrast to the white colour of the Davisil 643.

Investigation into larger 7 nm Ni NPs supported on silica using the same method provided comparable results, shown in Figure 4.1. The average particle size of 8.8 ± 2.7 nm appeared slightly larger than the initial colloid sizes in Figure 3.3a, although this might also be a result from the difficulty in measuring the smaller 4 nm particles using TEM due to the relatively low contrast between the silica and the Ni NPs. The larger 7 nm particles also show the presence of aggregates of Ni nanoparticles. The larger 7 nm Ni NPs supported on carbon, of which TEM images are shown in Figure 4.2, show some interesting features. This sample, also prepared by a slow-evaporation method, shows three types of regions with different particle distributions across the support. First, a region with well-distributed Ni NPs is shown in Figure 4.2a. Particles are separated and found in both thin and thick parts of the sample. The next type of region is shown in Figure 4.2b, where many Ni NPs are found on the same part of the sample. Finally, a type of region where a very small amount of Ni NPs are found is shown in Figure 4.2c. These three types of Ni NP dispersions indicate that the deposition is not completely homogeneous. In contrast to the silica samples prepared in this manner, nearly empty regions were found. This might be attributed to the much larger surface area of the GNP500 used when compared to the Davisil 643, as well as the possibility that the stacking of the carbon platelets

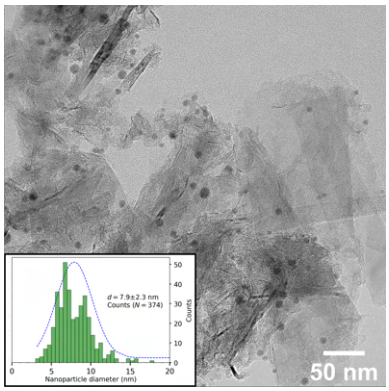

(a) A region of the sample with well-distributed Ni NPs.

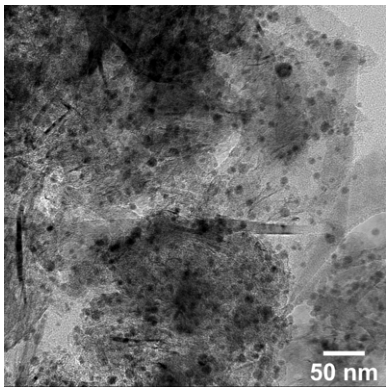

(b) A region with a high concentration of Ni NPs.

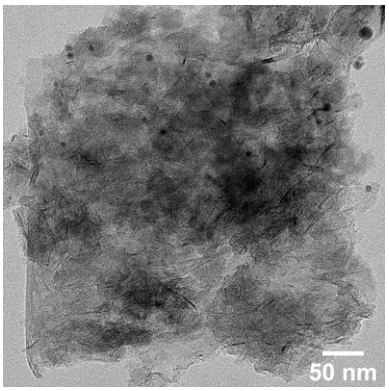

(c) A region of the sample that is nearly devoid of Ni NPs.

Figure 4.2: TEM images of 7.9 ± 2.3 nm Ni/GNP500 with a Ni wt-% of 1.4 % prepared through a slow-evaporation method. Ni wt-% is determined using TGA using Equation (2.2). Corresponding TGA profile is shown in Figure A.16.

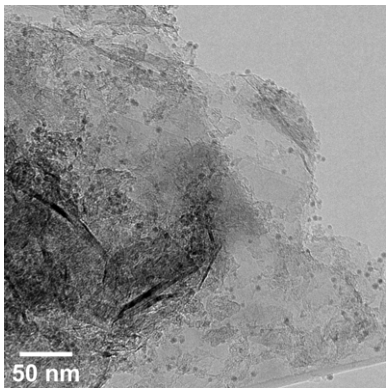

(a) A region of the sample with well-distributed 4 nm Ni seeds.

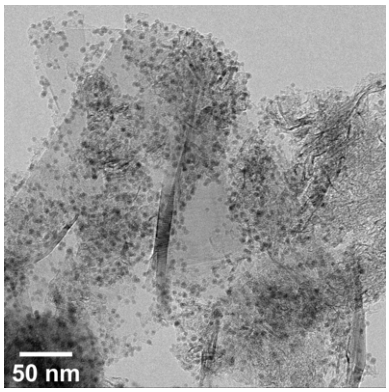

(b) A region with a high concentration of 4 nm Ni seeds. Some particles cluster together.

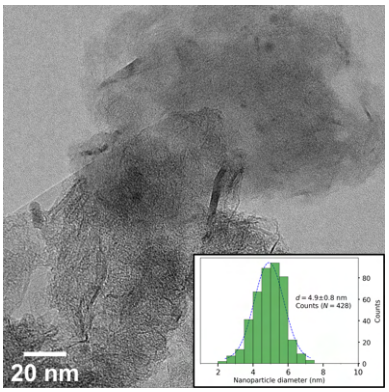

(c) A region of the sample that is nearly devoid of 4 nm Ni seeds.

Figure 4.3: TEM images of 4.9 ± 0.8 nm Ni/GNP500 with a Ni wt-% of 2.7 % prepared through a sonication-assisted deposition method. Ni wt-% is determined using TGA according to Equation (2.2). Corresponding TGA profile is shown in Figure A.17.

might prevent particles from depositing on certain parts of the GNP500. The average particle size is 7.9 ± 2.3 nm for the deposited particles, starting from the 6.5 ± 1.7 nm colloids which were presented in Figure 3.3a.

To obtain a more homogeneous dispersion of the Ni nanoparticles and to prevent a loss of the magnetic Ni NPs on the porous magnetic stirring bar during the slow-evaporation step, the sonication-assisted deposition method was used to obtain the next set of samples. First shown are samples prepared on GNP500, with the 4 nm Ni seeds on GNP500 shown in Figure 4.3 and the larger 7 nm Ni NPs on GNP500 in Figure 4.4. Interestingly, for both the seeds and the larger Ni NPs, the same three types of regions are observed. Shown in Figures 4.3a and 4.4a are the regions were the NPs are well-dispersed across the support area. Then, in some areas as shown in Figures 4.3b and 4.4b, a higher concentration of Ni NPs are observed. In particular, a big agglomerate of Ni NPs is found in Figure 4.4b. This is a rare occurrence in the sample, as most of the sample conforms to the other types of regions observed. These agglomerates might be a result from the NPs not being sufficiently separated in suspension, thus clustering together. A lower concentration of Ni NPs in toluene might therefore prevent formation of these agglomerates.

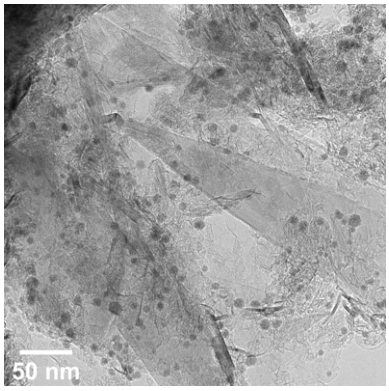

(a) A region of the sample with well-distributed 4 nm Ni seeds.

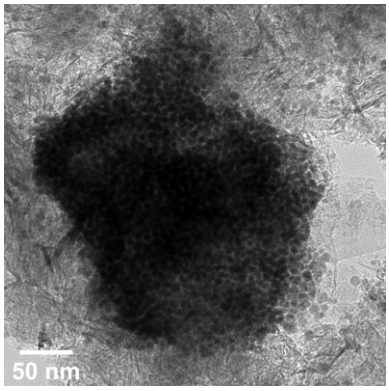

(b) An agglomerate of many Ni NPs.

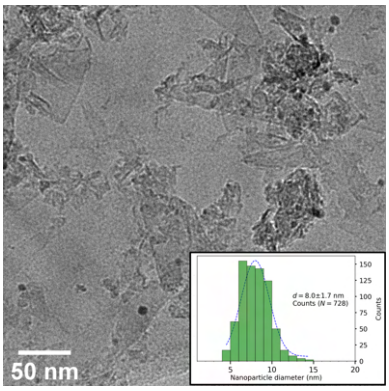

(c) A region of the sample that is nearly devoid of larger 7 nm Ni NPs.

Figure 4.4: TEM images of 8.0 ± 1.7 nm Ni/C with a Ni wt-% of 1.7 % prepared through a sonication-assisted deposition method. Ni wt-% is determined using TGA according to Equation (2.2). Corresponding TGA profile is shown in Figure A.18.

Figures 4.5a and 4.5b show Ni nanoparticles supported on Davisil 643 with an average particle diameter of 4.2 ± 0.7 nm and 8.8 ± 2.8 nm, respectively. The small 4 nm nanoparticles shown in Figure 4.5a appear well dispersed across the support material. The larger 9 nm nanoparticles shown in Figure 4.5b appear to have clustered near the top of the particle. Visual inspection of sample prepared using sonication-assisted deposition revealed a uniform gray or black colour, in contrast to the samples prepared with slow-evaporation. The 4 nm particles on SiO_2 shown in Figure A.11 and Figure 4.5a showed corroborating results. Ni agglomerates are no observed for the sample synthesized using sonication-assisted deposition(Figure 4.5a), whereas they are observed for the sample prepared using slow-evaporation(Figure A.11). ICP-OES and TPR calculations for the sample shown in Figure 4.5a (according to Equation (2.1)) give Ni wt-% of 1.51 and 1.96 % respectively. The larger amount of Ni calculated using TPR is probably caused by the hydrogen consumption of the support or ligand materials still present on the sample during TPR. The corresponding TPR profile is shown in Figure A.21. Figures 4.6a and 4.6b show TEM images of Ni NPs synthesized using TOP as a ligand after deposition on GNP500 and Davisil 643, respectively. On GNP500, clustering of Ni NPs is observed, in stark contrast with most regions found for the Ni NPs synthesized with OAm as a ligand. Particles appear very monodisperse and spherical in shape and have an average size of 7.3 ± 1.3 nm. On Davisil 643, clustering of the Ni nanoparticles is also observed, both at the edges of the support particle as well as in the centre. The particles had an average size of 7.4 ± 1.0 nm. This practically identical particle size and shape over the different supports illustrates the potential of preparing catalysts using colloidal synthesis. However, a major drawback was that deposition of Ni nanoparticles led to imhomogeneous dispersion of the particles across the various supports. This inhomogeneous dispersion of nanoparticles appears stronger for colloids synthesized using TOP.

Ni NPs were also deposited on SBa200 (alumina, Al_2O_3) (Figure 4.7a) and on Aerosil 380V (Figure 4.7b). Particles appeared inhomogeneously distributed across the Aerosil 380V support, with large parts of the support material remaining devoid of any particles, and some areas with larger concentrations of Ni nanoparticles as shown in the TEM images. Ni NPs supported on SBa200 were primarily located at the edge of support particles. The center of support particles was difficult to investigate due to the small contrast difference between the particles and the support. Preparing a similar sample using 7 nm nanoparticles might improve the contrast between the two, helping to investigate nanoparticle dispersion.

To summarize, it was possible to prepare Ni/C (Ni/GNP500), Ni/SiO_2 (Davisil 643, Aerosil 380V) and Ni/Al_2O_3(SBa200) using the methods mentioned in Section 2.1.3. Although the use of the sonication-assisted deposition method improved the dispersion of Ni nanoparticles (most notably visible in the silica samples), there were still some regions that contained inhomogeneously dispersed Ni nanoparticles. The stacking of the carbon platelets might be the cause, as they could prevent access by the colloidal particles. An experiment where toluene was first added without Ni colloids present to shake loose the GNP500 provided a similar re-

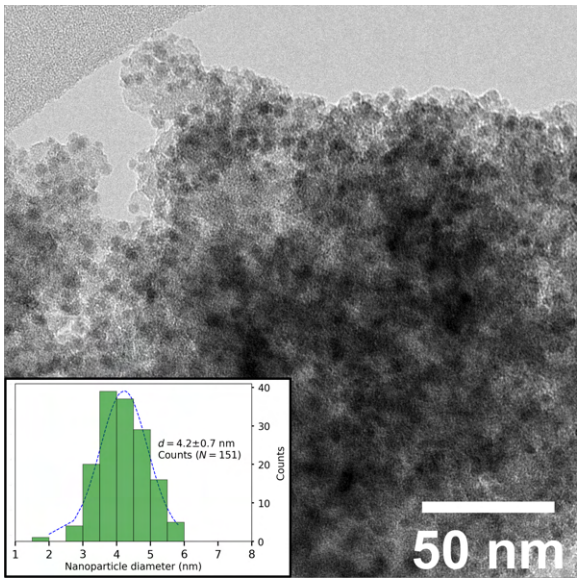

(a) Ni(4.2 ± 0.7)/SiO_2

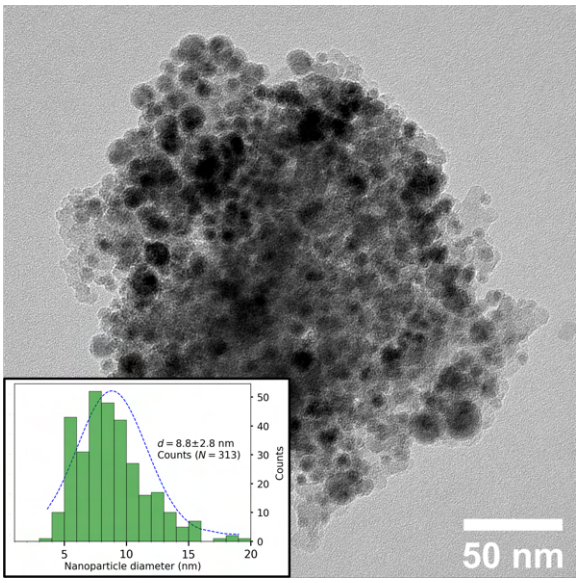

(b) Ni(8.8 ± 2.8)/SiO_2

Figure 4.5: TEM images of Ni nanoparticles deposited on Davisil 643 with a) 4.2 ± 0.7 nm Ni/Davisil 643 with a Ni wt-% of 1.51 % as determined by ICP-OES and 1.96 % as calculated using TPR data Equation (2.1). Corresponding TPR profile is shown in Figure A.21. b) 8.8 ± 2.8 nm Ni/Davisil 643 with a Ni wt-% of 0.69 % as calculated using TPR data according to Equation (2.1). Corresponding TPR profile is shown in Figure A.20.

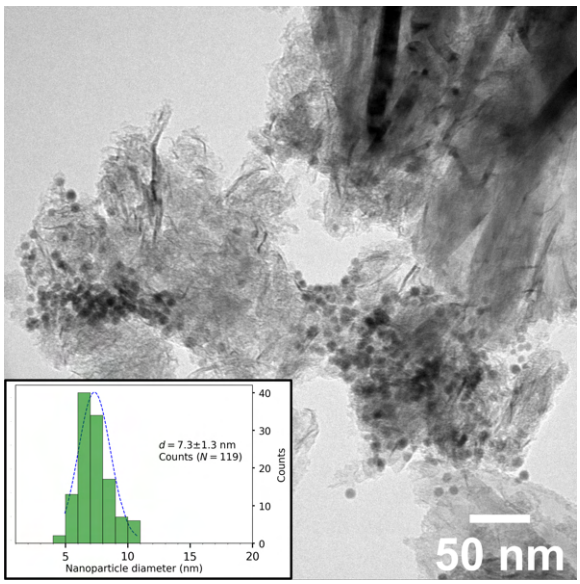

(a) Ni(7.3 ± 1.3 nm)/C

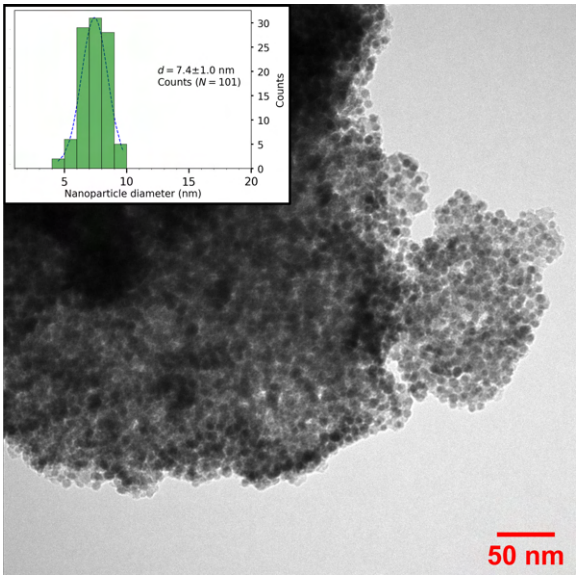

(b) Ni(7.4 ± 1.0 nm)/SiO_2

Figure 4.6: TEM images of supported Ni NPs synthesized with TOP supported on a) GNP500 and b) Davisil 643. Clusters of Ni NPs are observed for both Figures 4.6a and 4.6b.

sult(Figure A.22). Generally speaking, Ni nanoparticles appeared more well dispersed across the GNP500 support when compared to the other used supports. The worst dispersion of Ni nanoparticles is observed for the nanoparticles synthesized with TOP on both Davisil 643 and GNP500, and for the 4 nm Ni seeds on Aerosil 380V and SBa200. The big difference between the samples where TOP was used compared to the samples where only OAm and OAc were used as ligands is very likely caused by the ligands covering the surface. This might be caused by the nature of the ligands, where the double bond present in the OAm leads to a larger

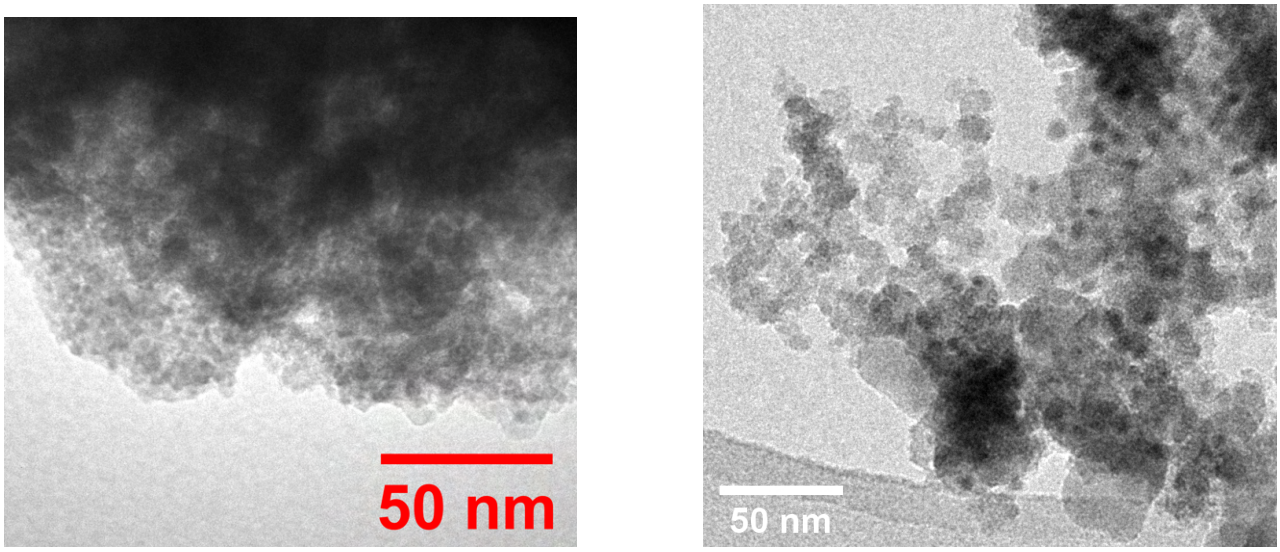

(a) (b)

Figure 4.7: TEM images of Ni NPs supported on a) SBa200 Al_2O_3 and b) Aerosil 380V SiO_2.

interparticle distance because of a larger extended ligand, which might prevent other ligand covered nanoparticles from approaching due to steric hindrance. In contrast, the trioctylphosphine might allow for nanoparticles to approach each other more closely, leading to more clustering. To test this, TEM images of Ni nanoparticles prepared using TOP as a ligand should be compared with images of similarly sized Ni nanoparticles prepared with OAm. In particular, the interparticle distance should be determined. For SBa200, the inhomogeneous dispersion of Ni nanoparticles could be explained through the too high concentration of Ni nanoparticles in the colloidal suspension used for deposition when taking into account the smaller surface area of the support material. This might have led to inhomogeneous dispersion of the Ni nanoparticles near the support particle edges, as the support material was already full. An experiment aiming for a much lower wt-% could test this hypothesis. The inhomogeneous distribution on the Aerosil 380V is of interest. Possibly, unfavourable interaction of the ligands with the surface groups of the SiO_2 lead to clustering of the nanoparticles. This could be investigated by functionalization of the silica with a more hydrophobic material, which could lead to a better interaction with the hydrophobic ligands and thus to better dispersion.

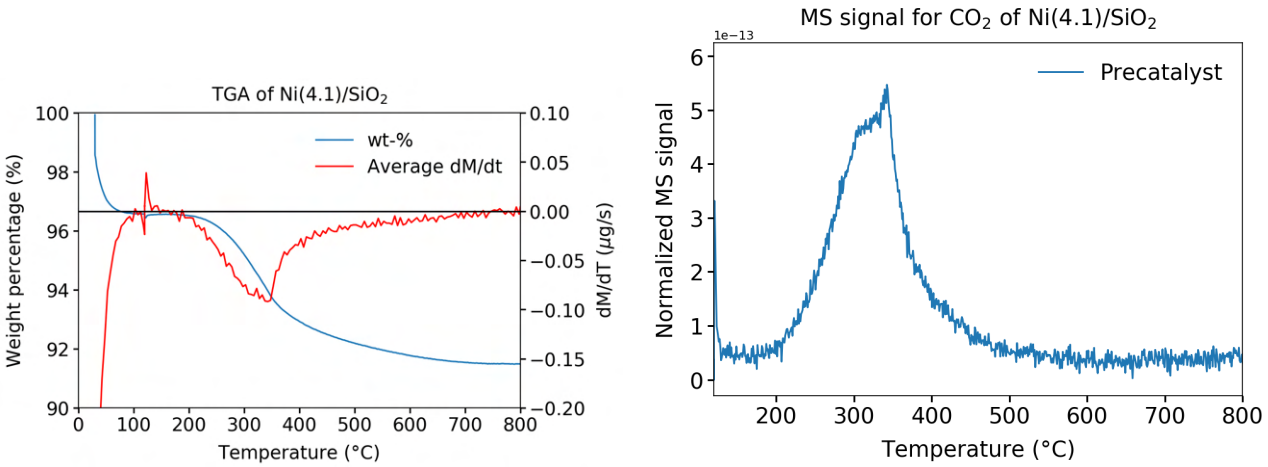

(a) (b)

Figure 4.8: TGA-MS data acquired for $Ni(4.1)/SiO_2$ with a Ni wt-% of 0.6 % in 20 % O_2. a) TGA profile of the sample. Mass loss is observed from 200 °C to 800 °C. The large average weight loss is found at around 340 °C. b) MS signal of CO_2 for the sample. Peak of CO_2 is centered around 340 °C. This corresponds with the largest average weight loss observed Figure 4.8a.

4.1.2 Determining heat treatments

As shown in Section 4.1.1, colloidal particles of several different sizes are deposited onto unique supports with varying success. The next step is to treat these ligand covered Ni NPs to remove the ligands, which can prevent access to the Ni nanoparticle surface by reactants. This can be done by calcination and subsequent reduction at elevated temperatures. To this end, TGA-MS measurements were performed to determine suitable heat treatments parameters. Results of this experiment are shown in Figure 4.8, with Figures 4.8a and 4.8b showing the TGA profile and the MS signal for CO_2, respectively. A corresponding signal for H_2O is shown in Figure A.23. Major mass loss is observed from 200 °C to 800 °C, with most mass loss occurring from 200 °C to 500 °C. Initial mass loss could be explained through the evaporation of water, and this corresponded well to the observed peak in Figure A.23. The largest relative mass loss appeared to take place at around 340 °C, which corresponded well to the peak found in the MS signal of CO_2. This is rationalised as the burning of the ligand material still present on the surface of the Ni nanoparticles, and any residual organic materials still present on the support material itself. Interestingly, the peak position of the MS signal for CO_2 is very close to the literature value for the boiling point of OAm, which is around 348-350 °C (Sigma Aldrich, 70 %). This supports the hypothesis that we are indeed burning ligand materials at these temperatures. Based on this data, and taking into account the stability of GNP500 (TGA data is shown in Figure A.25), further calcination treatments of supported Ni nanoparticles were performed at 250 °C. This was done as some CO_2 MS signal is observed for our Ni/SiO_2, but the GNP500 does not yet degrade at this temperature (Figure A.25).

The next part of the heat treatments involves the subsequent reduction of our now nickel oxides to metallic nickel. To this end, suitable reduction treatments need to be established, again taking into account the stability of our support materials as well as our Ni nanoparticles. A temperature-programmed reduction experiment were performed on the calcined sample (250 °C, 20 vol-% O_2 in N_2) discussed in Figure 4.8. The results are shown in Figure 4.9. A maximum in H_2 consumption is observed at 320 °C, which corresponds to the reduction of NiO to metallic Ni. To make sure all NiO is reduced, further reduction experiments in H_2 were done at 350 °C. Here, the stability of GNP500 was again taken into account [53], with which it was determined that higher temperatures are unsuitable for this support material.

To check whether these initial experiments were indeed successful in removing all ligands and other residual organic materials from the Ni nanoparticles, additional TGA-MS in O_2 and IR spectroscopy were performed for the same $Ni(4.1)/SiO_2$ after various heat treatments. TGA-MS results are shown in Figure 4.10. Mass

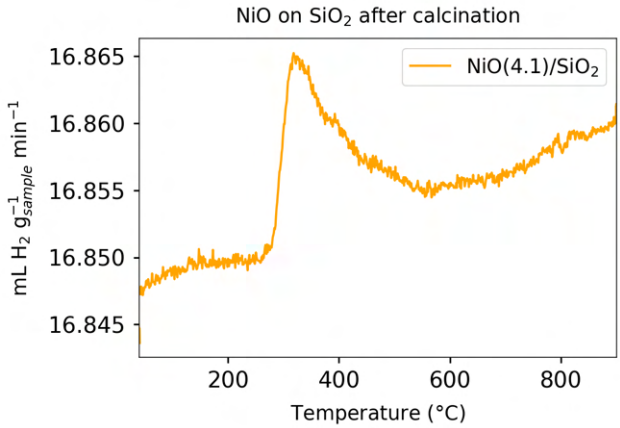

Figure 4.9: TPR data acquired for the sample discussed in Figure 4.8 after calcination at 250 °C in 20 vol-% O_2 in N_2. A maximum in H_2 consumption is observed at 320 °C, which corresponds to the reduction of NiO to metallic Ni.

loss was observed for most samples from 200 °up to 800 °C. Mass spectrometry indicated that weight loss was caused by loss of water(Figure A.24). In addition, a peak for CO_2 was found for some samples from 200 °C ending at 500 °C, as shown in Figure 4.10b. This can be rationalised as the burning of the carbon containing ligands, OAc and OAm. The largest relative mass loss was observed for the catalyst directly after deposition, as well as the catalyst which was calcined at 250 °C (the light blue and red lines, respectively). In three cases, a peak for CO_2 was observed. This was seen in the untreated sample, in the sample which was calcined at 250 °C in O_2 and the sample which was reduced at 350 °C in H_2 (the light blue, red and purple lines). The treatment in H_2 at 350 °C appears to have had the greatest effect on removing residual organics, but the presence of this CO_2 peak after treatment indicates that there still some organics present on the catalyst, which could be ligands still attached to the Ni NPs. No peak corresponding to CO_2 was observed in the mass spectrometry data after either calcination at 250 °C and subsequent reduction at 350 °C, nor after calcination at 500 °C (the brown and green lines). This indicates that these heat treatments are sufficient to remove most of the residual organic material and ligands present on the catalysts. The position of the peak of the CO_2 MS signal for the precatalyst and the sample calcined at 250 °C is 350-360 °C, which corresponds to the boiling point of OAm. No CO_2 peak is observed for the Davisil 643, which supports the conclusion that these CO_2 correspond to the burning of residual organic material and ligands present on the Ni NP surface. Therefore, we can conclude the combined treatment of calcination in 20 vol-% O_2 at 250 °C and reduction in 5 vol-% H_2 at 350 °C is sufficient to remove any organics still present after deposition.

To check whether the developed methods could be applied to the carbon GNP500 support, TGA measurements were also performed for Ni NPs supported on carbon, as shown in Figures 4.11a and 4.11b. This, in addition to the TGA profile for pristine GNP500 shown in the GNP500 information sheet [53], indicates that calcination at temperatures higher than 200 °C, will inevitably start to degrade the carbon support. Therefore, to keep the GNP500 as intact as possible, calcination was performed at 250 °C, as previously mentioned. Using MS data to determine whether ligands are removed was difficult, as during treatment in O_2 the carbon support would inevitably burn and form CO_2 as well, overshadowing the relatively small contribution of the ligands to this signal. However, the fact that the carbon support itself was burned away at high temperatures (shown in the TGA-MS data in Figures 4.11a and 4.11b) was used to determine the weight loading of Ni for these samples. The relevant equation is shown in Equation (2.2). This was achieved by heating the sample during the measurement to 800 °C in 20 vol% O_2 and then keeping it at this temperature for 2 hours. All carbonaceous material should be burned off and the only weight remaining should be that of NiO. This could then be related to the amount of Ni and subsequently to the amount of starting material in the TGA, yielding a weight percentage of Ni. Results of the TGA data presented in Figures 4.11a and 4.11b are summarized in Table 4.1. The sample GNP500 has 0.33 wt-% remaining after the TGA program had finished. This wt-% in all probability is ash remaining after burning the carbon support material. The Ni wt-% of carbon supported Ni samples mentioned further in this thesis are all determined using this method. Another interesting observation

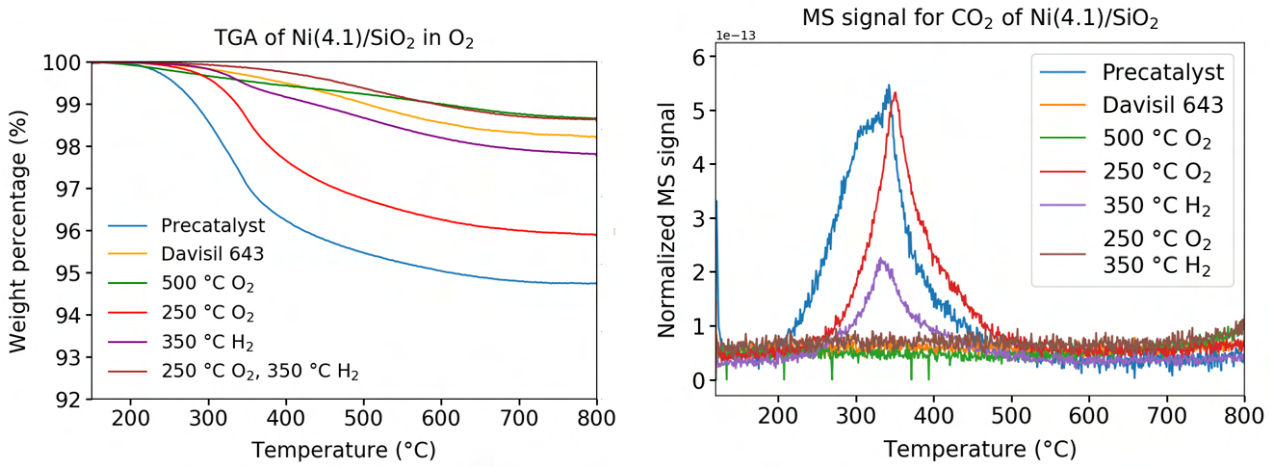

(a) (b)

Figure 4.10: TGA-MS data acquired for $Ni(4.1)/SiO_2$ in O_2 directly after deposition and after various heat treatments. a) TGA profile of the tested samples. Major mass loss is observed for the precatalyst from 200 °C up to 500 °C. b) Normalized MS signal (mg^{-1}_{sample}) for CO_2 of the tested samples.

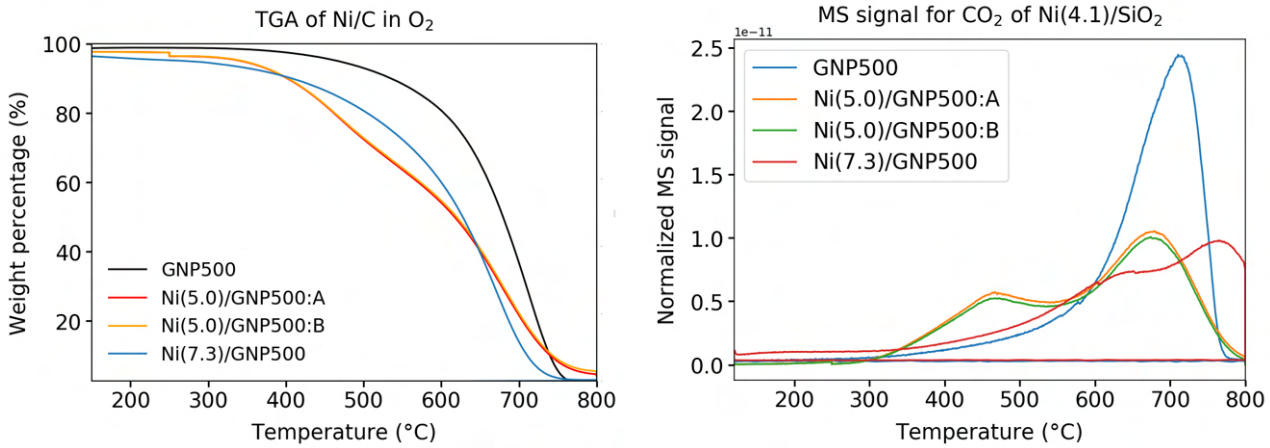

(a) (b)

Figure 4.11: TGA-MS data acquired for $Ni(4.1)/SiO_2$ in O_2 directly after deposition and after various heat treatments. a) TGA profile of the tested samples. Major mass loss is observed for the precatalyst from 200 °C up to 500 °C. b) Normalized MS signal ($mg^{-1}{}_{sample}$) for CO_2 of the tested samples.

were the double peaks observed for the MS signal for CO_2 of the Ni/C samples shown in Figure 4.11b. These double peaks were both located at lower temperatures than the peak observed for GNP500, which is located at 700 °C. This is likely a result of the NiO acting as an oxidation catalyst and lowering the temperature necessary to start burning the carbon support.

Another set of experiments was performed to determine the effects of the heat treatments on ligand removal. In this case, infrared spectroscopy experiments were performed to identify the presence of characteristic peaks for carbon containing materials, such as peaks corresponding to the C-H stretching vibrations. The absence or presence of these peaks indicated the lack or presence of carbon containing materials, and thus whether ligands were present. Shown in Figures 4.12a and 4.12b are results of these infrared spectroscopy experiments. These spectra are normalized with respect to the largest peak, present at 1100 cm^{-1} which corresponds to the Davisil 643 SiO_2 support. The peak at 600 cm^{-1} also corresponds to SiO_2. An IR spectrum of untreated

Table 4.1: Overview of Ni wt-% as determined by TGA. Ni wt-% for GNP500 indicates the % of remaining carbon.

Sample	Ni wt-%
GNP500	0.33
Ni(5.0)/GNP500A	2.7
Ni(5.0)/GNP500B	2.7
Ni(7.3)/GNP500	1.2

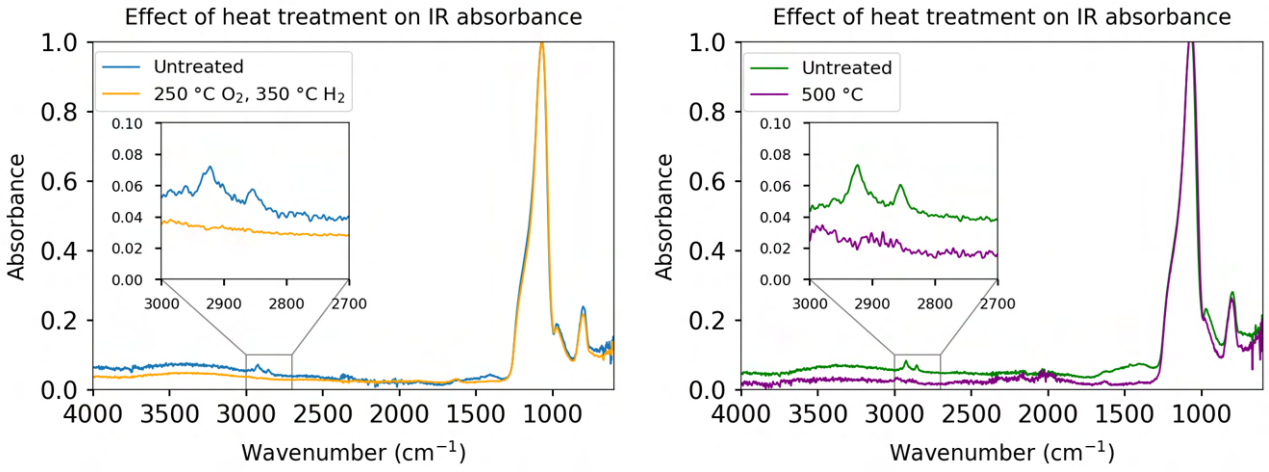

(a) (b)

Figure 4.12: IR spectroscopy of Ni(7.7)/SiO_2 with a Ni wt-% of 2.55 % of a) an untreated sample and the same sample treated in O_2 at 250 °C and in H_2 at 350 °C and b) an untreated sample and a Ni(6.3)/SiO_2 with a Ni wt-% of 1.25 % treated in O_2 at 500 °C. The disappearance of the C-H stretch vibrations between 3000 and 2800 cm^{-1} after these treatments indicates successful removal of carbonaceous materials. The large peaks at 1100 cm^{-1} and 600 cm^{-1} corresponds to the support material.

Davisil 643 (SiO_2) is shown in Figure A.14. In Figure 4.12a, the spectrum of an untreated Ni(7.7)/SiO_2 sample as well as the same sample treated in O_2 at 250 °C and in H_2 at 350 °C are shown. The peaks at 2950 cm^{-1} and 2850 cm^{-1} present in the untreated sample correspond to C-H stretch vibrations, which can be attributed to the presence of residual organic material, such as ligands. Their disappearance in the treated sample indicates successful removal of these ligands to a certain degree. A similar result is observed for a Ni(6.3)/SiO_2 sample (shown in Figure 4.12b) where it was treated at 500 °C in 20 vol-% O_2 in N_2. This experiment was performed as literature calcination treatments are sometimes performed at high temperatures [3]. Here, the peaks corresponding to the C-H stretch vibrations also disappear. This corroborates well with the TGA-MS data presented in Figures 4.10a and 4.10b, where we also notice the disappearance of a carbon indicating peak after utilising either treatment. It should be noted that not in all cases the peaks at 2950 cm^{-1} and 2850 cm^{-1} could be observed for untreated samples using ATR-IR . This indicates that in some cases, the carbon content was too small to observe, even when ligands might still be present.

The reduction treatments discussed in this thesis were determined by temperature-programmed reduction for which calcined samples were used. The results for Ni/SiO_2 are shown in Figure 4.13. In Figure 4.13a, the result of TPR is shown for two distinct sizes of Ni NPs supported on SiO_2. For the smaller particles, a reduction peak at 300 °C is observed, whilst for the larger particles, one is observed at 230 °C. The peak at lower temperature for the larger particles indicates that these particles are easier to reduce, which could point towards a weaker interaction with the support material when compared to the smaller particles. The same effect is observed after reduction as well, for the passivated samples. Here the larger particles reduce at 160 °C and the smaller particles at 230 °C. Additionally, the broad peak observed for both particle sizes might indicate the particles have a larger size distribution. However, this would need to be tested by synthesizing a

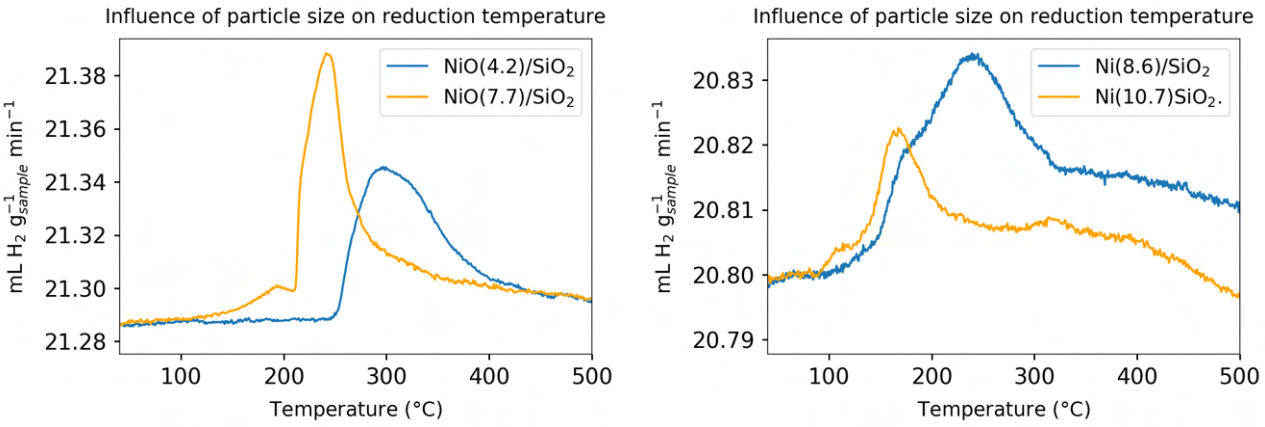

(a) (b)

Figure 4.13: TPR profiles of Ni(7.7)/SiO_2 with at Ni wt-% of 2.55 as determined by ICP-OES for a) the samples after calcination at 250 °C in 20 vol-% O_2 in N_2 and b) after calcination at 250 °C in 20 vol-% O_2 in N_2 and reduction at 350 °C in 5 vol-% H_2 in N_2.

broader size range of Ni/SiO_2 catalysts.

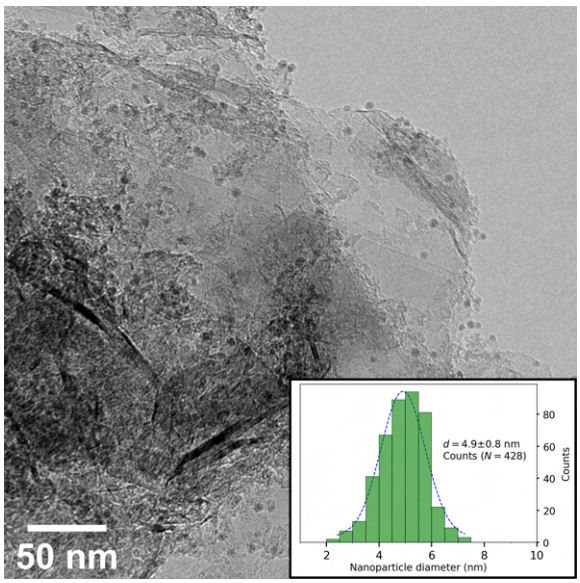

(a) Ni(4.9 ± 0.8)/C

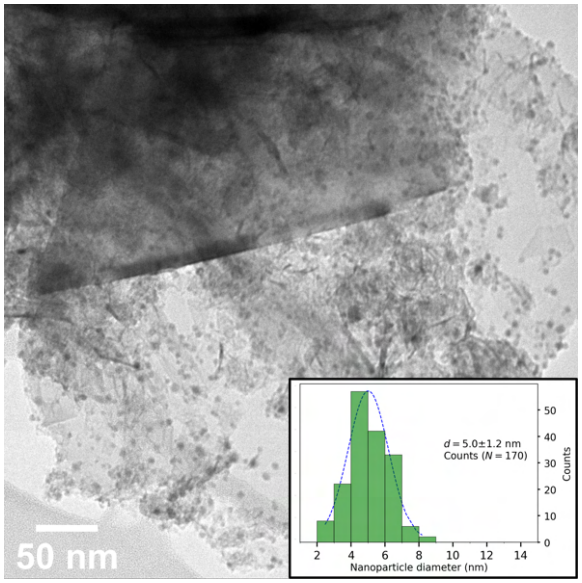

(b) Ni(5.0 ± 1.2)/C

Figure 4.14: TEM images of 4 nm Ni seeds supported on GNP500 with a wt-% of 2.7 % for a) an untreated sample with a Ni particle diameter of 4.9 ± 0.8 nm and b) a sample after heat treatment at 250 °C in O_2 and at 350 °C in H_2 with a Ni particle diameter of 5.0 ± 1.2 nm. Ni wt-% was determined according to Equation (2.2). Corresponding TGA profile is shown in Figure A.17.

4.1.3 Influence of heat treatments on Ni nanoparticles stability

The significant advantage that colloidal synthesis can have over conventional impregnation is the fact that particles can remain as they were in solution, given mild deposition strategies are used. However, heat treatments like those established in Section 4.1.2 can have great influence on both the support as well as the Ni NPs themselves. Shown in Figure 4.14 are TEM images of Ni NP seeds supported on GNP500 before and after treatment at 250 °C in O_2 and at 350 °C in H_2. Well-dispersed particles can be found before as well as after heat treatments. No large agglomerates of Ni seeds are observed across the support, and no particle growth is observed for this sample. These particles, with a size of 4.9 ± 0.8 nm after deposition and a mean size of 5.0 ± 1.2 nm after calcination at 250 °C in O_2 for 2 h and reduction at 350 °C in H_2 for 2 h, appear to be mostly unchanged as a result of the heat treatments. X-ray diffraction corroborates these results, as shown in Figure 4.15. Here, the reflections shown all correspond to the ordered structure of the GNP500. No reflections corresponding to large Ni or NiO crystallites are observed, confirming the TEM images shown in Figure 4.14.

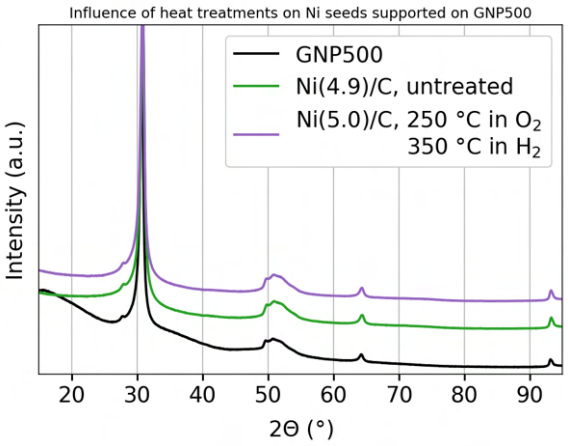

Figure 4.15: X-ray diffraction pattern of 4 nm Ni seeds on GNP500 during various stages of catalyst preparation. Reflections at 2Θ values of 31˚, 50-52˚, 64-65˚and 93˚correspond to the carbon support GNP500, which is shown in black in the figure. No reflections corresponding to metallic Ni or NiO are observed, indicating the absence of very large crystallites.

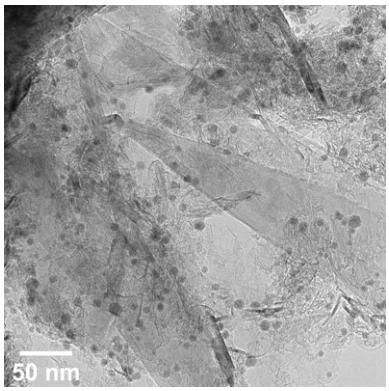

(a) Ni(8.0 ± 1.7)/C

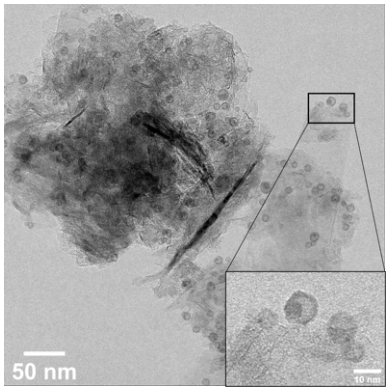

(b) Ni(9.5 ± 1.5)/C

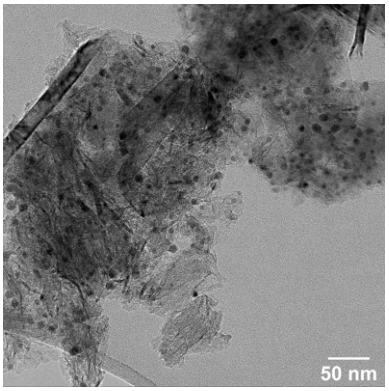

(c) Ni(7.3 ± 1.7)/C

Figure 4.16: TEM images of larger 7 nm Ni NPs supported on GNP500 with a Ni wt-% of 2.7 % for a) an untreated sample and b) a sample after heat treatment at 250 ˚C in O_2 and c) at 350 ˚C in H_2. A small size increase and subsequent contraction can be seen moving from Figures 4.16a to 4.16c. Hollow NPs can be seen in Figure 4.16b, which are shown in greater detail in the inset. Corresponding size distributions are found in Figure A.28, with a) corresponding to Figure A.28a, b) corresponding to Figure A.28b and c) corresponding to Figure A.28c. Ni wt-% was determined according to Equation (2.2) and a corresponding TGA profile is shown in Figure A.18.

Shown in Figure 4.16 are TEM images of 7 nm Ni NPs deposited on GNP500. Initially (Figure 4.16a), the Ni NP mean size was 8.0 ± 1.7 nm. After calcination at 250 ˚C in O_2 (Figure 4.16b), the average size was 9.5 ± 1.5 nm. After reduction, the mean size was 7.3 ± 1.7 nm(Figure 4.16c). Interestingly, after calcination, the particles appear hollow, with darker, smaller particles attached to the inside of a hollow sphere, which is shown in the inset of Figure 4.16b. This hollow particle appears slightly larger than the initial particles were. Reducing the particles again results again in solid particles, slightly smaller than the hollow particles observed. The hollow sphere might consist of NiO or Ni. This phenomenon, called the Kirkendall effect, is also found for Ni NPs supported on Al_2O_3 [60], or unsupported Ni NPs as found by Nakamura et al [82]. This is discussed in more detail in Chapter 5.

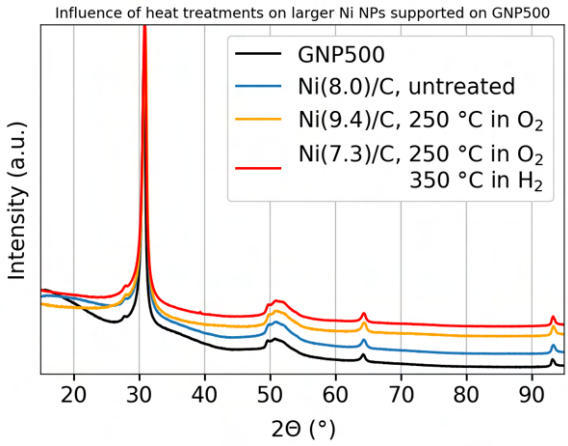

Figure 4.17: X-ray diffraction pattern of larger 7 nm Ni NPs on GNP500 during various stages of catalyst preparation. Reflections at 2Θ values of 31˚, 50-52˚, 64-65˚and 93˚correspond to the carbon support GNP500, which is shown in black in the figure. No reflections corresponding to metallic Ni or NiO are observed, indicating the absence of very large crystallites.

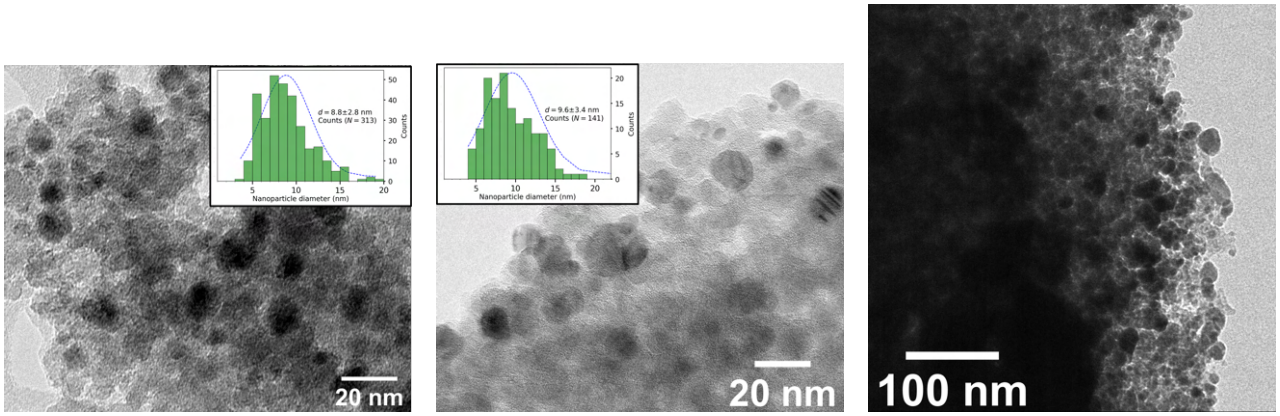

(a) Ni(8.8 ± 2.8)/SiO_2 (b) Ni(9.6 ± 3.4)/SiO_2 (c) Ni/SiO_2

Figure 4.18: TEM images of larger 7 nm Ni/SiO_2 a) after deposition for a sample with a Ni wt-% of 0.7 %, b) after calcination at 250 ˚C in O_2 for 2 h for a sample with a Ni wt-% of 0.7 %. Ni wt-% was determined with TPR according to Equation (2.1). Corresponding TPR profile is shown in Figure A.20. c) After calcination at 250 ˚C in O_2 for 2 h for a sample with a Ni wt-% of 2.55 % as determined by ICP-OES.

TEM images of 4 nm Ni seeds and larger 7 nm Ni NPs on SiO_2 are shown in Figures 4.18 and 4.20, with corresponding X-ray diffraction patterns shown in Figures 4.19 and 4.21. Shown in Figure 4.18a is a typical TEM image of larger Ni NPs supported on SiO_2 with an average size of 8.8 ± 2.8 nm, directly after deposition. These larger Ni NPs appear to grow during preparation steps, yielding an average size of 9.6 ± 3.4 nm (Figure 4.18b) after calcination and reduction. In cases of a sample with higher Ni wt-%, shown in Figure 4.18c, much larger particles were obtained after calcination and reduction. An average particle diameter was not determined based on TEM images as very large and inhomogeneous particle diameters and shapes were found. These results are corroborated by XRD shown in Figure 4.19, where a significant reflection is obtained for Ni(200) and Ni(220) at 52˚and 61˚, respectively. These reflections indicate the presence of larger crystallites, also observed with TEM.

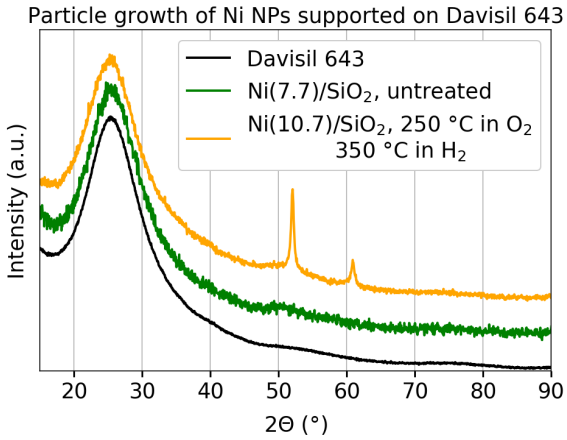

Figure 4.19: X-ray diffraction pattern of larger 7 nm Ni NPs on SiO_2 during various stages of catalysts development. Broad reflections centered at 25˚correspond to the reflections from amorphous silica, which is shown in the black line. The reflections at 52˚and 61˚correspond to Ni(200) and Ni(220), respectively, and indicate the presence of larger crystallites.

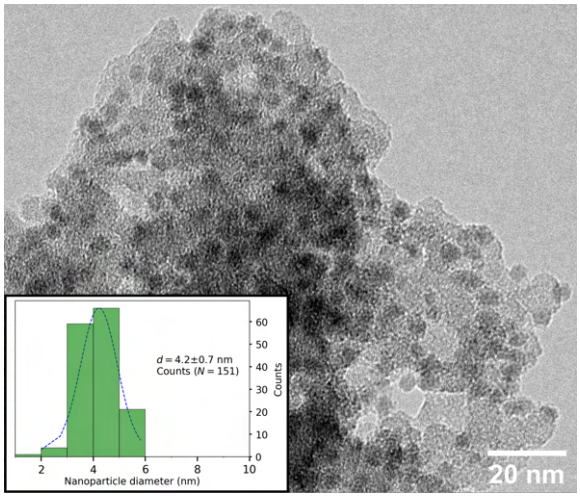

(a) Ni(4.2 ± 0.7)/SiO_2

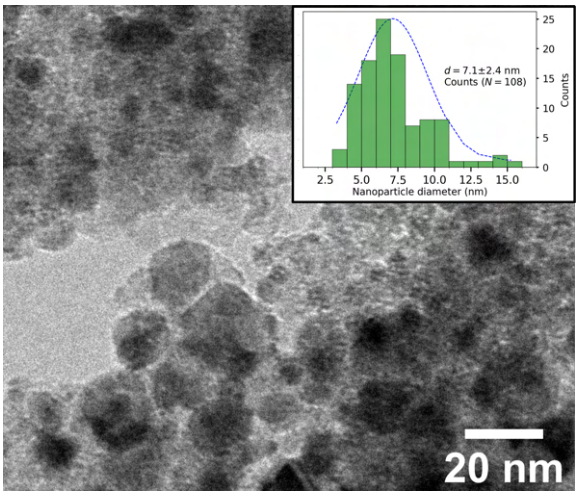

(b) Ni(7.1 ± 2.4)/SiO_2

Figure 4.20: TEM images of Ni seeds supported on SiO_2 with a) Ni NPs supported on SiO_2 directly after deposition and b) after calcination at 250 ˚C for 2 h and reduction at 350 ˚C for 2 h. Ni wt-% is 1.51 %, as determined by ICP-OES.

The influence of calcination at 250 ˚C for 2 hours and subsequent reduction at 350 ˚C for 2 hours was also investigated for 4 nm Ni seeds on SiO_2. TEM images are shown in Figure 4.20. Similar to the larger 7 nm particles, some particle sintering is observed. Average particle diameter increases from 4.2 ± 0.7 nm to 7.1 ± 2.4 nm. XRD reveals a small reflection observed at 52˚, which indicated the presence of larger crystallites, as shown in Figure 4.21.

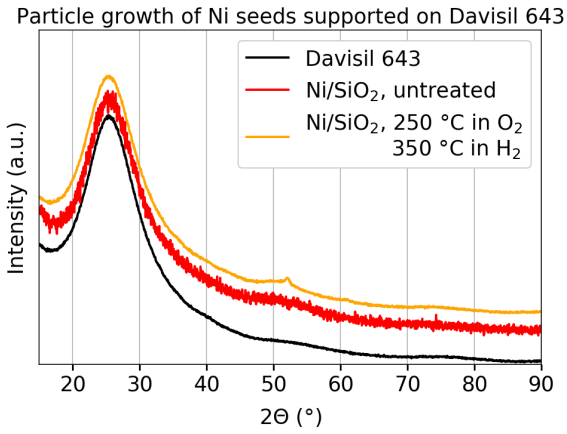

Figure 4.21: X-ray diffraction pattern of 4 nm Ni seeds on SiO_2 during various stages of catalysts development. Broad reflections centered at 25˚correspond to the reflections from amorphous silica, which is shown in the black line. The reflection at 52˚corresponds to Ni(200), and indicates the presence of larger crystallites.

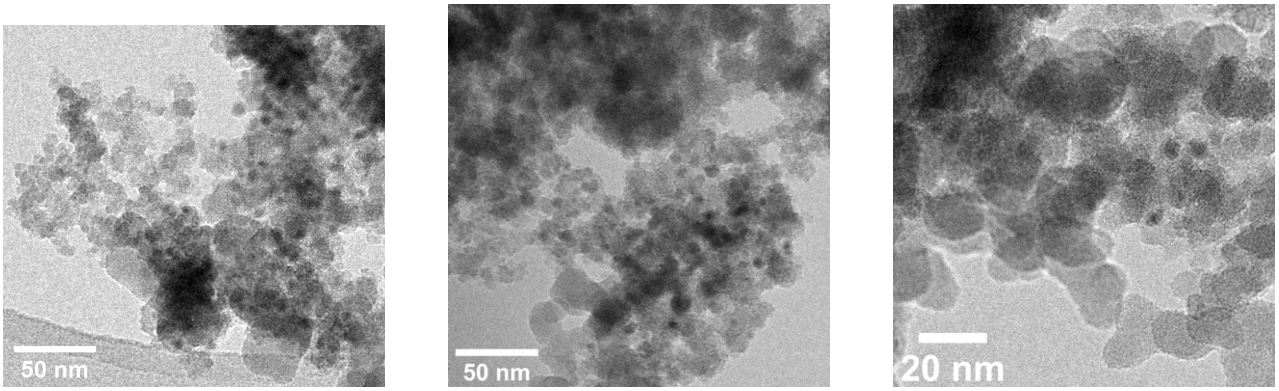

(a) (b) (c)

Figure 4.22: TEM images of Aerosil 380V supported larger 7 nm Ni NPs a) before calcination and reduction, b) larger 7 nm Ni NPs after calcination at 250 ˚C in O_2 for 2 h and reduction at 350 ˚C in H_2 for 2 h. and c) Ni 4 nm seeds after calcination at 250 ˚C in O_2 for 2 h and reduction at 350 ˚C in H_2 for 2 h.

Figure 4.22 shows TEM images of the effect that the established heat treatments can have on the stability of the 4 nm Ni seeds supported on Aerosil 380V (SiO_2, 380 m^2/g, Figure 4.22c) and larger 7 nm Ni nanoparticles supported on Aerosil 380V (Figure 4.22b). Figure 4.22a showed the larger Ni nanoparticles directly after deposition. A corresponding X-ray diffractogram for both reduced samples is shown in Figure 4.23. For both samples, only a very small amount of particles could be found. Most of these particles appeared similar to the particles directly after deposition, indicating limited particle growth and reshaping. XRD does not detect the presence of large crystallites, corroborating the TEM results.

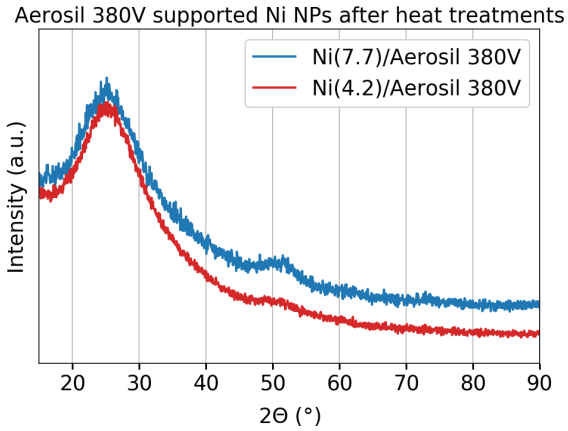

Figure 4.23: XRD of Aerosil 380V supported 4 and 7 nm Ni NPs after calcination and reduction. A small shoulder near 52°is observed, which can correspond to crystalline Ni(200) domains.

Shown in Figures 4.24 and 4.25 are TEM images of Al_2O_3 supported Ni seeds. Figure 4.24 shows a TEM image of the sample directly after deposition. The sample calcined at 250 °C in Figure 4.25 shows no significant difference from the one shown in Figure 4.24. The high concentration of Ni NPs observed makes particle growth during reduction a very likely possibility, which is observed in Figure 4.27. Here, the red line shows two reflections corresponding to metallic nickel at 52°for Ni(200) and 61°for Ni(220). These intense reflections indicate the presence of large crystallites, with an average crystallite size of 26 nm as evaluated by the Scherrer equation. Shown in Figure 4.26 is the result of applying the developed heat treatments on a sample synthesized with TOP. This sample Ni(7.0)/SiO_2 showed a very similar size and size distribution to the initial sample (7.4 ± 1.0 nm) and was virtually unchanged as a result of the applied thermal treatments. ICP-OES and EDX both confirmed the presence of Ni and P, with ICP-OES revealing a Ni wt-% of 0.75 and a P wt-% of 0.25 % even after treatment. This indicates that the ligand removal method was unsuccessful for this particular catalyst and that phosphorous was still present, similar to the result found in literature [69].

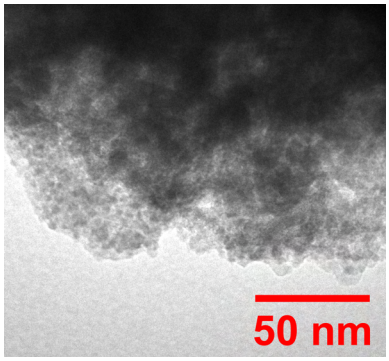

Figure 4.24: TEM image of Ni(3.7 ± 0.8)/Al_2O_3 directly after deposition

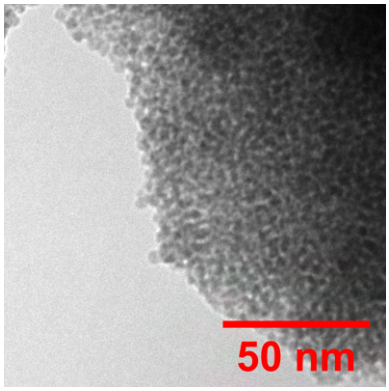

Figure 4.25: TEM image of Ni(3.9 ± 0.6)/Al_2O_3 directly after calcination at 250 ˚C in O_2 for 2 h. Particles appear to have a similar particle size to those shown in Figure 4.24.

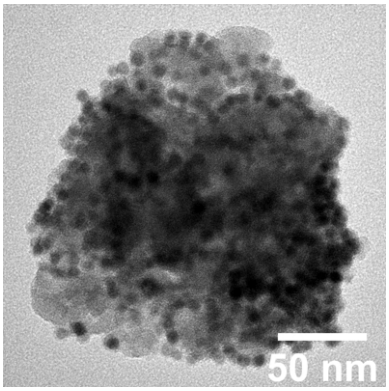

Figure 4.26: Ni(7.0)/SiO_2 synthesized using TOP as a ligand material after calcination at 500 ˚C in O_2 for 2 h and reduction at 350 ˚in H_2 for 2 h. Corresponding size distribution is found in Figure A.26. EDX confirmed the presence of phosphorous after these treatments, indicating unsuccessful removal of the ligands or possible incorporation of P in the Ni lattice. ICP-OES confirmed this and gave a Ni wt-% of 0.75 and a P wt-% of 0.25 %.

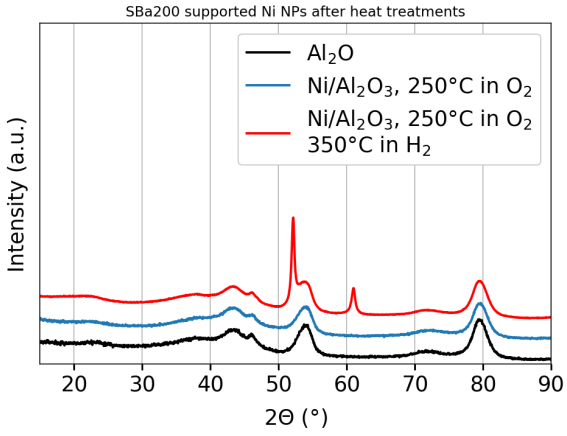

Figure 4.27: XRD of Al_2O_3 supported Ni seeds during various stages of catalyst development. No reflections corresponding to Ni or NiO are observed for the sample after calcination. After reduction, strong reflections at 52˚and 61˚corresponding Ni(200) and Ni(220) are observed. This indicates the presence of large crystallites in the sample after reduction.

4.2 Conclusions

In this chapter, the deposition of colloidal Ni NPs on various supports, GNP500 (C), Davisil 643 (SiO_2), Aerosil 380V (SiO_2) and SBa200 (Al_2O_3) is described. In addition, investigation into the removal of ligands is also discussed. After some experimentation, a method was developed to reliably deposit colloidal Ni NPs on different supports. Various Ni wt-% could be obtained through this deposition method. Size and shape were maintained over the different supports, however the distribution of the Ni nanoparticles over the support materials was not completely homogeneous. It was observed for GNP500, some regions remain devoid of Ni NPs, whilst other regions contained many Ni NPs. In the case of Aerosil 380V, only a very limited amount of particles was observed, indicating unsuccessful deposition. These particles were also not well dispersed across the support. Deposition of the TOP-capped Ni NPs led to inhomogeneously deposited NPs, on both GNP500 and Davisil 643. In addition, even after exposing the TOP-capped Ni nanoparticles supported on silica to the established heat treatments, phosphorous is still detected in significant amounts using EDX and ICP-OES. This indicates either the presence of ligands materials or the formation of a Ni_xP_y phase. Together, these two results for the TOP samples highlight the importance of the developed method for phosphorous-free colloidal synthesis.

Using TGA and TPR, heat treatments were determined that succeeded in removing the ligands from the Ni NPs and in reducing the Ni NPs. However, these treatments caused significant sintering for the Davisil 643 supported Ni NPs with higher Ni wt-%, as well as for nanoparticles supported on SBa200. Particles on GNP500 showed more limited growth and those supported on Aerosil 380V showed limited growth as well. It appeared that primarily wt-% and support surface area influence the sintering effects observed in this chapter. This could be caused by the smaller interparticle distance that was the result of higher Ni wt-% sample or lower support surface area where the particles can deposit. This hypothesis is corroborated by the Ni/C sample shown in Figure A.27, where Ni nanoparticles were initially inhomogeneously distributed across the support and for which sintering and irregular shapes were observed after reduction. Due to the inhomogeneous distribution, the interparticle distance was smaller and this could cause more significant sintering. This sintering also led to the observation that despite starting from different colloidal particle sizes, sizes of Ni nanoparticles after heat treatments were much closer, making studies towards size effects difficult.

The larger Ni NPs supported on carbon showed interesting oxidation and reduction behaviour in the form of the Kirkendall effect. The particles hollowed out during oxidation, and became dense after reduction. This phenomenon is discussed in more detail in Chapter 5.

4.3 Outlook

The method for Ni nanoparticle deposition is not yet completely optimized. In particular, the distribution of the nanoparticles across a high surface area support like GNP500 needs to be improved, as some regions of the support remain completely empty. A promising approach might be to use 99% toluene instead of 90%, as the presence of water might prevent migration of colloids to certain parts of the support surface already occupied by physisorbed water. Additionally, functionalization of the oxidic supports with hydrophobic ligands might improve interaction of these supports with the colloidal particles, improving their dispersion. Finally, sonication of the suspension of colloids and support material for longer times might give the colloids more time to migrate across the support surface.
The methods demonstrated in this thesis for Ni NP synthesis and deposition could easily be adapted for different support. Especially other oxidic supports, like TiO_2, CeO_2 and ZrO_2 could be interesting to investigate for the potential elucidation of support effects when using the same 4 nm Ni seeds.
Heat treatments used in this thesis causes significant sintering of Ni NPs, especially on Davisil 643 (SiO_2) and SBa200 (Al_2O_3). Milder methods to remove ligands and organic material such as chemical removal might be interesting to possibly obtain more monodisperse ligand free nanoparticles. In addition, samples with lower Ni wt-% appeared to grow less during treatments, indicating that these depositions and heat treatments might also be performed on low < 1 % samples to reduce particle growth.

Chapter 5

Investigating morphology of nickel nanoparticles during heat treatments with *in situ* electron microscopy

This chapter discusses an interesting observation which was already depicted in Section 4.1.3. Here, the hollowing out of Ni nanoparticles supported on carbon was observed after calcination. After reduction, these hollow particles reverted back to solid Ni nanoparticles. This type of hollow particle showcases the result of a specific type of diffusion effect. This effect, known as the nanoscale Kirkendall effect, is also observed in literature for Ni nanoparticles supported on Al_2O_3 as found by Zacharaki et al[60], or unsupported Ni NPs as found by Nakamura et al and Railsback et al[82,83]. The nanoscale Kirkendall effect is a result of diffusion differences at the boundary between two regions in a nanoparticle[83]. A schematic depiction is shown in Figure 5.1. Here, J_{Ni} represents the outwards diffusion rate of Ni[83]. J_O and J_V represent the inwards diffusion of oxygen and vacancies. Basically, the exposure of a nanoparticle to oxygen (or other elements, like sulphur or phosphorous) at elevated temperatures can lead to a diffusion inhomogeneity. In the depicted case, the inwards diffusion rate of anions (J_O) is lower than the outwards diffusion rate of Ni (J_{Ni})[83]. This can lead to the formation of vacancies in the center of the particle, potentially resulting in the formation of large voids[83]. Typically, the hollow NiO nanoparticles that form are larger than their initial Ni counterparts[84]. The reverse of the reaction, where the hollow NiO nanoparticle collapses and shrinks again is also possible[82,84]. Investigating this effect using *in situ* transmission electron microscopy might provide insight in how Ni nanoparticle morphology changes as a result of oxidative and reductive treatment. This chapter aims to answer the following research question:

- Can we use *in situ* transmission electron microscopy to investigate the oxidation and reduction behaviour of carbon supported Ni nanoparticles?

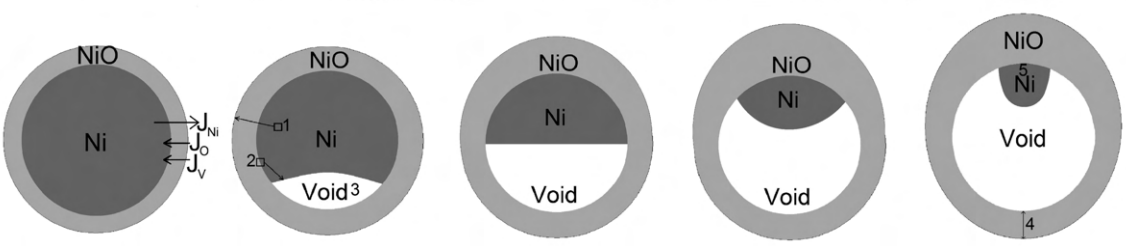

Figure 5.1: A schematic depiction of the nanoscale Kirkendall effect for a NiO/Ni nanoparticle. J_{Ni} represents the outwards diffusion rate of Ni. J_O and J_V represent the inwards diffusion of oxygen and vacancies. Vacancies are formed as a result of a difference in outwards and inwards diffusion of Ni and O respectively. Reproduced from Railsback et al[83].

5.1 Experimental methods

In situ transmission electron microscopy experiments were performed on a FEI Talos^{TM} F200X set at 200 kV using a *in situ* gas phase sample holder from Protochips. All experiments were performed on the same sample, Ni/C with a Ni wt-% of 2.7 % and a initial particle size of 8.0 ± 1.7 nm.

5.1.1 Oxidation in oxygen followed by reduction in hydrogen

First, the sample was heated to 200 °C with 1 °C/s under an argon (Ar) flow of 0.1-0.2 standard cubic centimeters per minute (sccm) for 30 minutes. After drying in Ar, the sample was cooled down to 50 °C. After drying in Ar, the sample was cooled down to 50 °C and the flow was switched to 20 vol-% O_2 in Ar. The sample cell was flushed with this gas for some time to ensure O_2 in Ar atmosphere. The sample is then heated to 250 °C at a rate of 0.1 °C/s and an image was taken with the transmission electron microscope every five minutes. The beam was blanked in between measurements. Images were sampled for 2 seconds. After measuring in O_2 for 50 minutes, the sample was cooled down to 50 °C. The sample holder was then flushed at 25 °C with Ar after which it was brought under vacuum. The sample was then imaged in vacuum. The experiment was continued and a 5 vol-% H_2 in Ar with a flow rate of 0.2 sccm was used to flow over the sample. The sample was then heated to 350 °C with 0.1 °C/s. It was kept at this temperature for 25 minutes then heated to 400 °C with 0.1 °C/s. It was kept at this temperature for 20 minutes and finally it was heated to 450 °C with 0.1 °C/s at which it was kept for 10 min, after which it was allowed to cool down again to 25 °C. Images were taken with the electron microscope every 5 minutes and the electron beam was blanked in between measurements.

5.1.2 Reduction in hydrogen

First, the sample was heated to 300 °C with 1 °C/s under an argon (Ar) flow of 0.1-0.2 standard cubic centimeters per minute (sccm) for 30 minutes. After drying in Ar, the sample was cooled down to 100 °C and the flow was switched to 5 vol-% H_2 in Ar. The sample cell was flushed with this gas for some time to ensure H_2 in Ar atmosphere. The sample is then heated to 350 °C at a rate of 0.1 °C/s at which it was kept for 2 hours and an image was taken with the transmission electron microscope every five minutes. The beam was blanked in between measurements. Images were sampled for 1 second.

5.2 Results & Discussion

In this section, the results of the *in situ* TEM experiments are described. For direct comparison, the *ex situ* TEM experiments of the Ni/C catalysts with a Ni wt-% of 2.7 % are shown in Figure 5.2, with Figures 5.2a to 5.2c showing the untreated, calcined and reduced catalyst, respectively. Shown in Figure 5.3 is the result of the *in situ* TEM experiment performed according to Section 5.1.1, where the oxidation behaviour of the Ni nanoparticles was observed. Starting from Figure 5.3a and ending at Figure 5.3d, the hollowing out of these Ni nanoparticles was observed. This hollowing out appeared to start near the edge of the particle, then quickly expanding over time. All particles appeared to hollow out at the same time. In some cases, a small black amorphous spot on the inside of the particle could be observed, which was likely a spot of Ni adhered to the inner part of the NiO shell. The experiment was then continued to study the back reaction where the hollow NiO nanoparticles shrink back into Ni nanoparticles. However, after cooling down and bringing the sample under vacuum, the carbon support material had deteriorated significantly. Shown in Figure A.29 is the result of taking a TEM image of the carbon supported Ni nanoparticles in vacuum. A possible explanation of this observation could be the interaction of the high energy electron beam with adsorbed water on the support, destroying the support material in the process. This adsorbed water might be present due to a small leak in the sample holder cell which. The measurement was continued, but particles appeared to never fully reduce back to Ni nanoparticles. Instead, separate dark spots were visible on the inside of the particles, which could combine to form a single large dark spot. This is shown in Figure A.30. Repeating this experiment whilst preventing the deterioration of the support in between the oxidation and reduction atmospheres would possibly allow for a full observation of the nanoscale Kirkendall effect with *in situ* TEM. A separate *in situ* TEM experiment was performed at a temperature of 350 °C with a temperature ramp of 0.1 °C/s. The result of this experiment are shown in Figure 5.4. Some of the hollow NiO nanoparticles visible in Figure 5.4a appeared to reduce back

to solid Ni, but not all particles would do so. This was in contrast to the reduced sample shown in Figure 5.2c, where only solid particles were visible after reduction at 350 °C in H_2 for 2 hours.

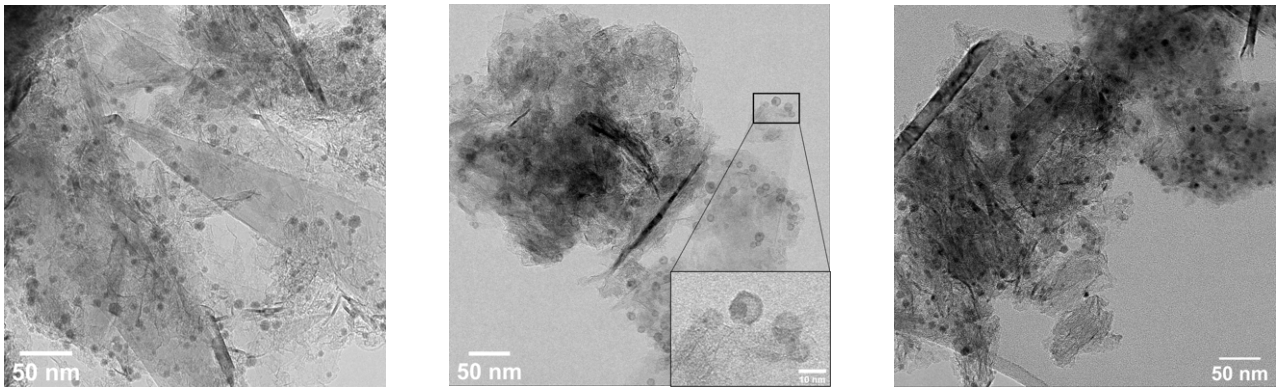

(a) Ni(8.0 ± 1.7)/GNP500 (b) Ni(9.5 ± 1.5)/GNP500 (c) Ni(7.3)/GNP500

Figure 5.2: Ex situ TEM images of larger Ni NPs supported on GNP500 with a Ni wt-% of 2.7 %. All depicted images are made of the same sample after different treatments with a) the untreated sample with an average size of 8.0 ± 1.7 nm, b) the sample after heat treatment at 250 °C in O_2 with and average size of 9.4 ± 1.4 nm and c) the sample after subsequent heat treatment at 350 °C in H_2 with an average 7.3 ± 1.7 nm. A small size increase and subsequent contraction can be seen moving from Figures 5.2a to 5.2c. Hollow nanoparticles can be seen in Figure 5.2b, of which an example is shown in greater detail in the inset. A dark spot is noticed in the nanoparticles shown in the inset, which could be rationalised as a Ni cluster adhered to the inside of the NiO shell, similar to the schematic depicted in Figure 5.1.

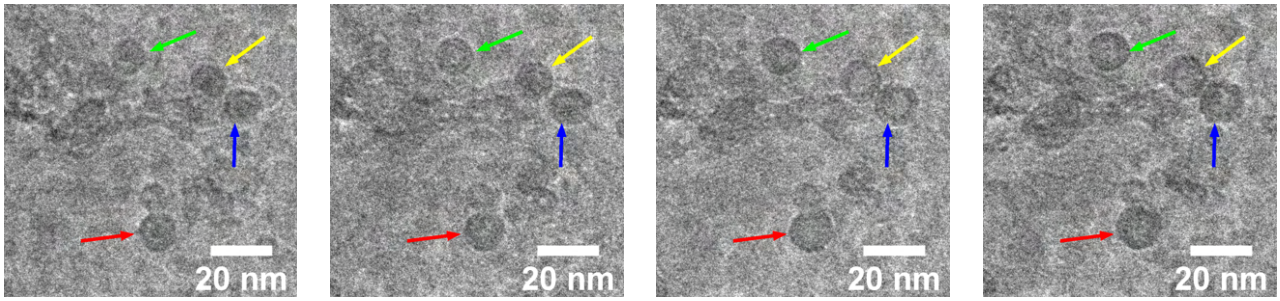

(a) t = 5 min, T = 201 °C (b) t = 30 min, T = 230 °C (c) t = 38 min, T = 278 °C (d) t = 49 min, T = 347 °C

Figure 5.3: TEM images of Ni nanoparticles on GNP500 during an *in situ* TEM experiment in O_2 at various time stamps and temperatures. The Ni nanoparticles shown here appeared to turn hollow over time, with only a small dark spot remaining at the inside of the hollow shell. All particles appeared to turn hollow at approximately the same time. This could be rationalised as a Ni cluster adhered to the inside of the NiO shell. The particles that show this hollowing out and corresponding size increase are denoted with the coloured arrows. An overview of their sizes at these points is shown in Figure 5.5.

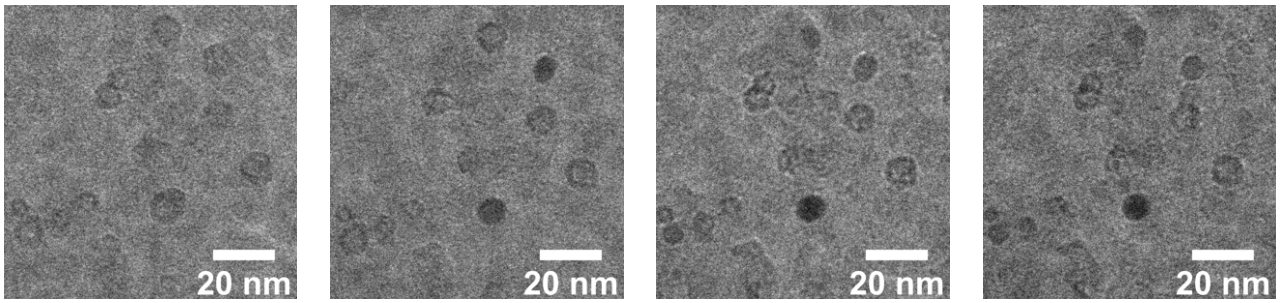

(a) t = 30 min, T = 281 °C (b) t = 40 min, T = 341 °C (c) t = 53 min, T = 350 °C (d) t = 83 min, T = 350 °C

Figure 5.4: TEM images of Ni nanoparticles on GNP500 during an *in situ* TEM experiment in H_2 at various time stamps and temperatures according to Section 5.1.2. The hollow NiO nanoparticles shown in Figure 5.4a shrink back to solid Ni nanoparticles (Figure 5.4d). These appear slightly smaller than their hollow NiO counterparts. Some particles remain hollow, even at 350 °C after 2 hours.

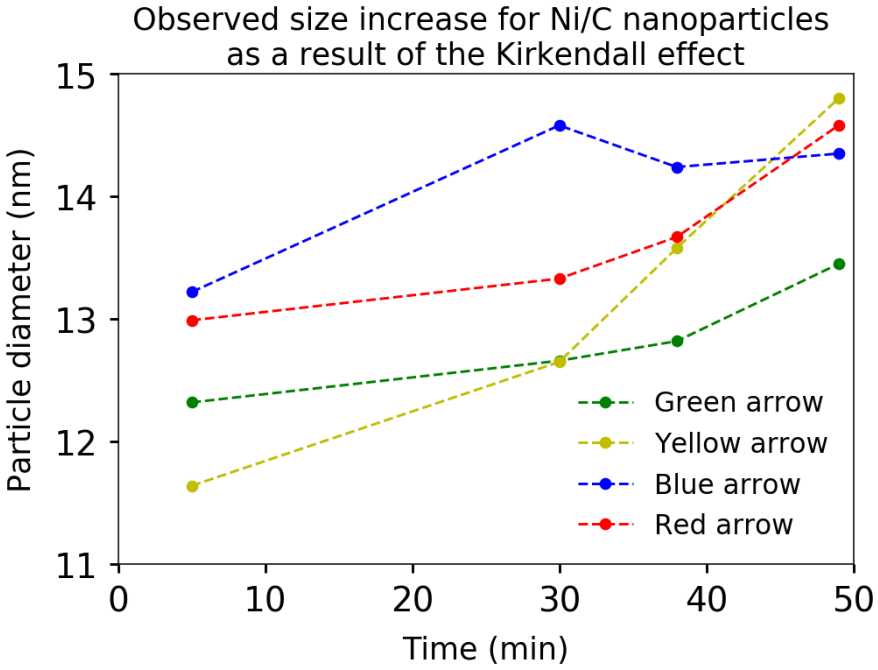

Figure 5.5: Observed particle diameter increase for the particles indicated with the coloured arrows in Figure 5.3. An average increase in particle diameter of 1.8 ± 0.8 nm was observed.

5.3 Conclusions and outlook

To summarize, here it was demonstrated that *in situ* electron microscopy could be a suitable method to investigate nanoscale effects on Ni nanoparticles. However, the limited resolution (compared to *ex situ* experiments) and the sensitivity to potential contaminants, as well as the limited amount of sample that can be imaged make external characterization absolutely essential for full understanding of effects such as the nanoscale Kirkendall effect. By correlating the *ex situ* experiments shown in Figure 5.2c to the *in situ* experiments shown in Figures 5.3 and 5.4, this chapter illustrates the possibility of using *ex situ* and *in situ* TEM techniques in tandem to investigate the same nanoscale behaviour at similar conditions. Using this unique combination, we might start to understand the various aspects of the Kirkendall effect that might influence it. For example, by studying differently sized particles, we might observe influences of Ni nanoparticle size on the Kirkendall effect, like Railsback et al observed for 9 and 26 nm Ni nanoparticles [83]. In addition, using the methods developed in this thesis, we could look at the Kirkendall effect on Ni nanoparticles supported on different materials. Studying the presented system (Figures 5.3 and 5.4) in more detail might reveal effects of Ni nanoparticle location on the support or their distance to other Ni nanoparticles. Studying these various aspects in detail might help understand when and why the Kirkendall effect occurs, giving fundamental understanding in our NiO/Ni nanoparticle system. This, in turn, might give insight in how to improve the Ni nanoparticle synthesis. Performing detailed analysis on the shell of the observed hollow particles might also give an indication what materials the shell contains, which in turn can help us understand how this effect is caused. In addition, using a lower temperature ramp or by keeping the sample at lower temperatures for longer times might help to identify possible difference based on particle size or location on the support material. Utilizing larger particles could also be very interesting, as they would provide better resolution.

Chapter 6

High pressure CO_2 hydrogenation

In this chapter, supported Ni NPs are tested using a high-pressure catalytic setup at various temperatures. Here, the activity of the catalysts at various temperature was investigated and the influence of various supports, as well as particle sizes on CO_2 methanation was investigated. The two supports were carbon based graphene nanoplatelets with an average BET surface area of 500 m^2/g and Davisil 643 silica with an average BET surface area of 300 m^2/g. A comparison between conventional impregnation catalysts, catalysts prepared using hot-injection and seed-mediated growth in OAm and OAc ligands and a catalyst synthesized using TOP ligands is also made, to identify the potential difference that ligand choice could have on catalysis. In addition, structural analysis based on TEM and XRD was used to identify differences in catalysts before and after catalysis. This chapter aims to answer the research questions found below:

- What is the influence of the support material on CO_2 hydrogenation?
- How do conventional impregnation catalysts compare to those prepared by colloidal synthesis?
- How do catalysts prepared using phosphorous-containing ligands compare to those prepared without phosphorous-containing ligands?

6.1 Results and discussion

6.1.1 Activity test

The first test that was performed is an exploratory activity test to determine whether the catalysts synthesized with these colloidal nanoparticles showed hydrogenation activity. Here, 4 and 7 nm Ni nanoparticles supported on Davisil 643 (SiO_2) and GNP500 (C) were tested. Samples of 4 nm Ni nanoparticles supported on SiO_2 and C were loaded double to determine whether the samples behaved homogeneously. An additional sample of 4 nm Ni nanoparticles supported on carbon was also tested determine the reproducibility of the synthesis procedure. This included a separate colloidal synthesis. The temperature program is indicated with the dotted lines in black. This program was chosen to investigate the dependence of CO_2 methanation on the reaction temperature. The catalytic test proceeded, after initial GC measurements at a low temperature of 240 °C, with GC measurements at 340 °C. This was done to ensure most restructuring of Ni nanoparticles took place at the beginning of the test, at the most extreme conditions. It then returned stepwise to 240 °C, taking measurements at the shown temperatures. Particle sizes indicated in the graphs within brackets correspond to the particle sizes after catalysis. It should be noted that in all cases the particles were much more polydisperse in their size after catalysis than before catalysis.

Figures 6.1 and 6.2 show summaries of the results of the first catalytic test for Ni/SiO_2 and Ni/C catalysts, respectively. In Figure 6.1a, the CO_2 conversion of Ni/SiO_2 catalysts is shown. The hollow cyan triangle represents the same catalyst as the solid cyan triangle. This catalyst was loaded double to test its homogeneity. The $Ni(8.6)/SiO_2$ catalysts both reached a conversion of approximately 87 %, which was very close to the equilibrium conversion at 340 °C of 88 % (Figure 1.1b). This also indicated that the doubly loaded catalyst behaved the same, indicating that the catalysts is homogeneous. The $Ni(10.7)/SiO_2$ had a much lower conversion of around 60 %. The silica support showed no conversion. To be able to more directly compare different catalysts, the activity of the catalysts was plotted in mol CO_2 s^{-1} mol_{Ni}^{-1}. This is shown in Figure 6.1b. Here, the difference between the smaller (intially 4 nm) and larger particles (initially 7 nm) was still present. CH_4 of the Ni/SiO_2 catalysts is shown in Figure 6.1c. Interestingly, for both the $Ni(8.6)/SiO_2$ catalysts as well as the $Ni(10.7)/SiO_2$ catalyst, the CH_4 selectivity at 240 °C at the start of the catalytic test is about 5 % lower than the CH_4 selectivity at 240 °C at the end of the catalytic test. As the CH_4 appeared to be highest at the highest temperature, the CH_4 selectivity was also plotted against the CO_2 conversion. This is shown in Figure 6.1d. Here, a clear trend was observed for both the $Ni(8.6)/SiO_2$ and the $Ni(10.7)/SiO_2$ catalysts. Increasing CO_2 conversion led to higher CH_4 selectivity. > 95 % CH_4 selectivity was reached at conversions above 60 %. The major side product which was observed in these cases was CO, which together with the CH_4 accounts for $>$ 99% of the products.

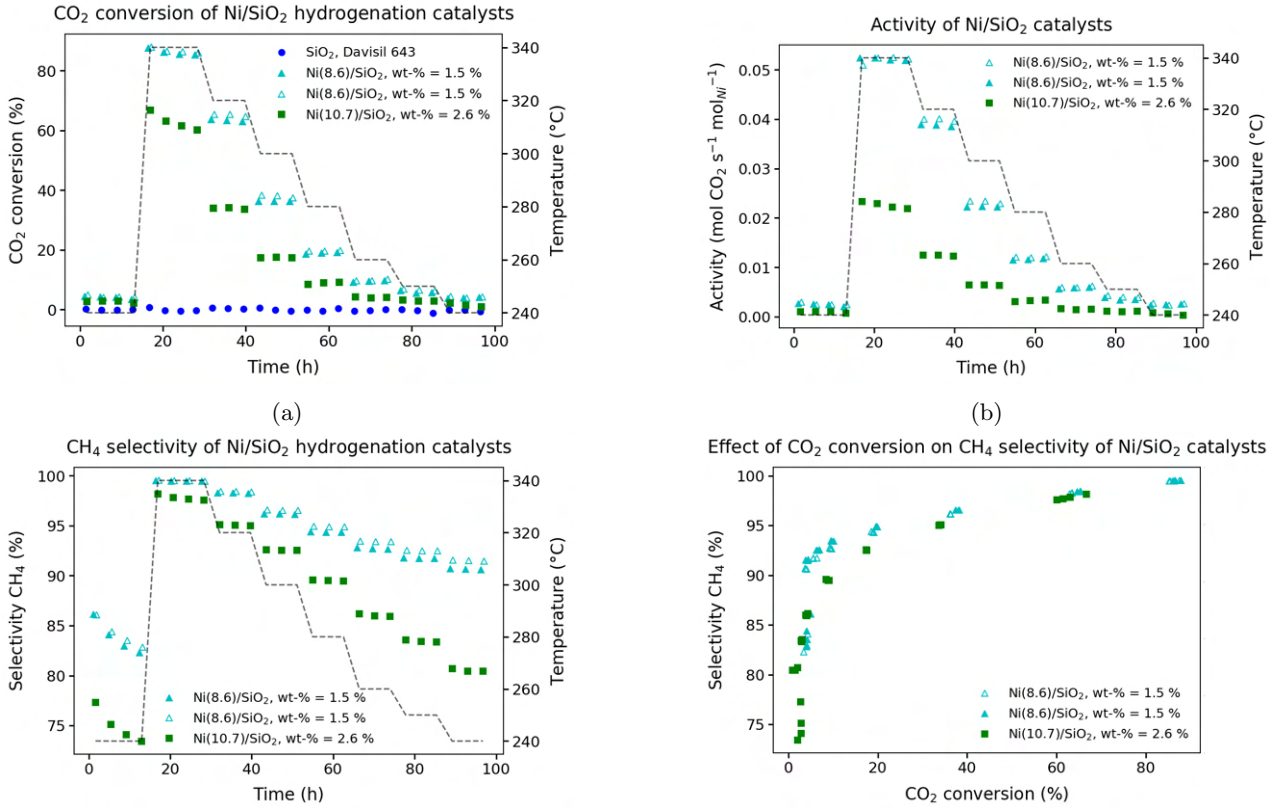

Figure 6.1: Overview of catalytic data obtained for Ni/SiO_2 catalysts from the activity test as described in Section 2.3.2. Reaction conditions: GHSV = 6000 mL g^{-1} h^{-1}, $p = 30$ bar, reaction mixture (in vol-%) = 5 % He, 75.64 % H_2 and 19.36 % CO_2. Temperatures ranged from 240 °C up to 340 °C, as indicated by the dotted black line. a) CO_2 conversion at various temperatures. Equilibrium conversions at 340 °C and 300 °C are around 88 and 93 %, respectively. The hollow cyan triangles correspond to the same sample as the solid cyan triangles, to test whether the sample performed homogeneously in catalysis. b) Catalyst activity at various temperatures. Activity of $Ni(8.6)/SiO_2$ was much higher than that of $Ni(10.7)/SiO_2$. c) CH_4 selectivity at various temperatures. Selectivity of Ni/SiO_2 catalysts was higher at 240 °C at the end of the catalytic test than at the start of the catalytic test at 240 °C. d) CH_4 selectivity as a function of CO_2 conversion. A trend of increasing CH_4 as a function of CO_2 is observed. $Ni(10.7)/SiO_2$ showed slightly lower CH_4 selectivity at similar CO_2 conversions, except at conversions near 60 %.

In Figure 6.2a, the CO_2 conversion of Ni/C catalysts is shown. 4 catalysts, as well as the carbon support material (GNP500) were tested. The hollow red diamond represents the same catalyst as the solid red diamond. This catalyst was loaded double to test its homogeneity. The doubly loaded catalyst showed similar conversions for both reactors, indicating that it was a homogeneous sample. All Ni/C catalysts shown here reached much lower CO_2 conversions than their Ni/SiO_2 counterparts shown in Figure 6.1a. Ni(11.7)/C showed the highest conversion of 28 % at 340 °C, far from equilibrium conversion of 88 % (Figure 1.1b). Activities of the Ni/C catalysts are shown in Figure 6.2b. Comparing these to those found for Ni/SiO_2 in Figure 6.1b, an large difference was noted in activities. Ni/SiO_2 performed much better than their Ni/C counterparts at most temperatures. This huge difference between activities appears to indicate a significant support effect. This could be caused by strong adsorption of CO_2 and possible activation to CO^* on SiO_2 [28]. This hypothesis was also supported by the fact that the SiO_2 support itself does not show any activity, so it did not actively hydrogenate CO_2 by itself, but needed Ni to do so. CH_4 selectivity of the Ni/C catalysts was also investigated and shown in Figure 6.2c Here, in contrast to the results shown in Figure 6.1c, the Ni/C catalysts had a lower selectivity at 240 °C after catalysis than at 240 °C before catalysis, despite showing similar CO_2 conversion. Ni(7.1)/C, Ni(7.8)/C and Ni(11.7)/C show a drop of around 15, 30 and 40 % in CH_4 selectivity, respectively. Comparing this to the 5-10 % increase in CH_4 selectivity observed for Ni/SiO_2 at the beginning of the test at 240 °C compared to the end of the test at 240 °C reveals another difference between the two support materials. Both Ni/SiO_2 and Ni/C catalysts showed some initial deactivation at 240 °C and 340 °C, but appeared relatively stable afterwards (shown in Figures 6.1a and 6.2a. This deactivation appeared to be accompanied by a corresponding decrease in selectivity, shown in Figures 6.1c and 6.2c. To summarize, we can see that for Ni/C, catalysts with a higher Ni wt-% have higher selectivity and conversion. Logically, a higher Ni wt-% leads to a higher CO_2 conversion, which has been shown to have strong correlation with CH_4 selectivity. However, decreasing CH_4 selectivity is also observed for decreasing Ni wt-% at the same CO_2 conversions for Ni/C catalysts. This difference in CH_4 selectivity can therefore not be explained through the dependency on CO_2 conversion.

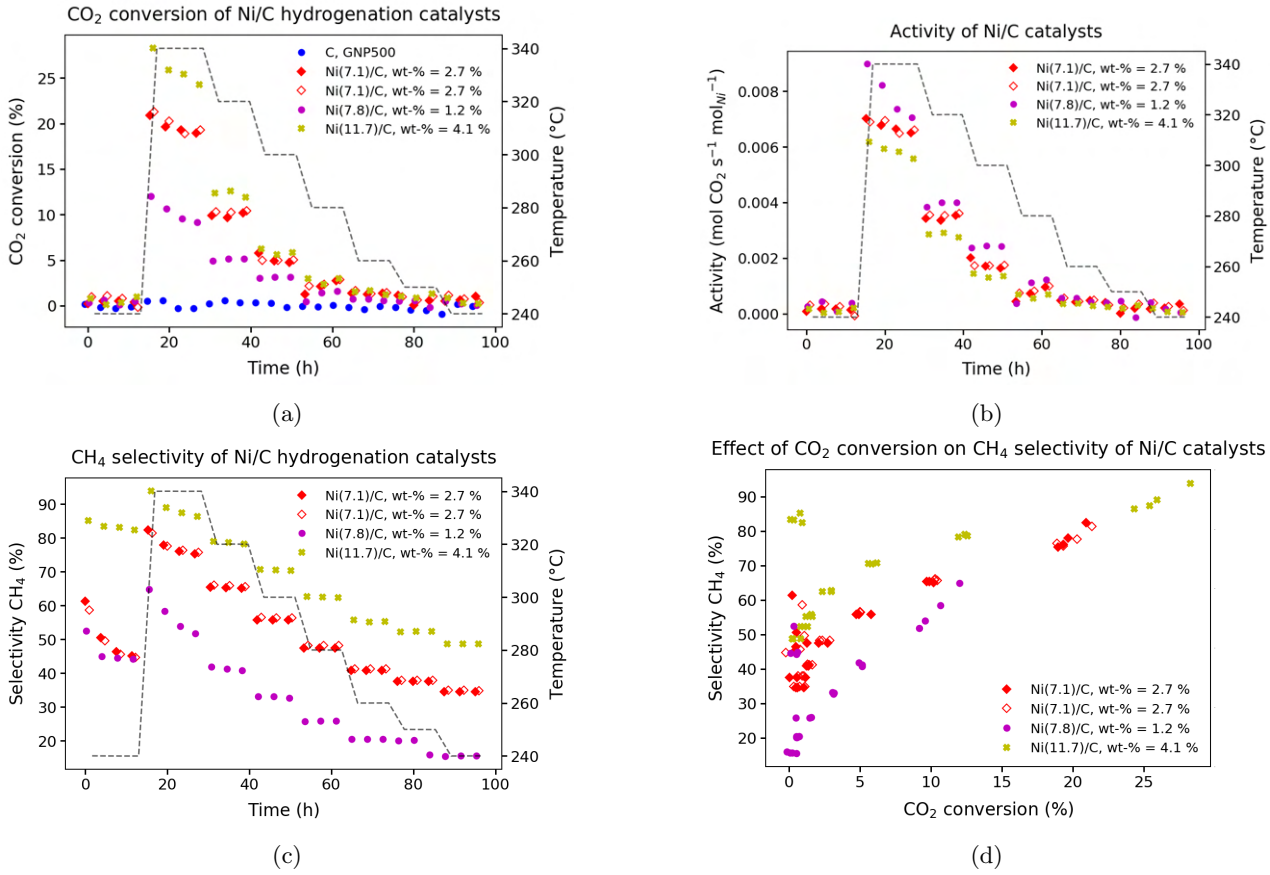

Figure 6.2: Overview of catalytic data obtained for Ni/C catalysts from the activity test as described in Section 2.3.2. Reaction conditions: GHSV = 6000 mL g^{-1} h^{-1}, p = 30 bar, reaction mixture (in vol-%) = 5 % He, 75.64 % H_2 and 19.36 % CO_2. Temperatures ranged from 240 °C up to 340 °C, as indicated by the dotted black line. a) CO_2 conversion plotted against time on stream. Highest CO_2 conversions was found for the highest wt-% Ni/C samples. The carbon support material (GNP500) itself showed no conversion. b) Activity plotted against time on stream. The tested Ni/C samples showed similar activities. c) CH_4 selectivity plotted against time on stream. Highest selectivity was observed at the highest temperature for all samples. Selectivity at 240 °C at the beginning of the test was lower than selectivity at 240 °C at the end of the test. d) CH_4 selectivity plotted against CO_2 conversion. A similar trend as observed in Figure 6.1d was observed for the Ni/C catalysts, with increasing CH_4 selectivity for increasing CO_2 conversion. At most CO_2 conversions, the Ni/C with lower Ni wt-% showed lower CH_4 selectivity, indicating a dependence on Ni wt-%.

The particle sizes indicated in the graphs correspond to average particle sizes, but the catalysts showed significant sintering after catalysis and much larger size distributions. Shown in Figures 6.3 and 6.5 are TEM images of Ni seeds supported on Davisil 643 and GNP500, respectively. In Figures 6.4 and 6.6, the corresponding X-ray diffractograms are shown. Significant particle growth is observed in the TEM images for the supported Ni NPs, with most growth occurring on Davisil 643. X-ray diffraction did not reveal any reflections for large Ni crystallites for the Ni seeds supported on GNP500. However, Ni seeds supported on SiO_2 show reflections at 41°, 52°, 61°and 84°as shown in Figure 6.4, which indicates the presence of larger Ni crystallites, which are easily visible in Figure 6.3b.

Shown in Figure 6.7 are TEM images of larger Ni NPs supported on GNP500, after calcination at 250 °C in O_2 for 2 h and reduction at 350 °C in H_2 for 2 h (Figure 6.7a) and after catalysis Figure 6.7b. Irregularly shaped Ni NPs are observed in different sizes. Corresponding X-ray diffraction reveals the presence of large Ni crystallites with reflections present at 52°and 61°. Similar results are found for Ni/SiO_2, where very large Ni NPs are found in the TEM images shown in Figures 6.9a and 6.9b. XRD corroborates these results, as reflections for 52°and 61°indicate the presence of large Ni crystallites. For the samples on silica, Ni particles as large as 100 nm are found, and for the carbon samples around 50 nm.

Sintering appears much more prominent on the Davisil 643 as compared to the GNP500. This could be caused by the large difference in support surface area (300 m^2/g for Davisil 643 compared to 500 m^2/g for GNP500), leading to relatively smaller interparticle distance and higher probability for particle growth. These large particle diameters and in particular the broad size distributions made comparison based on turnover-frequency of the catalysts difficult. A graph plotting the TOFs of the samples shown here is given in Figure A.31. Larger, 11.7 ± 4.3 nm Ni/C appeared to have a very similar TOF compared to smaller 8.6 ± 2.0 Ni/C catalysts, as errorbars nearly overlap. For Ni/SiO_2, the errorbars were so large that comparison was not possible.
Activation energies of the Ni/SiO_2 and Ni/C catalysts were determined according to the Arrhenius equation and the relevant ln(k) vs 1/T plot is shown in Figure A.32. These activation energies were all very similar.

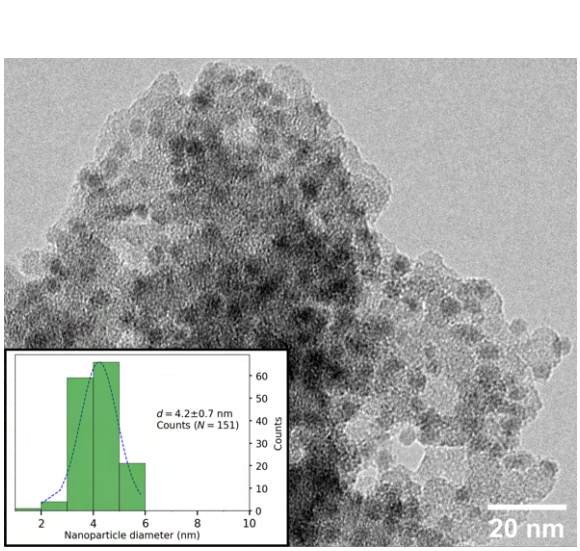

(a) Ni(4.2 ± 0.7)/SiO_2

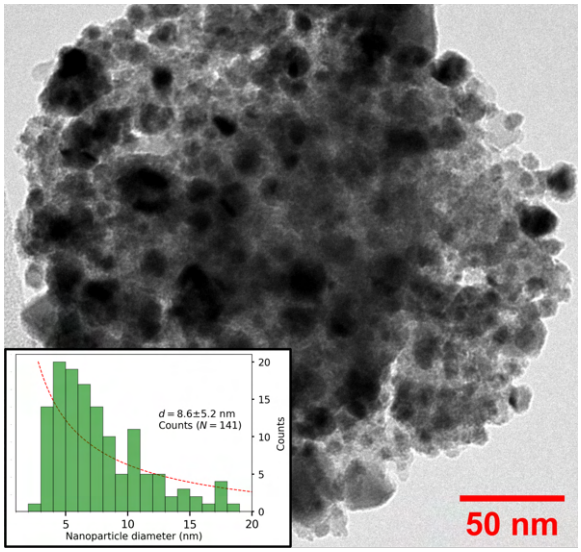

(b) Ni(8.6 ± 5.2)/SiO_2

Figure 6.3: TEM images of Ni seeds supported on Davisil 643 a) after deposition and b) after catalysis. Particles have grown significantly and a much broader size distribution is obtained.

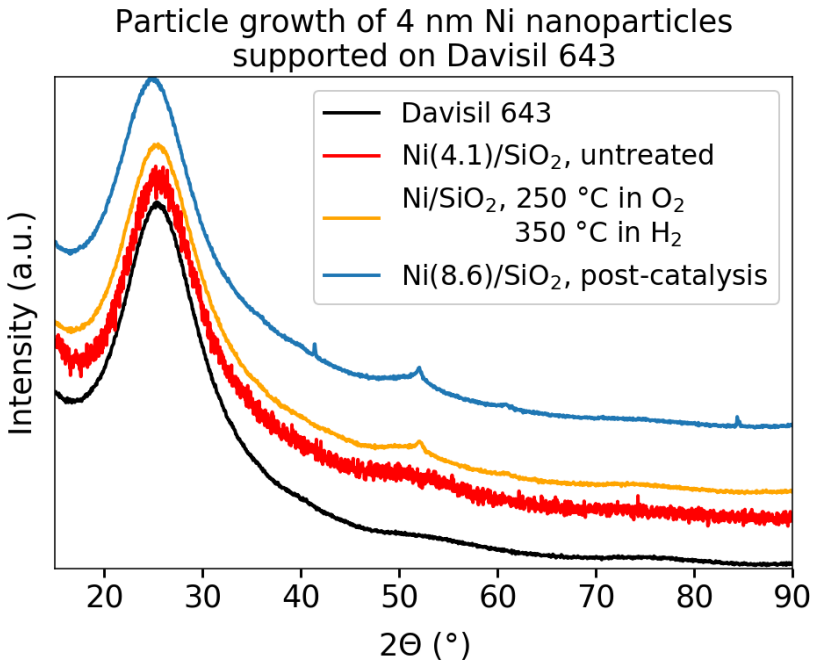

Figure 6.4: XRD of Ni/SiO_2 during various stages of catalyst development and after catalysis. The appearance of reflections near 41˚, 52˚, 61˚and 84˚, corresponding to Ni(111), Ni(200), Ni(220) and Ni(311), indicates the presence of larger crystallites, also observed in TEM.

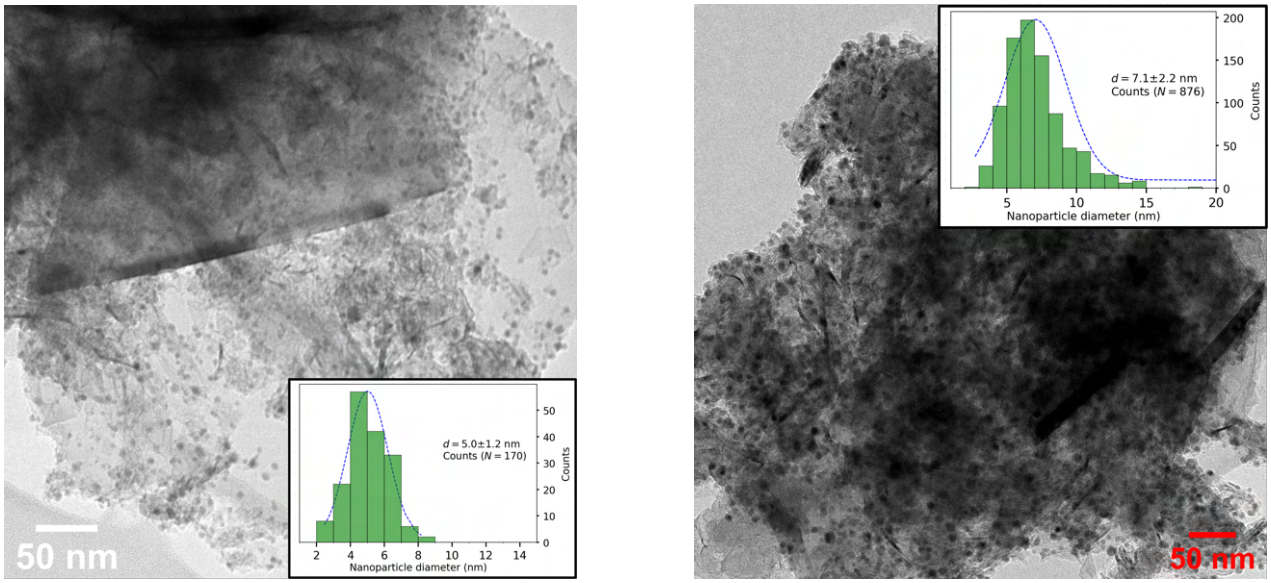

(a) Ni(5.0 ± 1.2)/C

(b) Ni(7.1 ± 2.2)/C

Figure 6.5: TEM images of 4 nm Ni seeds supported on GNP500 a) after heat treatments and b) after catalysis.

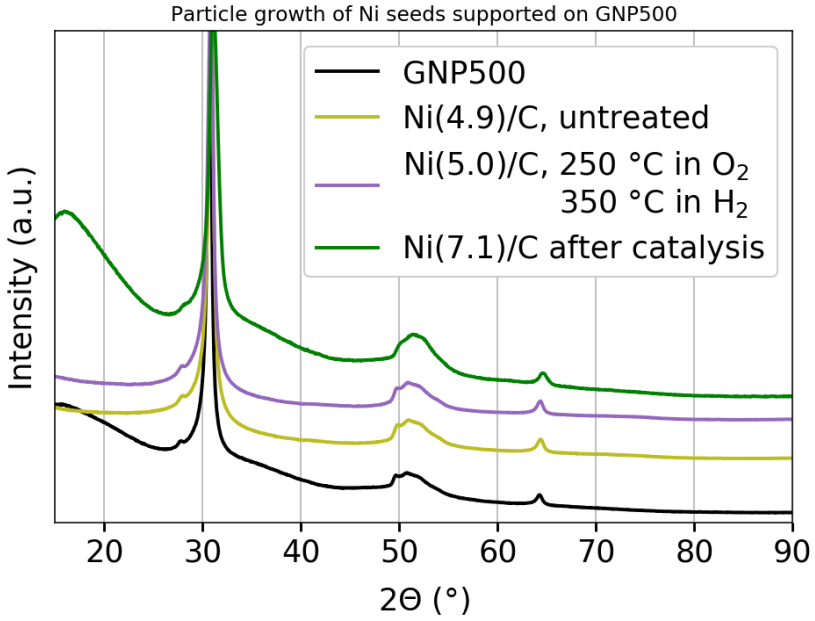

Figure 6.6: XRD of Ni/C during various stages of catalysts development and after catalysis. The broad reflection near 18˚corresponds to the sample holder, and is only observed when using a small amount of sample, which is the case for the samples after catalysis. No reflections corresponding to metallic Ni can be discerned, indicating the lack of large crystalline particles.

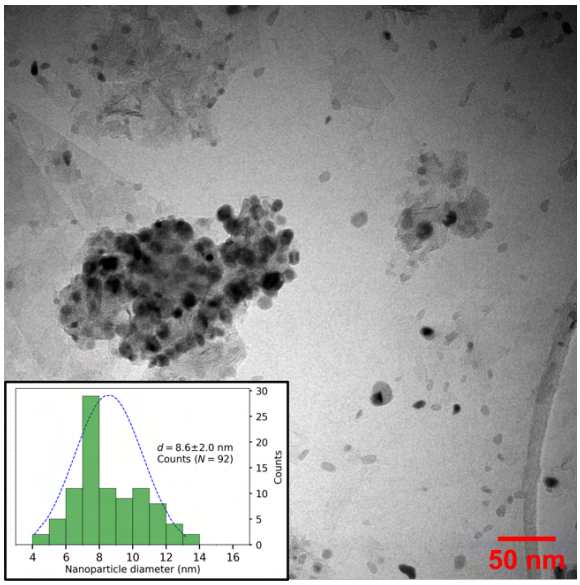

(a) Ni(8.6 ± 2.0)/C

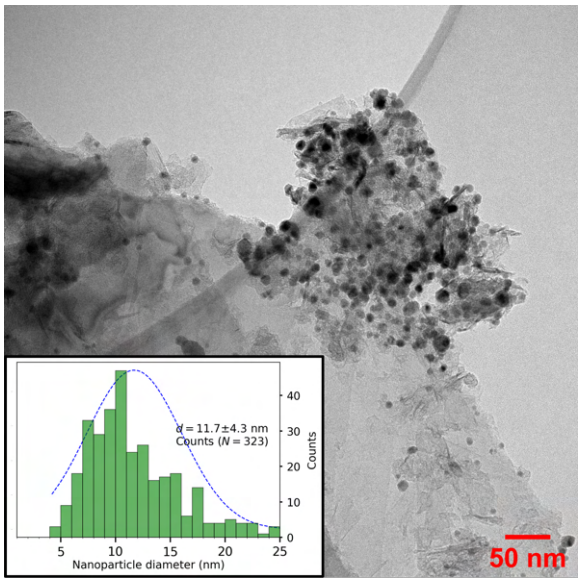

(b) Ni(11.7 ± 4.3)/C

Figure 6.7: TEM images of larger Ni NPs supported on GNP500 a) after heat treatments and b) after catalysis. In Figure 6.7a, irregular shapes and sizes are observed for the Ni NPs, in contrast to the particles observed in Figure 4.16c. This difference is thought to be caused by the difference in Ni wt-% (4.1 vs 1.7%), leading to smaller interparticle distance and more significant sintering.

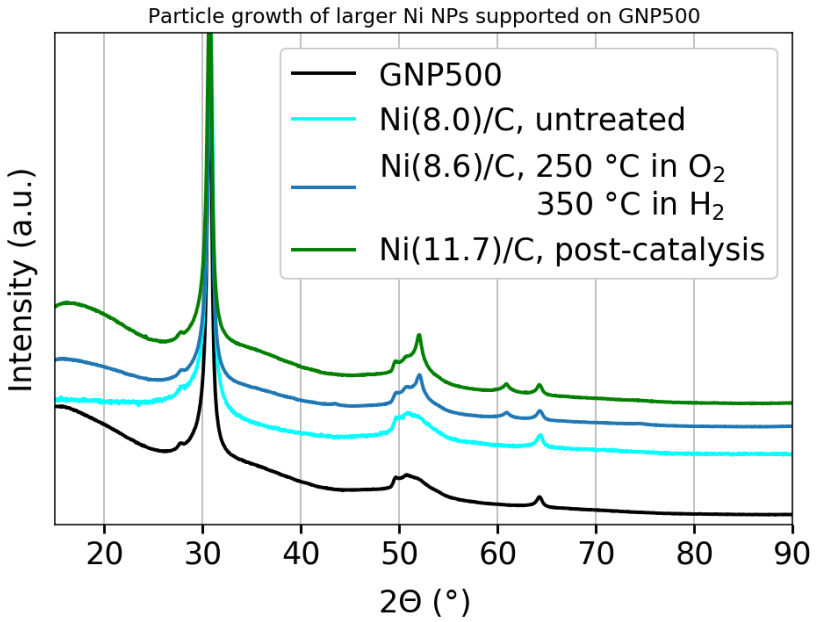

Figure 6.8: XRD of Ni/C during various stages of catalysts development and after catalysis. The broad reflection near 18˚corresponds to the sample holder, and is mainly observed when using a small amount of sample, which is the case for the samples after catalysis. For the catalyst directly before and after catalysis, reflections at 52˚and 61˚are observed. These corresponds to Ni(200) and Ni(220) respectively.

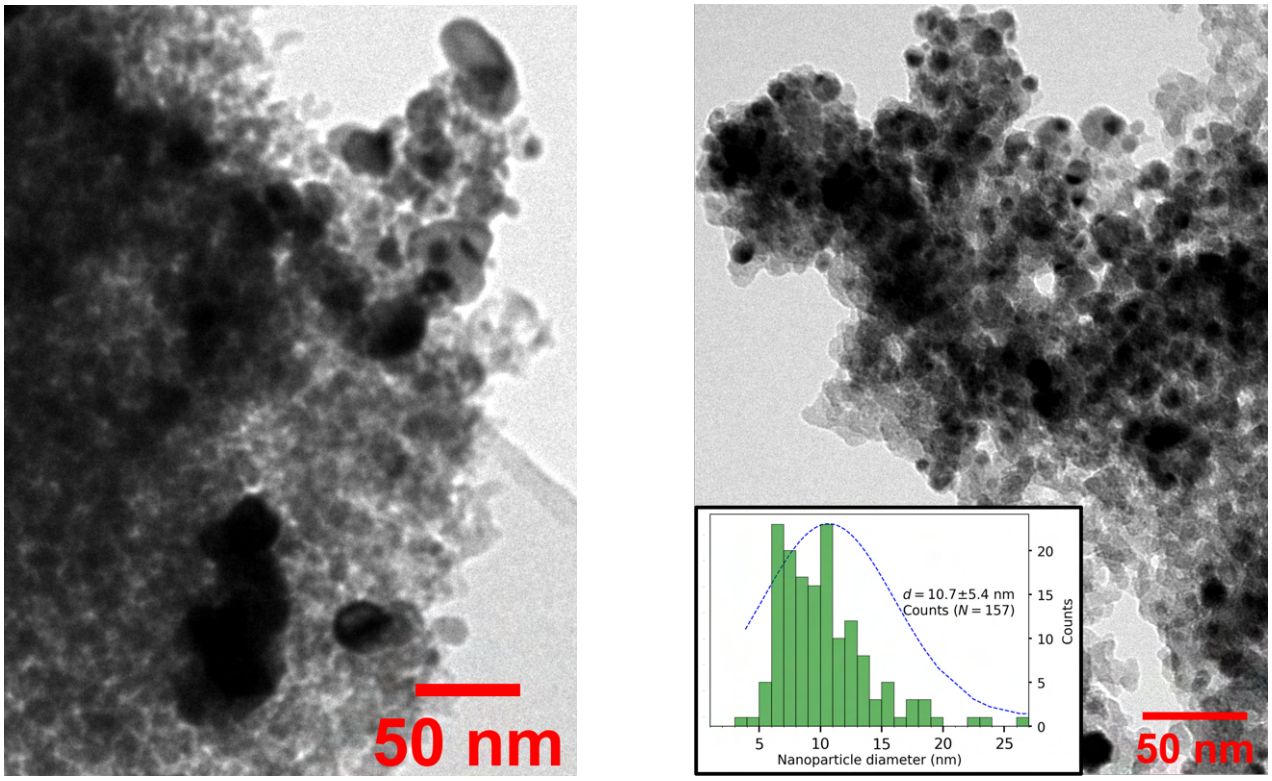

(a) Ni/SiO_2 (b) $Ni(10.7 \pm 5.4)/SiO_2$

Figure 6.9: TEM images of larger 7 nm Ni NPs supported on SiO_2 a) after heat treatments and b) after catalysis. A very broad particle diameter distribution is observed for both samples.

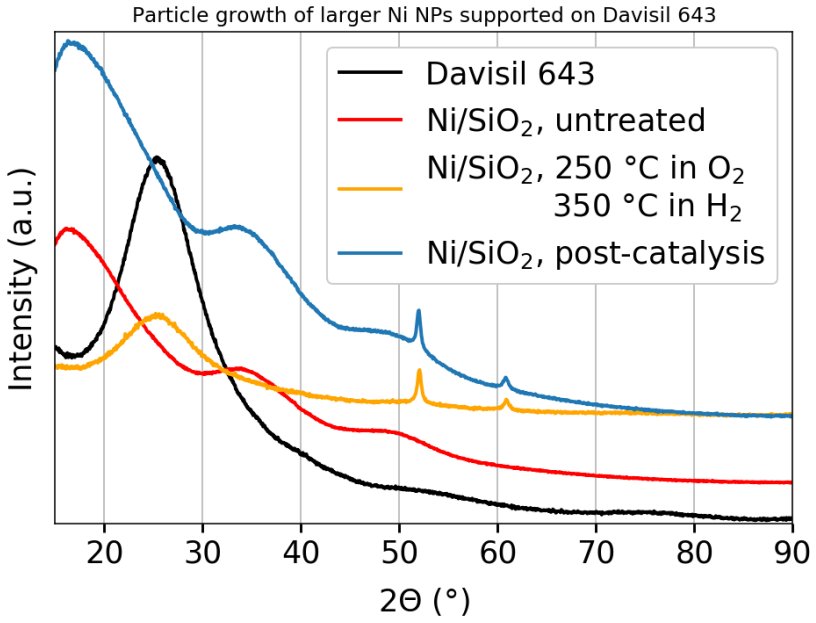

Figure 6.10: XRD of Ni/SiO_2 during various stages of catalyst development and after catalysis. Broad reflections at 18˚, 34˚and 48˚correspond to the sample holder and are mainly observed when using little sample. The sharp reflections at 52˚, 61˚correspond to metallic nickel, and indicate the presence of large crystallites.

6.1.2 Combined activity and stability test

Activity test

This catalytic test consisted of a combined activity and stability test. Here, the influence of synthesis methods on catalytic performance of Ni/C and Ni/SiO_2 catalysts was investigated. Two Ni/C catalysts prepared through incipient wetness impregnation were tested (IWI:Ni/C). These were exposed to different heat treatments before catalysis, 1) first a heat treatment in N_2 at 350 °C with a ramp of 2 °C/min, then a calcination in O_2 at 250 °C with a ramp of 5 °C/min and a subsequent reduction in H_2 at 350 °C with a ramp of 5 °C/min and 2) a heat treatment in N_2 at 400 °C with a ramp of 2 °C/min and a reduction in H_2 at 350 °C with a ramp of 2 °C/min. This was done to investigate the influence of the heat treatment on the Ni/C catalysts, and allow for a more direct comparison of the IWI:Ni/C catalysts to the Ni/C catalysts prepared with colloidal methods. In addition to this, a Ni/SiO_2 catalyst which was prepared using trioctylphosphine to synthesize the deposited colloids was also tested. Comparable Ni/SiO_2 catalysts prepared using phosphorous-free methods were also investigated here. The activity test had a temperature program according to the dotted line in black shown in the graphs of Figure 6.11. Shown in Figure 6.11 is an overview of the catalytic data which was obtained. First, initial GC measurements are taken at 240 °C, before heating to 340 °C where additional GC measurements were taken. Subsequently, the temperature was reduced stepwise to 240 °C again. This temperature program was chosen to expose the catalysts to the most extreme conditions initially to make sure most nanoparticle restructuring takes places here. Numbers indicated in brackets in the legends of each graph point to particle diameter after catalysis when available. Ni wt-% is also indicated where available. In Figure 6.11a, the CO_2 conversion of Ni/SiO_2 catalysts prepared using colloidal methods with and without phosphorous-containing ligands is depicted. The Ni_xP_y/SiO_2 indicated in purple showed similar CO_2 conversion as the SiC diluent. This meant the Ni_xP_y/SiO_2 was inactive as a catalysts. In contrast, Ni/SiO_2 prepared with phosphorous-free colloids showed significant conversion. ICP-OES data indicated that the Ni_xP_y had a P wt-% of 0.25 % and a Ni wt-% of 0.75 %. Additionally, the two Ni/SiO_2 catalysts showed similar catalytic performance, despite the different treatments. This indicates that the presence of phosphorous clearly hampers the catalytic performance for CO_2 methanation of Ni/SiO_2 catalysts. To further illustrate this result, the activity of the catalysts was also plotted in Figure 6.11b, which underlines this result.

In Figure 6.11c, the CO_2 conversion of the IWI:Ni/C catalysts was compared to the CO_2 conversion of comparable Ni/C catalysts prepared through colloidal methods. A clear difference in CO_2 conversion was observed, with the IWI:Ni/C catalysts outperforming the Ni(7.7)/C at every temperature. It should be noted that the Ni wt-% indicated in this graph for the IWI:Ni/C catalysts was based on the impregnated volume of the carbon support with a known solution of $Ni(NO_3)_2.6H_2O$. The Ni wt-% for the Ni(7.7)/C was determined based on TGA-results, according to Equation (2.2). Catalyst activity was plotted in Figure 6.11d, and showed the same results. A difference between the IWI:Ni/C catalysts was also noted, with the IWI:Ni/C catalyst which was calcined at 250 °C in O_2 performing slightly worse than the IWI:Ni/C catalyst which was not calcined. Possibly, the calcination treatment has had an influence on the Ni nanoparticle structure or size, which could influence its catalytic properties, although this was not yet investigated. The difference between IWI:Ni/C and Ni/C prepared through colloidal methods might be explained through the potential doping of the Ni nanoparticles with boron. However, this was not investigated in this thesis.

In Figure 6.11e, the CH_4 selectivity of the tested catalysts is plotted. Here, the IWI:Ni/C catalysts show the highest selectivity, as well as increased selectivity at 240 °C at the end of the catalytic test compared to their selectivity at 240 °C at the beginning of the catalytic test. This was also observed for the $Ni(9.5)/SiO_2$) catalyst. The opposite was observed for the Ni(7.7)/C catalyst. Shown in Figure 6.11f is the CH_4 selectivity plotted against the CO_2 conversion. Taking into account the previously observed trends where increasing CO_2 conversion appeared to coincide with increasing CH_4 selectivity, the samples here showed similar results. The IWI:Ni/C catalysts showed the highest CH_4 selectivity at similar conversions. Ni/SiO_2 and Ni/C prepared through colloidal methods showed similar selectivity at similar conversions.

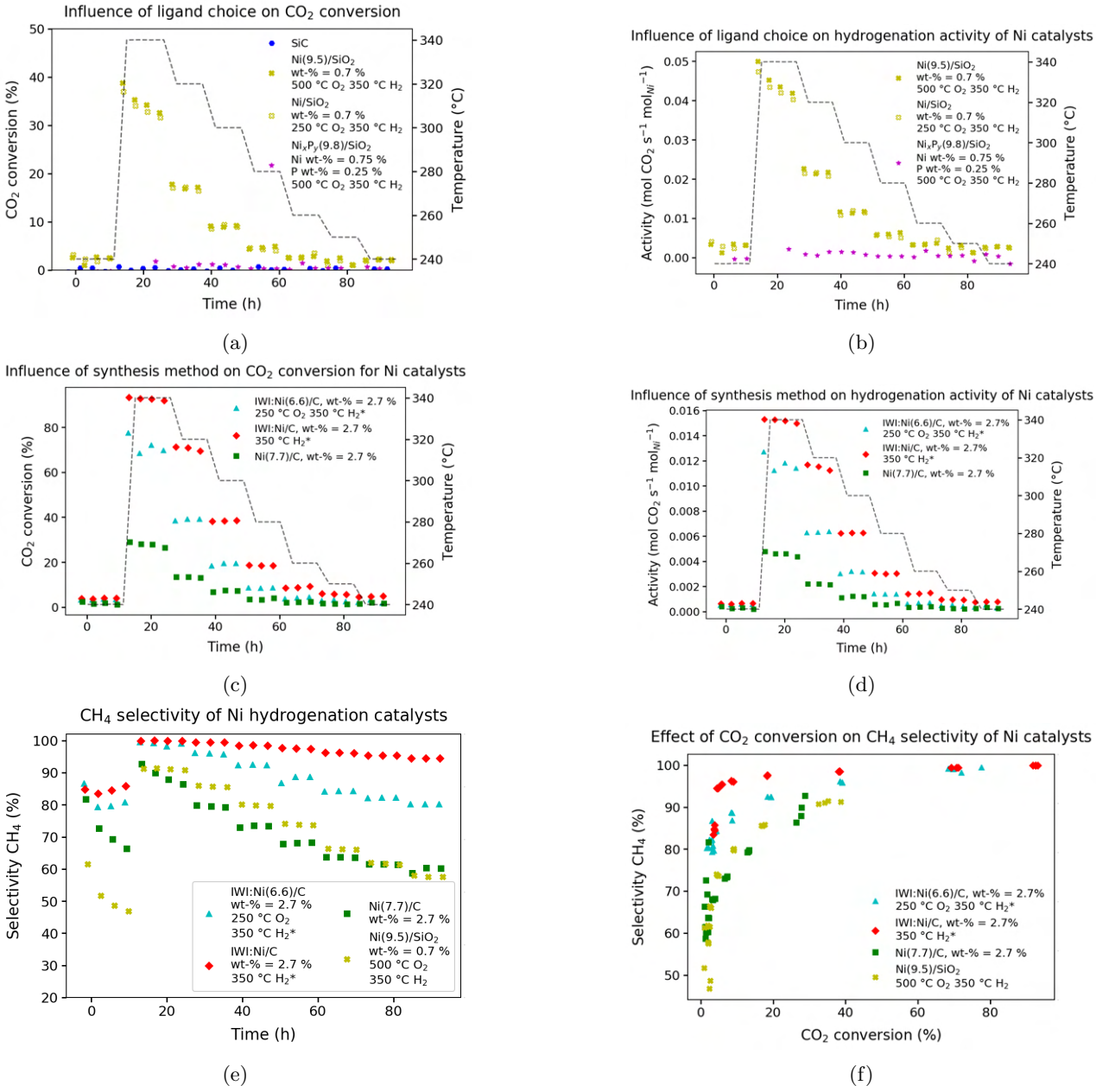

Figure 6.11: Overview of catalytic data obtained for supported Ni NP catalysts made in various ways. Reaction conditions: GHSV = 6000 mL g^{-1} h^{-1} for Ni/SiO_2 catalysts and 3000 mL g^{-1} h^{-1} for Ni/C catalysts, p = 30 bar, reaction mixture (in vol-%) = 5 % He, 75.72 % H_2 and 19.28 % CO_2. Temperatures ranged from 240 °C up to 340 °C, as indicated by the dotted black line. a) CO_2 conversions at various temperatures. Ni/SiO_2 treated at 250 °C or at 500 °C in O_2 for 2 h showed identical conversions. Ni_xP_y/SiO_2 showed almost no CO_2 conversion. b) Activity for Ni/SiO_2 vs Ni_xP_y/SiO_2 showed inactive NiP. c) Comparison in CO_2 conversion for different synthesis methods. Difference in heat treatments on IWI catalysts decrease activity, with comparable Ni/C samples prepared with colloids showing much lower activity. d) Hydrogenation activity of Ni/C catalysts showed the same effect. e) CH_4 selectivity of various Ni catalysts. Both Ni/SiO_2 and IWI:Ni/C catalysts showed an increase in CH_4 selectivity at 240 °C at the end of the catalytic test compared to the start of the test. Ni(7.7)/C showed a decrease in CH_4 when comparing the start to the end of the test at 240 °C, similar to those samples found in Figure 6.2c. f) CH_4 selectivity plotted against CO_2 conversion showed a dependence of CH_4 selectivity on CO_2 conversion. Catalysts prepared using colloidal methods showed similar CH_4 selectivity at similar conversion, but these were lower than comparable IWI:Ni/C catalysts. *Catalyst Ni wt-% was calculated according to impregnated volume and measured density of a $Ni(NO_3)_2.6H_2O$ solution.

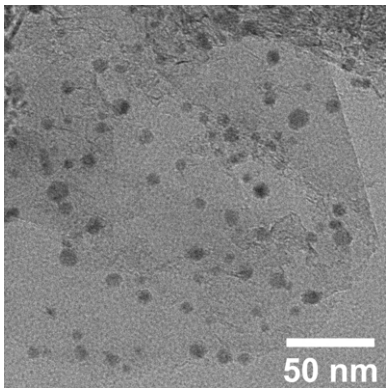

(a) Ni(7.7 ± 1.7)/C, Ni wt-% = 2.7 %

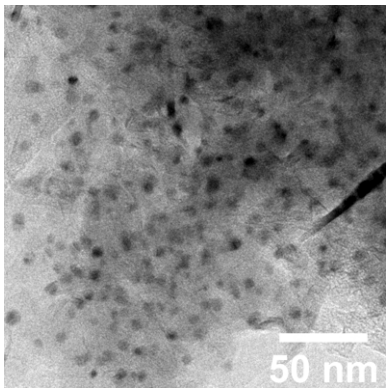

(b) Ni(6.6 ± 1.0)/C, Ni wt-% = 2.7 %

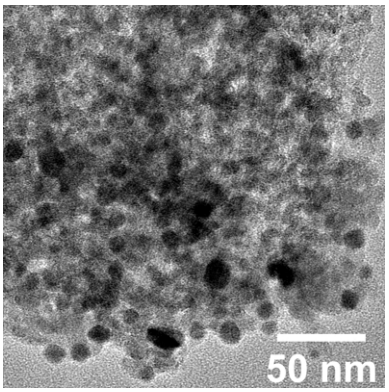

(c) Ni(9.8 ± 2.1)/SiO_2, Ni wt-% = 0.7, P wt-% = 0.25 %

Figure 6.12: TEM images of the Ni_xP_y catalyst and comparable Ni/C and IWI:Ni/C catalysts after catalysis. While not showing any activity, the Ni_xP_y catalyst showed some sintering, especially when compared to the Ni/C catalysts.

Depicted in Figure 6.12 are TEM images of the Ni_xP_y catalyst and Ni/C and IWI:Ni/C catalysts after catalysis. Both the Ni(7.7)/C and the IWI:Ni(6.6)/C catalysts show relatively monodisperse particle diameter distributions (Figures 6.12a and 6.12b). The Ni_xP_y catalyst shows some sintering compared to the result after heat treatments and EDX-measurements revealed there was still phosphorous present in the sample. This indicated that the particles visible in Figure 6.12c likely still have incorporated phosphorous. This incorporated phosphorous was suspected to be the reason this Ni_xP_y catalyst shows no CO_2 hydrogenation activity.

Stability test at constant temperature

The stability test was performed at a constant temperature of 300 °C. In this test, the IWI:Ni/C catalysts as well as various Ni/C catalysts prepared through colloidal methods and a Ni/SiO_2 catalyst were investigated for their stability over time at elevated temperatures. Shown in Figure 6.13 is an overview of the catalytic data which was obtained. In Figure 6.13a, the CO_2 conversion of the various catalysts is depicted. Here, the IWI:Ni/C and the Ni/SiO_2 catalysts showed the highest conversion, with the Ni/C catalysts prepare through colloidal methods showing stable conversion between 3-8 %. The lowest conversion was observed for the Ni/C catalysts with the lowest Ni wt-%. The IWI:Ni/C catalysts showed an initial activation where conversion increased, followed by a decrease in CO_2 conversion over the course of the test. The Ni/SiO_2 showed deactivation over the entire catalytic test. Converting the CO_2 conversion into activity (depicted in Figure 6.13b) showed that the $Ni(5.4)/SiO_2$ was much more active than all Ni/C catalysts prepared, similar to the differences seen between Figures 6.11b and 6.11d and Figures 6.1b and 6.2b. Activities of all Ni/C catalysts prepared using colloidal methods were similar. Shown in Figure 6.13c is the CH_4 selectivity of the tested catalysts. The IWI:Ni/C and Ni/SiO_2 catalysts showed stable CH_4 selectivity above 90 %, whereas the Ni/C catalysts prepared through colloidal methods showed more significant decrease in selectivity. Here, the lowest Ni wt-% catalyst showed the lowest CH_4 selectivity and a decrease of about 20 %. The other Ni/C catalysts showed a reduction of about 10 % in CH_4 selectivity. In Figure 6.13d, the CH_4 selectivity is plotted against the CO_2 conversion. Here, the comparable Ni/C catalysts showed similar CH_4 selectivity at similar conversion. From this graph, it became clear that the $Ni(5.4)/SiO_2$ showed lower CH_4 selectivity even at the same CO_2 conversion when compared to the IWI:Ni/C catalysts, which was also observed in Figure 6.11f. However, the opposite was seen when comparing the Ni/SiO_2 catalysts to comparable Ni/C catalysts when both were prepared with colloidal methods.

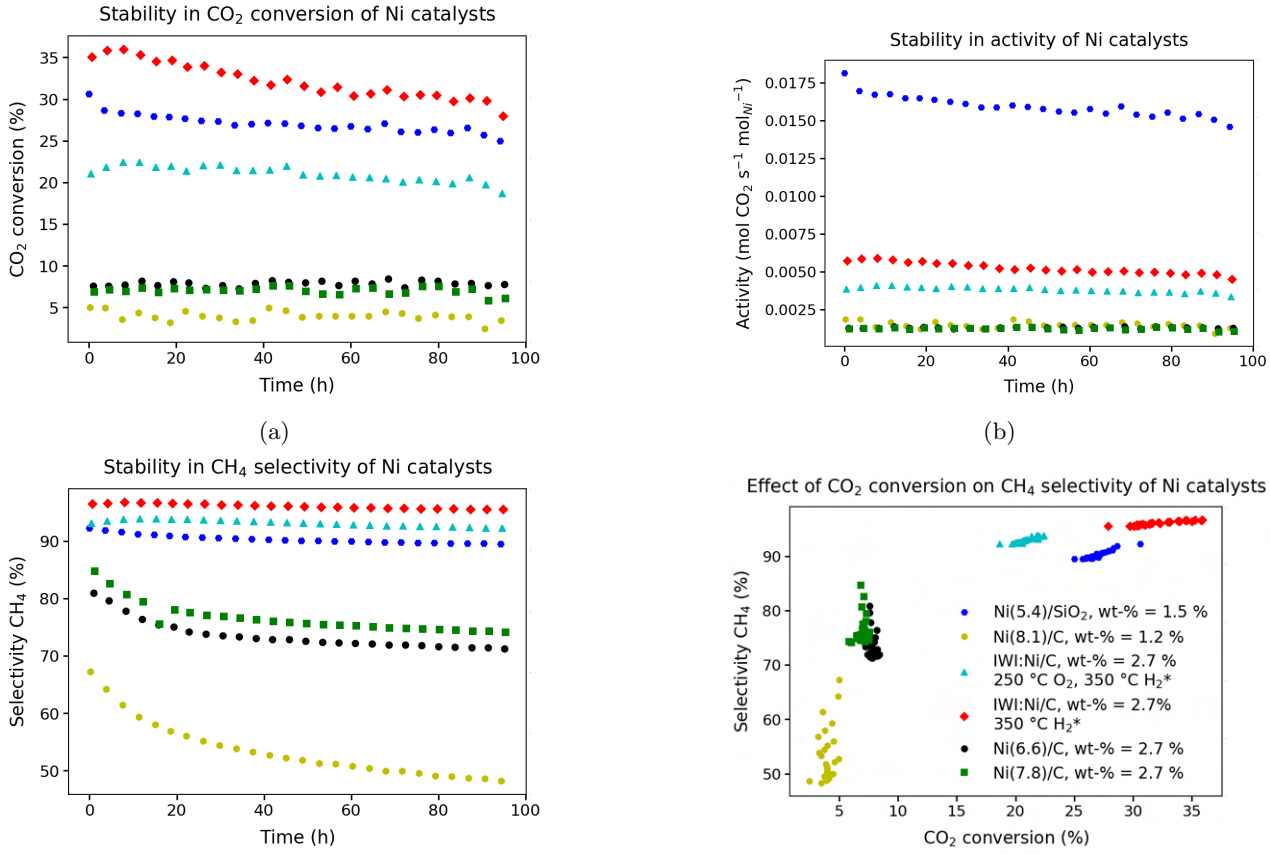

Figure 6.13: Overview of catalytic data obtained for supported Ni NP catalysts made in various ways. Legend for all tested catalysts is shown in the bottom right graph. Reaction conditions: GHSV = 6000 mL g^{-1} h^{-1} for Ni/SiO_2 catalysts and 3000 mL g^{-1} h^{-1} for Ni/C catalysts, $p = 30$ bar, reaction mixture (in vol-%) = 5 % He, 75.72 % H_2 and 19.28 % CO_2. Temperature was kept constant at 300 °C. a) CO_2 conversions for the various catalysts. Both IWI:Ni/C catalysts showed initial activation. $Ni(5.4)/SiO_2$ showed catalyst deactivation from about 30 % to 25 %. Colloidally prepared Ni/C catalyst remained at similar conversions throughout, with the lowerst wt-% showing the lowest conversion. b) Activity revealed that the $Ni(5.4)/SiO_2$ is much more active than the Ni/C catalysts. In turn, the IWI:Ni/C show higher activities than their colloidally prepared Ni/C counterparts. c) CH_4 selectivity of the Ni/C catalysts decreased, with the lowest Ni wt-% showing the largest decerease. The IWI:Ni/C and Ni/SiO_2 remained stable at above 90 %. d) CH_4 selectivity plotted against CO_2 conversion revealed increasing CH_4 selectivity at increasing CO_2 conversion at CO_2 conversion of > 20 % for Ni/SiO_2 and IWI:Ni/C. Ni/C prepared through colloidal methods showed decreasing CH_4 selectivity even at the same CO_2 conversions. *Catalyst Ni wt-% was calculated according to impregnated volume and measured density of a $Ni(NO_3)_2.6H_2O$ solution.

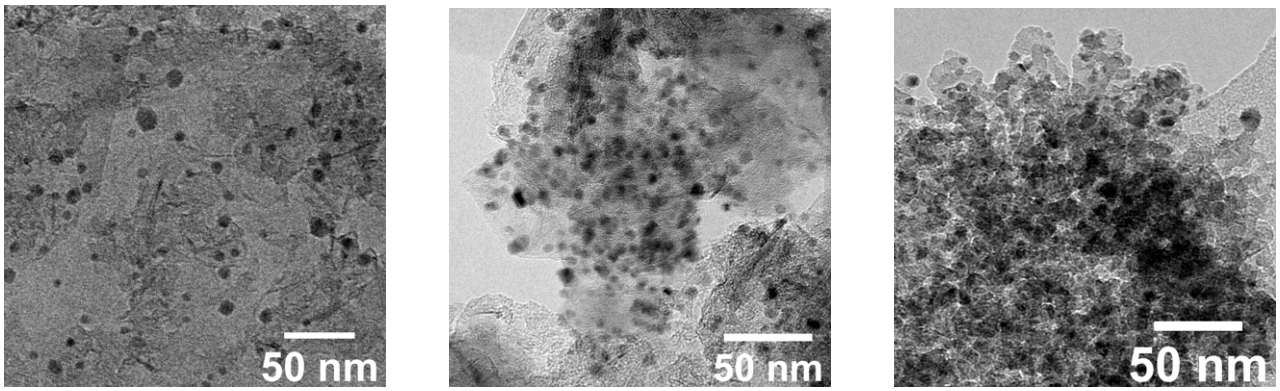

(a) Ni(7.7 ± 1.8)/C (b) Ni(6.6 ± 1.5)/C (c) Ni(5.4 ± 1.7)/SiO_2

Figure 6.14: Overview of the Ni nanoparticle sizes after a catalytic test at constant 300 °C for GHSV = 6000 mL g^{-1} h^{-1} for Ni/SiO_2 catalysts and 3000 mL g^{-1} h^{-1} for Ni/C catalysts, $p = 30$ bar and a reaction mixture (in vol-%) = 5 % He, 75.72 % H_2 and 19.28 % CO_2. Only for Ni/SiO_2 shown in Figure 6.14c

The supported Ni nanoparticles after the stability test showed nanoparticles with a relatively narrow size distribution in Figure 6.14. Larger (> 20 nm) nanoparticles were only observed for the Ni/SiO_2 shown in Figure 6.14c, but these were rare. This illustrates the possibility of using these Ni nanoparticles prepared through colloidal methods for investigating CO_2 hydrogenation over Ni/C and Ni/SiO_2 catalysts at 300 °C. It should be noted that the Ni/SiO_2 catalysts which were tested at 340 °C showed much more significant sintering (shown in Figure 6.3b) than the same catalysts at 300 °C. A possible explanation might be that due to the higher conversions at the higher temperature of 340 °C compared to 300 °C and the exothermic nature of CO_2 hydrogenation, hot spots might form which induce more significant sintering. An additional observation which was made was that the Ni/C catalysts shown in Figure 6.14b and Figure 6.14a show similar particle diameters after catalysis, despite starting from 4 nm Ni seeds and 7 nm Ni nanoparticles. This illustrates that although differently sized Ni/C catalysts can be prepared and tested, studying potential influences of particle diameter on catalytic performance is much more complicated.

6.2 Conclusions

In this chapter, the catalytic performance in high pressure catalysis at a temperature range of 240 °C to 340 °C of several different Ni catalysts was described. These supported Ni catalysts were prepared with different supports, particle sizes and Ni wt-%. Ni/SiO_2 (Davisil 643) and Ni/C (GNP500) prepared through colloidal methods with several particle diameters and Ni wt-% were investigated and compared to conventional incipient wetness impregnation catalysts. In particular, it was shown that Ni/SiO_2 catalysts prepared with colloidal methods whilst using trioctylphosphine showed no CO_2 hydrogenation activity. This highlights the importance of developing phosphorous-free colloidal synthesis methods to study CO_2 methanation, like those discussed in this thesis.
The studied catalysts both showed significant particle growth after activity tests from 240 °C up to 340 °C. Ni/SiO_2 catalysts showed much higher CO_2 hydrogenation activity than their Ni/C counterparts, both at a constant 300 °C as well as over the range of 240 °C up to 340 °C. This might be explained through strong adsorption of CO_2 on SiO_2, which in turn can lead to higher activity [28]. The Ni/SiO_2 catalysts also experienced more significant sintering, which might be rationalised through the formation of more hot spots at high CO_2 conversions due to the exothermic nature of CO_2 methanation. In addition, the smaller surface area of the support material (300 vs 500 m^2/g for Davisil 643 vs GNP500) might also reduce the interparticle distance, which could lead to more sintering.
Ni/C catalysts prepared through incipient wetness impregnation showed significantly higher activity than colloidally prepared Ni/C catalysts despite having similar Ni wt-% and particle diameter. A potential effect which might cause this significant difference is doping of our Ni nanoparticles with boron during colloidal synthesis. This was not investigated in this thesis and literature suggests that boron is not incorporated in the Ni nanoparticles through the synthesis described in Section 2.1.2 [58]. The heat treatment used in this thesis also influenced the activity of the IWI:Ni/C catalysts. Calcination in O_2 at 250 °C appeared to decrease the IWI:Ni/C activity.
The supported Ni catalysts discussed here were also tested for stability at 300 °C. Here, Ni/SiO_2 again showed the highest average conversion, with the IWI:Ni/C catalysts in turn being higher than the colloidally prepared Ni/C catalysts. This stability test showed an additional promising result for the reproducibility of the colloidal preparation methods. The Ni/C catalysts with varying Ni wt-% but similar Ni particle diameters show very similar catalytic activities and CH_4 selectivity at similar conversions.
Finally, despite the attempt, it was found very difficult to determine the influence of Ni particle diameter on the catalytic performance in CO_2 hydrogenation. A major cause for this was the sintering that particles experienced. Particles supported on SiO_2 that started as 4 and 7 nm colloids ended up having either very polydisperse particle diameters and shapes, which made comparison very difficult. Particles supported on carbon that started as 4 and 7 nm colloids ended up having very similar particle sizes after catalysis, which made it difficult to elucidate size effects.
To summarize, we have demonstrated the possibility of testing a variety of Ni/SiO_2 and Ni/C catalysts prepared in a variety of ways and comparing these catalysts at a range of 240 to 340 °C at pressures of 30 bar.

6.3 Outlook

The catalytic results presented in this chapter are highly interesting starts of further research. Especially, the large difference noted in activity for Ni/SiO_2 and Ni/C catalysts highlights the potential influence support materials can have on the CO_2 hydrogenation reaction. For further research, the same Ni nanoparticles could be supported on different kinds of C and SiO_2. Using SiO_2 supports with larger surface areas might limit sintering by reducing interparticle distance. Entirely different supports, like CeO_2, ZrO_2 and TiO_2 might also be investigated to determine the influence the support can have on the catalytic performance. CeO_2 support material in particular might be very interesting, as some literature suggests using it as a support enhances CO_2 methanation [10,28,85,86].
A noticeable difference in CO_2 hydrogenation activity between the IWI:Ni/C and Ni/C catalysts prepared using colloidal methods was observed in this chapter, despite their similar sizes and shapes. A possible explanation could be the presence of boron in the colloidally prepared catalysts. This could be investigated by ICP-OES, although the literature procedure on which the synthesis was based claimed to not observe boron with elemental analyses [58]. The inactive Ni_xP_y catalyst still had defined particles after catalysis. Although, this catalysts was not active for CO_2 hydrogenation, they might be active for hydrodesulfurization reactions and could therefore be interesting to test for these reactions [87].
The studied systems attempted to compare Ni/C to Ni/SiO_2. However, the carbon present in the support material might also hydrogenate and form CH_4, especially in the presence of Ni. By preparing a range of Ni/C catalysts and testing them in high pressure H_2 without any CO_2 present, we might quantify this methanation of the support and more accurately compare the Ni/SiO_2 catalysts to the Ni/C catalysts.

Chapter 7

Conclusions & Outlook

This thesis aimed to develop and understand a method for using colloidal synthesis to Ni based catalyst for use in CO_2 hydrogenation to methane. This particular reaction is interesting for its potential to store solar and wind power in chemical bonds. However, gaining fundamental insight in this reaction requires the development of methods to be able to reliably synthesize various sizes of Ni NPs supported on different supports. In this thesis, a colloidal synthesis approach was applied to reproducibly synthesize 4.4 $\pm$ 0.7 nm and 6.5 $\pm$ 1.7 nm monodisperse Ni NPs, without resorting to the use of P-containing ligands. These distinct sizes of Ni NPs were deposited on 4 different supports, GNP500 C, Davisil 643 SiO_2, Aerosil 380V SiO_2 and SBa200 Al_2O_3. The used mild method for deposition was successful in maintaining the size and shape of the deposited nanoparticles across these supports. Dispersion of the nanoparticles across the support was not completely controlled, with some samples showing large empty areas or large amounts of aggregated NPs. Heat treatments used were successful in removing the majority of organic ligands present on the Ni NPs, however they also led to significant sintering for the samples with larger Ni wt-%, especially on Davisil 643 and SBa200.
Finally, catalytic performance of the catalyst was investigated in a high pressure catalysis setup from 240 to 340 °C, as well as a constant 300 °C. Here, it was found that Ni/Si_O2 catalysts performed significantly better than comparable Ni/C catalysts, which could be caused by the stronger adsorption of CO_2 to the SiO_2. Significant particle growth was observed for the Ni nanoparticles supported on SiO_2 post-catalysis. Particles supported on C also show some growth, although much less than those supported on SiO_2. This made comparison between activities and TOFs of catalysts with different particle sizes difficult.
Ni NPs synthesized using a phosphorous-free colloidal synthesis method performed much better than those synthesized with a TOP ligand, which were inactive. This supports the reasoning behind using phosphorous-free ligands for Ni NPs synthesis. Ni/C catalysts (with similar Ni particle diameter and wt-%) prepared using incipient wetness impregnation were also tested to investigate their performance to those Ni/C catalysts prepared through colloidal methods. The IWI:Ni/C catalysts performed better (higher conversions, higher activities and higher CH_4 selectivity) to their colloidally prepared counterparts, despite having similar Ni particle diameter and Ni wt-%.

In Chapters 3, 4 and 6, suggestions for follow-up research and optimization of the demonstrated methods are discussed. With respect to the main content of this thesis, the main focus of future continuation of this research should be to optimize the used synthesis methods to obtain monodisperse Ni NPs after reduction on different supports. The methods demonstrated already show the possibility to deposit similarly sized Ni colloids on different supports, and the next step should be to keep these particle sizes and shapes constant across different supports. Chemical removal of ligands might be an interesting approach to attain this, which would enable further research, investigating potential support effects of different supports like C, SiO_2, CeO_2, ZrO_2 and TiO_2. Modifying the colloidal synthesis by using different ligands and reducing agents could be interesting to obtain differently sized Ni NPs, which can be used to study Ni NP size effects in more detail.

Chapter 8

Acknowledgements

Over the course of nearly a year, I have had the great joy of working in the Materials Chemistry and Catalysis group. It should be more than clear that the work presented here would not have been possible without the people that make up this group. In addition to this, and for the great atmosphere that I personally experienced, I would like to thank the entire group. Some people deserve special acknowledgements which is done below in no particular order:

I would like to thank all of the master and bachelor students that currently are or were present during my time at MCC. Their incredible talent in quickly switching from serious business to slightly less serious business helped me a lot during my thesis and made me enjoy counting particles significantly more.
I would like to thank Dennie Wezendonk, Laura Barberis, Johan de Boed and Yannick Geertzema for their training so that I could use the XRD, TPR, the centrifuge and the ATR-IR on my own.
I would like to thank the physisorption team and Dennie Wezendonk for the measurements they performed for me.
I would like to thank Suzan Schoemaker and Oscar Brandt Corstius for supervising me during Nienke & Oscar Daoura's absence.
I would like to thank all technicians for helping to provide a safe working environment.
I would like to thank Remco Dalebout & Jan Willem de Rijk for their help and input with the Flowrence.
I would like to thank Petra de Jongh for taking the time to examine my thesis, give input on my abstract(s) and poster and of course for the opportunity to work on this thesis at MCC.
I would like to thank Jessi van der Hoeven for examining my thesis, providing input on my abstract(s) and poster, for her input during the project on a variety of things and for having me as a student. I am really happy with the input you gave me and it helped especially in focusing my research.
Finally, I want to thank two people in particular. First, I would like to thank Oscar Daoura, for teaching me an incredible amount of things concerning colloidal synthesis, helping me build a small set-up for this colloidal synthesis and for also giving me advice on how to perform several experiments. I am also very grateful for your involvement and the fact you were still more than happy to give me feedback and input on the project after accepting your new job. You were always very interested in what kind of experiment I was performing and your enthusiasm in discussing potential creative solutions to both our colloidal problems was a welcome distraction from looking at a thermocouple to see whether it would stabilize or not.
Last, but certainly not least, I would like to thank Nienke Visser. As my daily supervisor, you certainly taught me a lot of different things in and outside of the lab. In particular, I would like to thank you for the opportunity to perform an *in situ* TEM experiment together, which was a really motivating and amazing experiment. In addition, we have spent quite some time looking at nanoparticles in the in the EM center, for which I would also like to thank you. Considering things outside of the lab, I would like to thank you for being patient with me ranting on and on about results, whilst at the same time giving me feedback and ideas on how to continue. I think your comments really helped me develop in presenting results in a more clear and concise manner. Finally, I am really happy about the way you approached teaching me things, which primarily allowed me to figure it out with you sometimes interjecting to point me in the right direction.
To conclude, I would also like to thank everyone else of the MCC group again, for helping me, working with me and enjoying all the external activities that could be organised.

Chapter 9

Layman's Abstract

The modern world as we know it currently relies on many different chemical processes to provide the materials we need. From the production of fuels and plastics to the creation of food and medical substances, chemistry is indispensable for our modern lives. A typical chemical process can be described as a conversion of certain substances into other substances. In many cases, these conversions require some form of energy to occur. Typically, this energy is provided as heat, similar to the cooking of food. However, some reactions require very high temperatures to operate at sufficient rates to be interesting for industrial appliances. This is where a certain class of materials enter the picture; 'the heterogeneous catalyst'. A catalyst is a material that helps certain chemical conversions occur more rapidly and selectively. This allows us to perform our reactions at much lower temperatures and still end up with the same production rates. The word heterogeneous indicates that the catalysts is in a different phase than the reactants are. Typically, the catalysts is a solid (a powder or a perhaps a porous gel) and the reactants are liquids or gases. These reactants are flowed over the catalysts, typically reacting on their surfaces and yielding our products. Heterogeneous catalysts widely used, and without them, our modern world would not exists as we know it. However, preparing these heterogeneous catalysts is not that straightforward and understanding the preparation of a specific type of heterogeneous catalyst is the main objective of this thesis.

Contemporary heterogeneous catalysts typically consist of two parts: 1) a metal (nickel, iron and copper, or more expensive metals like palladium, platinum and gold) and 2) a support material. These support materials are typically very stable chemicals, that can withstand high temperatures and pressures without changing much. The surface of the metal present in catalysts is typically the active site, the place where reactants form their products. A key nuance here is the mention of the metal surface. Typically, we would like to use as little metal as possible (as many used metals are expensive), whilst having as large a surface area as we can (to maximize reaction speed). To this end, catalysts typically consist of metallic nanoparticles supported on the stable materials we discussed before. Nanoparticles are very small particles, typically in the 3-20 nm range. Shown in Figure 9.1 is a schematic overview of why nanoparticles give us a large surface area, whilst keeping the used metal low. In this image, we can see that as the particle size increases, its surface and volume also increase. However, relative to the surface, volume increases faster. Thus, larger particles have a smaller surface relative to their volume when compared with smaller particles. Or, as seen in the image, a particle with a size of 2 cm has a surface-to-volume ratio of 3 cm^{-1} and a particle with a size of 3 cm has a surface-to-volume ratio of 2 cm^{-1}. Thus, smaller particles need less metal to obtain the same surface area as larger particles would. There is another key nuance that should be mentioned here. Although small metal particles have a larger surface-to-volume ratio, their size starts to influence reactions in their own way and sometimes larger particles might actually perform better by enabling more favourable reaction mechanisms. Therefore, controlling the size of these small particles is very important to prepare suitable catalysts.

The synthesis of very small (3-20 nm) metal particles is quite challenging. Many methods exist, each with their own advantages and disadvantages. A promising method described in more detail in this thesis is known as colloidal synthesis. Basically, a colloid is a solid particle floating in a liquid. These colloids are typically stabilized in this solution by something that is known as a ligand. A ligand binds to our metal and suspends it in a liquid. These particles can then be placed on a support material by placing the support material into

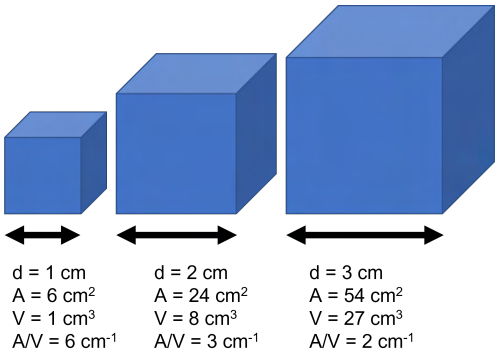

Figure 9.1: Schematic overview of the surface to volume ratio effect in particles. Here d is the size of an edge, A is the total surface area of the cube, V is the volume of the cube and A/V is the surface-to-volume ratio.

a suspension of colloids and evaporating the liquid in which the colloids are floating. This is what this thesis focussed on, making these colloids and placing them on a support material.

These supported nanoparticles can with the conversion of 'waste' molecules, like carbon dioxide (CO_2). This greenhouse gas is typically seen as something useless, however, it need not be. It is possible to convert CO_2 into something that we all use, like methane (CH_4). This chemical conversion is catalysed by metallic nickel (Ni). Thus, taking into account the discussed effect of particle sizes on metal surface area, this thesis focussed on preparation of small Ni nanoparticles for the methanation of CO_2. First, the goal of this thesis was to obtain Ni colloids of various sizes without using a certain ligand. This ligand, known as trioctylphosphine (TOP)), contains a certain chemical element, phosphorous (P), which allows it to stabilize metal colloids quite well. However, in the case of Ni, it also means that this element can incorporate itself into our Ni nanoparticle. In this thesis, we demonstrated that this incorporation of P can deactivate our catalysts, making them ineffective. In this thesis, it was demonstrated that we could reliably synthesize two distinct sizes of Ni nanoparticles, 4 and 7 nm in size (a nm is 1*10$^-$9 m).

The second goal of this thesis was to place these Ni colloids on different types of support materials, so we could study the preparation of different types of catalysts. Some materials show better thermal stability, like silica, and can help with catalysis by adsorbing CO_2. Other supports, like carbon, allow for more fundamental research into the process itself, because they are said to have a more limited interaction with the catalytic reaction. In this way, we would only study the effect of the Ni nanoparticles, and not an additional effect introduced by the support material, on CO_2 methanation. It was demonstrated that our Ni colloids could be placed on different supports whilst maintaining their size and shape. These Ni nanoparticles supported on these materials are however covered in the ligands that we used to make them, organic molecules that might hinder or influence catalysis. These need to be removed, which is done by heating our catalysts in oxygen or hydrogen. This in turn can change our particles, typically resulting in particle growth.

Finally, our catalysts are tested in realistic reaction conditions. This means we flow a mixture of hydrogen and carbon dioxide over our catalyst materials at elevated pressure (30 bar, which is almost 30 times the pressure our atmosphere exerts on us) and temperature (240-340 °C). We then measure the outflow of CH_4 and CO_2 to see how much of what we put in is actually converted to our desired product. In this work, it was shown that catalysts prepared with TOP were not active catalysts, whereas catalysts prepared without top were. A large difference in activity for Ni nanoparticles supported on silica (more active) vs Ni nanoparticles supported on carbon (less active) was also observed, which gives us insight in what improves the CO_2 methanation reaction.

To summarize, a schematic overview of this thesis is given in Figure 9.2. First, we could make phosphorous-free Ni colloids of different sizes. Then, we could place these Ni nanoparticle colloids on different supports and maintain their size. Then we demonstrated the possibility of removing these ligands in their entirety.

Finally, we could show the different effects of support materials as well as ligand choice on catalysis, helping us understand the ins and outs of CO_2 methanation.

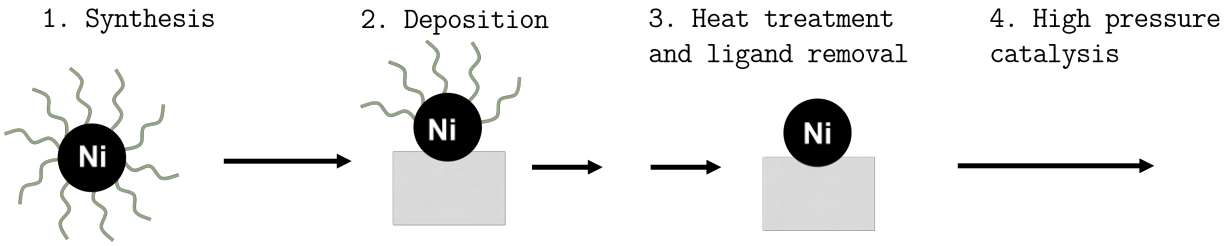

Figure 9.2: An schematic overview of the work presented in this thesis. It consists of four distinct parts; 1) Colloidal synthesis, 2) Deposition of colloids, 3) Removal of ligands and activation of prepared precatalysts and finally 4) high pressure catalysis.

Bibliography

[1] C. Vogt, E. Groeneveld, G. Kamsma, M. Nachtegaal, L. Lu, C. J. Kiely, P. H. Berben, F. Meirer, and B.M. Weckhuysen. Unravelling structure sensitivity in CO2 hydrogenation over nickel. *Nature Catalysis*, 1(2):127–134, feb 2018.

[2] P. Munnik, P. E. de Jongh, and K. P. de Jong. Recent Developments in the Synthesis of Supported Catalysts. *Chemical Reviews*, 115(14):6687–6718, jul 2015.

[3] W. L. Vrijburg, J.W. A. van Helden, A. J. F. van Hoof, H. Friedrich, E. Groeneveld, E. A. Pidko, and E. J. M. Hensen. Tunable colloidal Ni nanoparticles confined and redistributed in mesoporous silica for CO 2 methanation. *Catalysis Science & Technology*, 9(10):2578–2591, 2019.

[4] J. N. Armor. A history of industrial catalysis. *Catalysis Today*, 163(1):3–9, apr 2011.

[5] I. Chorkendorff and J. W. Niemantsverdriet. *Concepts of Modern Catalysis and Kinetics*. Wiley, oct 2003.

[6] M. Götz, J. Lefebvre, F. Mörs, A. McDaniel Koch, F. Graf, S. Bajohr, R. Reimert, and T. Kolb. Renewable Power-to-Gas: A technological and economic review. *Renewable Energy*, 85:1371–1390, jan 2016.

[7] G. Centi and S. Perathoner. Opportunities and prospects in the chemical recycling of carbon dioxide to fuels. *Catalysis Today*, 148(3-4):191–205, nov 2009.

[8] P. Panagiotopoulou and X. E. Verykios. Mechanistic Study of the Selective Methanation of CO over Ru/TiO 2 Catalysts: Effect of Metal Crystallite Size on the Nature of Active Surface Species and Reaction Pathways. *The Journal of Physical Chemistry C*, 121(9):5058–5068, mar 2017.

[9] A. Petala and P. Panagiotopoulou. Methanation of CO2 over alkali-promoted Ru/TiO2 catalysts: I. Effect of alkali additives on catalytic activity and selectivity. *Applied Catalysis B: Environmental*, 224:919–927, may 2018.

[10] R.-P. Ye, Q. Li, W. Gong, T. Wang, J. J. Razink, L. Lin, Y.-Y. Qin, Z. Zhou, H. Adidharma, J. Tang, A. G. Russell, M. Fan, and Y.-G. Yao. High-performance of nanostructured Ni/CeO2 catalyst on CO2 methanation. *Applied Catalysis B: Environmental*, 268:118474, jul 2020.

[11] Q. Pan, J. Peng, T. Sun, S. Wang, and S. Wang. Insight into the reaction route of CO2 methanation: Promotion effect of medium basic sites. *Catalysis Communications*, 45:74–78, feb 2014.

[12] C. Italiano, J. Llorca, L. Pino, M. Ferraro, V. Antonucci, and A. Vita. CO and CO2 methanation over Ni catalysts supported on CeO2, Al2O3 and Y2O3 oxides. *Applied Catalysis B: Environmental*, 264:118494, may 2020.

[13] S. Rönsch, J. Schneider, S. Matthischke, M. Schlüter, M. Götz, J. Lefebvre, P. Prabhakaran, and S. Bajohr. Review on methanation – From fundamentals to current projects. *Fuel*, 166:276–296, feb 2016.

[14] P. Frontera, A. Macario, M. Ferraro, and P. Antonucci. Supported Catalysts for CO2 Methanation: A Review. *Catalysts*, 7(12):59, feb 2017.

[15] H. C. Wu, Y. C. Chang, J. H. Wu, J. H. Lin, I. K. Lin, and C. S. Chen. Methanation of CO 2 and reverse water gas shift reactions on Ni/SiO 2 catalysts: the influence of particle size on selectivity and reaction pathway. *Catalysis Science & Technology*, 5(8):4154–4163, 2015.

[16] C. Heine, B. A. J. Lechner, H. Bluhm, and M. Salmeron. Recycling of CO 2 : Probing the Chemical State of the Ni(111) Surface during the Methanation Reaction with Ambient-Pressure X-Ray Photoelectron Spectroscopy. *Journal of the American Chemical Society*, 138(40):13246–13252, oct 2016.

[17] M.-H. Liu, H.A. Chen, C.-S. Chen, J.-H. Wu, H.-C. Wu, and C. M. Yang. Tiny Ni particles dispersed in platelet SBA-15 materials induce high efficiency for CO 2 methanation. *Nanoscale*, 11(43):20741–20753, 2019.

[18] C.-S. Chen, C. S. Budi, H.-C. Wu, D. Saikia, and H.-M. Kao. Size-Tunable Ni Nanoparticles Supported on Surface-Modified, Cage-Type Mesoporous Silica as Highly Active Catalysts for CO 2 Hydrogenation. *ACS Catalysis*, 7(12):8367–8381, dec 2017.

[19] B. Miao, S. S. K. Ma, X. Wang, H. Su, and S. H. Chan. Catalysis mechanisms of CO 2 and CO methanation. *Catalysis Science & Technology*, 6(12):4048–4058, 2016.

[20] P.A. U. Aldana, F. Ocampo, K. Kobl, B. Louis, F. Thibault-Starzyk, M. Daturi, P. Bazin, S. Thomas, and A.C. Roger. Catalytic CO2 valorization into CH4 on Ni-based ceria-zirconia. Reaction mechanism by operando IR spectroscopy. *Catalysis Today*, 215:201–207, oct 2013.

[21] S. Fujita, H. Terunuma, M. Nakamura, and N. Takezawa. Mechanisms of methanation of carbon monoxide and carbon dioxide over nickel. *Industrial & Engineering Chemistry Research*, 30(6):1146–1151, jun 1991.

[22] S.-i. Fujita, M. Nakamura, T. Doi, and N. Takezawa. Mechanisms of methanation of carbon dioxide and carbon monoxide over nickel/alumina catalysts. *Applied Catalysis A: General*, 104(1):87–100, oct 1993.

[23] L. Lin, C. A. Gerlak, C. Liu, J. Llorca, S. Yao, N. Rui, F. Zhang, Z. Liu, S. Zhang, K. Deng, C. B. Murray, J. A. Rodriguez, and S. D. Senanayake. Effect of Ni particle size on the production of renewable methane from CO2 over Ni/CeO2 catalyst. *Journal of Energy Chemistry*, 61:602–611, oct 2021.

[24] M. Li, H. Amari, and A. C. van Veen. Metal-oxide interaction enhanced CO2 activation in methanation over ceria supported nickel nanocrystallites. *Applied Catalysis B: Environmental*, 239:27–35, dec 2018.

[25] C. de Mello Donegá, editor. *Nanoparticles: Workhorses of Nanoscience*. Springer Berlin Heidelberg, Berlin, Heidelberg, 2014.

[26] S. Carenco, C. Boissiere, L. Nicole, C. Sanchez, P. Le Floch, and N. Mezailles. Controlled Design of Size-Tunable Monodisperse Nickel Nanoparticles. *Chemistry of Materials*, 22(4):1340–1349, feb 2010.

[27] L. M. Moreau, D.-H. Ha, C. R. Bealing, H. Zhang, R. G. Hennig, and R. D. Robinson. Unintended Phosphorus Doping of Nickel Nanoparticles during Synthesis with TOP: A Discovery through Structural Analysis. *Nano Letters*, 12(9):4530–4539, sep 2012.

[28] A. Jangam, S. Das, N. Dewangan, P. Hongmanorom, W. M. Hui, and S. Kawi. Conversion of CO2 to C1 chemicals: Catalyst design, kinetics and mechanism aspects of the reactions. *Catalysis Today*, 358:3–29, dec 2020.

[29] W. Wei and G. Jinlong. Methanation of carbon dioxide: an overview. *Frontiers of Chemical Science and Engineering*, 5(1):2–10, mar 2011.

[30] A. Cárdenas-Arenas, A. Quindimil, A. Davó-Quiñonero, E. Bailón-García, D. Lozano-Castelló, U. De-La-Torre, B. Pereda-Ayo, J.A. González-Marcos, J.R. González-Velasco, and A. Bueno-López. Isotopic and in situ DRIFTS study of the CO2 methanation mechanism using Ni/CeO2 and Ni/Al2O3 catalysts. *Applied Catalysis B: Environmental*, 265:118538, may 2020.

[31] J. Ilsemann, M. M. Murshed, T. M. Gesing, J. Kopyscinski, and M. Bäumer. On the support dependency of the CO 2 methanation – decoupling size and support effects. *Catalysis Science & Technology*, 11(12):4098–4114, 2021.

[32] J. Martínez, E. Hernández, S. Alfaro, R. López Medina, G. Valverde Aguilar, E. Albiter, and M. Valenzuela. High Selectivity and Stability of Nickel Catalysts for CO2 Methanation: Support Effects. *Catalysts*, 9(1):24, dec 2018.

[33] S. M. Lee, Y. H. Lee, D. H. Moon, J. Y. Ahn, Di. D. Nguyen, S. W. Chang, and S. S. Kim. Reaction Mechanism and Catalytic Impact of Ni/CeO 2– x Catalyst for Low-Temperature CO 2 Methanation. *Industrial & Engineering Chemistry Research*, 58(20):8656–8662, may 2019.

[34] A. Westermann, B. Azambre, M.C. Bacariza, I. Graça, M.F. Ribeiro, J.M. Lopes, and C. Henriques. Insight into CO2 methanation mechanism over NiUSY zeolites: An operando IR study. *Applied Catalysis B: Environmental*, 174-175:120–125, sep 2015.

[35] C. Liang, L. Zhang, Y. Zheng, S. Zhang, Q. Liu, G. Gao, D. Dong, Y. Wang, L. Xu, and X. Hu. Methanation of CO2 over nickel catalysts: Impacts of acidic/basic sites on formation of the reaction intermediates. *Fuel*, 262:116521, feb 2020.

[36] J. K. Kesavan, I. Luisetto, S. Tuti, C. Meneghini, G. Iucci, C. Battocchio, S. Mobilio, S. Casciardi, and R. Sisto. Nickel supported on YSZ: The effect of Ni particle size on the catalytic activity for CO2 methanation. *Journal of CO2 Utilization*, 23:200–211, jan 2018.

[37] D. Beierlein, D. Häussermann, M. Pfeifer, T. Schwarz, K. Stöwe, Y. Traa, and E. Klemm. Is the CO2 methanation on highly loaded Ni-Al2O3 catalysts really structure-sensitive? *Applied Catalysis B: Environmental*, 247:200–219, jun 2019.

[38] S. Sahebdelfar and M. Takht Ravanchi. Carbon dioxide utilization for methane production: A thermodynamic analysis. *Journal of Petroleum Science and Engineering*, 134:14–22, oct 2015.

[39] J. Gao, Y. Wang, Y. Ping, D. Hu, G. Xu, F. Gu, and F. Su. A thermodynamic analysis of methanation reactions of carbon oxides for the production of synthetic natural gas. *RSC Advances*, 2(6):2358, 2012.

[40] D. Schmider, L. Maier, and O. Deutschmann. Reaction Kinetics of CO and CO 2 Methanation over Nickel. *Industrial & Engineering Chemistry Research*, 60(16):5792–5805, apr 2021.

[41] C. V. Miguel, A. Mendes, and L. M. Madeira. Intrinsic kinetics of CO2 methanation over an industrial nickel-based catalyst. *Journal of CO2 Utilization*, 25:128–136, may 2018.

[42] M. A. Vannice. The Catalytic Synthesis of Hydrocarbons from Carbon Monoxide and Hydrogen. *Catalysis Reviews*, 14(1):153–191, jan 1976.

[43] G. A. Mills and F. W. Steffgen. Catalytic Methanation. *Catalysis Reviews*, 8(1):159–210, jan 1974.

[44] J. Gao, Q. Liu, F. Gu, B. Liu, Z. Zhong, and F. Su. Recent advances in methanation catalysts for the production of synthetic natural gas. *RSC Advances*, 5(29):22759–22776, 2015.

[45] G.D. Lee, M. J. Moon, J. H. Park, S. S. Park, and S. S. Hong. Raney Ni catalysts derived from different alloy precursors Part II. CO and CO2 methanation activity. *Korean Journal of Chemical Engineering*, 22(4):541–546, jul 2005.

[46] X. Gao, H. Liu, K. Hidajat, and S. Kawi. Anti-Coking Ni/SiO 2 Catalyst for Dry Reforming of Methane: Role of Oleylamine/Oleic Acid Organic Pair. *ChemCatChem*, 7(24):4188–4196, dec 2015.

[47] Y. Liu, L. Zhu, X. Wang, S. Yin, F. Leng, F. Zhang, H. Lin, and S. Wang. Catalytic methanation of syngas over Ni-based catalysts with different supports. *Chinese Journal of Chemical Engineering*, 25(5):602–608, may 2017.

[48] L. P. L. Gonçalves, J. P. S. Sousa, O. S. G. P. Soares, O. Bondarchuk, O. I. Lebedev, Y. V. Kolen'ko, and M. F. R. Pereira. The role of surface properties in CO 2 methanation over carbon-supported Ni catalysts and their promotion by Fe. *Catalysis Science & Technology*, 10(21):7217–7225, 2020.

[49] W. Zhen, B. Li, G. Lu, and J. Ma. Enhancing catalytic activity and stability for CO 2 methanation on Ni@MOF-5 via control of active species dispersion. *Chemical Communications*, 51(9):1728–1731, 2015.

[50] J. L. Figueiredo. Functionalization of porous carbons for catalytic applications. *Journal of Materials Chemistry A*, 1(33):9351, 2013.

[51] J. L. Figueiredo and M. F.R. Pereira. The role of surface chemistry in catalysis with carbons. *Catalysis Today*, 150(1-2):2–7, feb 2010.

[52] F. Rodriguez-Reinoso and A. Sepulveda-Escribano. Carbon as Catalyst Support. In *Carbon Materials for Catalysis*, pages 131–155. John Wiley & Sons, Inc., Hoboken, NJ, USA, apr 2008.

[53] P. Paalanen, M. Rivera Torrente, R. Dalebout, J. Wijten, and M. Versluijs-Helder. GNP500Informationsheet.

[54] A. R. Tao, S. Habas, and P. Yang. Shape Control of Colloidal Metal Nanocrystals. *Small*, 4(3):310–325, mar 2008.

[55] C.-J. Jia and F. Schüth. Colloidal metal nanoparticles as a component of designed catalyst. *Physical Chemistry Chemical Physics*, 13(7):2457, 2011.

[56] A.F. Gross, M. R. Diehl, K. C. Beverly, E. K. Richman, and S. H. Tolbert. Controlling Magnetic Coupling between Cobalt Nanoparticles through Nanoscale Confinement in Hexagonal Mesoporous Silica. *The Journal of Physical Chemistry B*, 107(23):5475–5482, jun 2003.

[57] N. Hondow and R. O. Fuller. The use of preformed nanoparticles in the production of heterogeneous catalysts. *Journal of Colloid and Interface Science*, 417:396–401, mar 2014.

[58] Ö. Metin, V. Mazumder, S. Özkar, and S. Sun. Monodisperse Nickel Nanoparticles and Their Catalysis in Hydrolytic Dehydrogenation of Ammonia Borane. *Journal of the American Chemical Society*, 132(5):1468–1469, feb 2010.

[59] V. Tzitzios, G. Basina, M. Gjoka, V. Alexandrakis, V. Georgakilas, D. Niarchos, N. Boukos, and D. Petridis. Chemical synthesis and characterization of hcp Ni nanoparticles. *Nanotechnology*, 17(15):3750–3755, aug 2006.

[60] E. Zacharaki, P. Beato, R. R. Tiruvalam, K. J. Andersson, H. Fjellvåg, and A. O. Sjåstad. From Colloidal Monodisperse Nickel Nanoparticles to Well-Defined Ni/Al 2 O 3 Model Catalysts. *Langmuir*, 33(38):9836–9843, sep 2017.

[61] G. G. Couto, J. J. Klein, W. H. Schreiner, D. H. Mosca, A. J.A. de Oliveira, and A.J.G. Zarbin. Nickel nanoparticles obtained by a modified polyol process: Synthesis, characterization, and magnetic properties. *Journal of Colloid and Interface Science*, 311(2):461–468, jul 2007.

[62] L. M. Rossi, J. L. Fiorio, M. A. S. Garcia, and C.P. Ferraz. The role and fate of capping ligands in colloidally prepared metal nanoparticle catalysts. *Dalton Transactions*, 47(17):5889–5915, 2018.

[63] T. S. Rodrigues, M. Zhao, T.-H. Yang, K. D. Gilroy, A. G. M. da Silva, P. H. C. Camargo, and Y. Xia. Synthesis of Colloidal Metal Nanocrystals: A Comprehensive Review on the Reductants. *Chemistry – A European Journal*, 24(64):16944–16963, nov 2018.

[64] A. Heuer-Jungemann, N. Feliu, I. Bakaimi, M. Hamaly, A. Alkilany, I. Chakraborty, A. Masood, M. F. Casula, A. Kostopoulou, E. Oh, K. Susumu, M.H. Stewart, I. L. Medintz, E. Stratakis, W.J. Parak, and A.G. Kanaras. The Role of Ligands in the Chemical Synthesis and Applications of Inorganic Nanoparticles. *Chemical Reviews*, 119(8):4819–4880, apr 2019.

[65] J. W. Han, J. S. Park, M. S. Choi, and H. Lee. Uncoupling the size and support effects of Ni catalysts for dry reforming of methane. *Applied Catalysis B: Environmental*, 203:625–632, apr 2017.

[66] Y. Pan, R. Jia, J. Zhao, J. Liang, Y. Liu, and C. Liu. Size-controlled synthesis of monodisperse nickel nanoparticles and investigation of their magnetic and catalytic properties. *Applied Surface Science*, 316:276–285, oct 2014.

[67] J. Park, E. Kang, S. U. Son, H.Mi. Park, M. K. Lee, J. Kim, K. W. Kim, H. J. Noh, J. H. Park, C. J. Bae, J. G. Park, and T. Hyeon. Monodisperse nanoparticles of Ni and NiO: Synthesis, characterization, self-assembled superlattices, and catalytic applications in the suzuki coupling reaction. *Advanced Materials*, 17(4):429–434, feb 2005.

[68] H. Winnischofer, T. C. R. Rocha, W. C. Nunes, L. M. Socolovsky, M. Knobel, and D. Zanchet. Chemical Synthesis and Structural Characterization of Highly Disordered Ni Colloidal Nanoparticles. *ACS Nano*, 2(6):1313–1319, jun 2008.

[69] R. Rinaldi, A. M. Porcari, T. C.R. Rocha, W. H. Cassinelli, R. U. Ribeiro, J. M. C. Bueno, and D. Zanchet. Construction of heterogeneous Ni catalysts from supports and colloidal nanoparticles – A challenging puzzle. *Journal of Molecular Catalysis A: Chemical*, 301(1-2):11–17, mar 2009.

[70] E. Ramírez-Meneses, I. Betancourt, F. Morales, V. Montiel-Palma, C. C. Villanueva-Alvarado, and M. E. Hernández-Rojas. Superparamagnetic nickel nanoparticles obtained by an organometallic approach. *Journal of Nanoparticle Research*, 13(1):365–374, jan 2011.

[71] S.-H. Wu and D.-H. Chen. Synthesis and characterization of nickel nanoparticles by hydrazine reduction in ethylene glycol. *Journal of Colloid and Interface Science*, 259(2):282–286, mar 2003.

[72] N. Dimitratos, J. A. Lopez-Sanchez, J. M. Anthonykutty, G. Brett, A. F. Carley, R. C. Tiruvalam, A. A. Herzing, C. J. Kiely, D. W. Knight, and Graham J. Hutchings. Oxidation of glycerol using gold–palladium alloy-supported nanocrystals. *Physical Chemistry Chemical Physics*, 11(25):4952, 2009.

[73] I. Lee, R. Morales, M. A. Albiter, and F. Zaera. Synthesis of heterogeneous catalysts with well shaped platinum particles to control reaction selectivity. *Proceedings of the National Academy of Sciences*, 105(40):15241–15246, oct 2008.

[74] M. Comotti, W.-C. Li, B. Spliethoff, and F. Schüth. Support Effect in High Activity Gold Catalysts for CO Oxidation. *Journal of the American Chemical Society*, 128(3):917–924, jan 2006.

[75] M. Casavola, J. Hermannsdörfer, N. de Jonge, A. I. Dugulan, and K. P. de Jong. Fabrication of Fischer-Tropsch Catalysts by Deposition of Iron Nanocrystals on Carbon Nanotubes. *Advanced Functional Materials*, 25(33):5309–5319, sep 2015.

[76] A. Y. Yang and M. Law. Uniform Supported Metal Nanocrystal Catalysts Prepared by Slurry Freeze-Drying. *Chemistry of Materials*, 33(1):256–265, jan 2021.

[77] P. Sonström and M. Bäumer. Supported colloidal nanoparticles in heterogeneous gas phase catalysis: on the way to tailored catalysts. *Physical Chemistry Chemical Physics*, 13(43):19270, 2011.

[78] D. Li, C. Wang, D. Tripkovic, S. Sun, N. M. Markovic, and V. R. Stamenkovic. Surfactant Removal for Colloidal Nanoparticles from Solution Synthesis: The Effect on Catalytic Performance. *ACS Catalysis*, 2(7):1358–1362, jul 2012.

[79] L. Lu, S. Zou, and B. Fang. The Critical Impacts of Ligands on Heterogeneous Nanocatalysis: A Review. *ACS Catalysis*, 11(10):6020–6058, may 2021.

[80] J. A. Lopez-Sanchez, N. Dimitratos, C. Hammond, G. L. Brett, L. Kesavan, S. White, P. Miedziak, R. Tiruvalam, R. L. Jenkins, A. F. Carley, D. Knight, C. J. Kiely, and G.J. Hutchings. Facile removal of stabilizer-ligands from supported gold nanoparticles. *Nature Chemistry*, 3(7):551–556, jul 2011.

[81] Q. Fan, K. Liu, Z. Liu, H. Liu, L. Zhang, P. Zhong, and C. Gao. A Ligand-Exchange Route to Nobel Metal Nanocrystals with a Clean Surface for Enhanced Optical and Catalytic Properties. *Particle & Particle Systems Characterization*, 34(8):1700075, aug 2017.

[82] R. Nakamura, J.-G. Lee, H. Mori, and H. Nakajima. Oxidation behaviour of Ni nanoparticles and formation process of hollow NiO. *Philosophical Magazine*, 88(2):257–264, jan 2008.

[83] J. G. Railsback, A. C. Johnston-Peck, J. Wang, and J. B. Tracy. Size-Dependent Nanoscale Kirkendall Effect During the Oxidation of Nickel Nanoparticles. *ACS Nano*, 4(4):1913–1920, apr 2010.

[84] J. A. Medford, A. C. Johnston-Peck, and J. B. Tracy. Nanostructural transformations during the reduction of hollow and porous nickel oxide nanoparticles. *Nanoscale*, 5(1):155–159, 2013.

[85] S. Tada, T. Shimizu, H. Kameyama, T. Haneda, and R. Kikuchi. Ni/CeO2 catalysts with high CO2 methanation activity and high CH4 selectivity at low temperatures. *International Journal of Hydrogen Energy*, 37(7):5527–5531, apr 2012.

[86] T. Das and G. Deo. Effects of metal loading and support for supported cobalt catalyst. *Catalysis Today*, 198(1):116–124, dec 2012.

[87] G. H. Layan Savithra, E. Muthuswamy, R. H. Bowker, B. A. Carrillo, M. E. Bussell, and S. L. Brock. Rational Design of Nickel Phosphide Hydrodesulfurization Catalysts: Controlling Particle Size and Preventing Sintering. *Chemistry of Materials*, 25(6):825–833, mar 2013.

Appendices

Appendix A

Figures

List of Figures

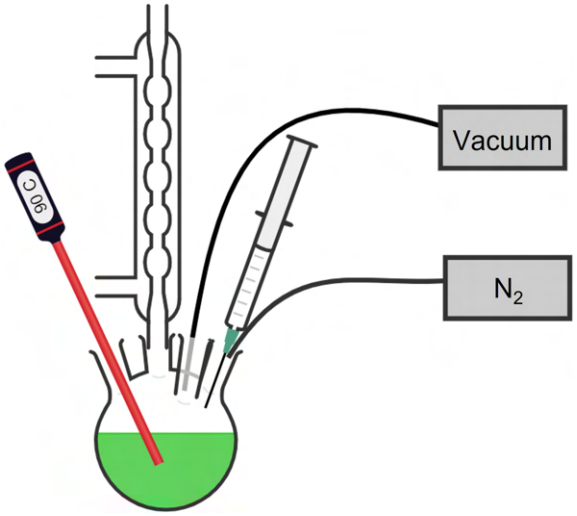

Figure A.1: Schematic overview of the setup used for hot-injection and heating-up methods.

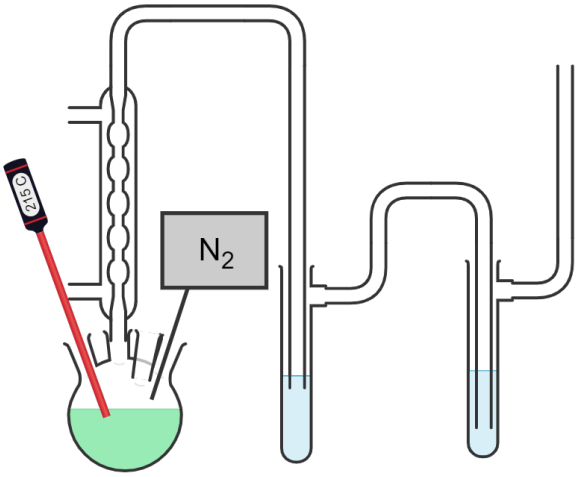

Figure A.2: Schematic overview of the setup used for the polyol synthesis.

Table A.1: Overview of physisorption experiments of support materials with and without nickel after calcination at 250 °C and reduction at 350 °C.

Support material	BET surface area (m^2/g)
Davisil 643	294
GNP500	503
Aerosil 380V	363
SBa200	185
Ni/Davisil 643	294
Ni/GNP500	436

Figure A.3: Photograph of the setup used for heat treatments under N_2, O_2 and H_2.

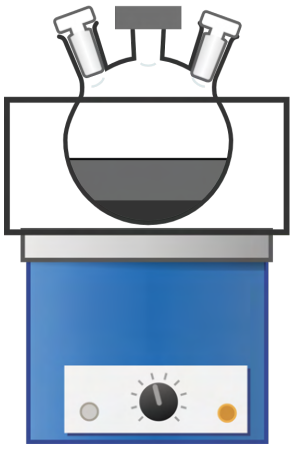

Figure A.4: Schematic overview of the setup used.

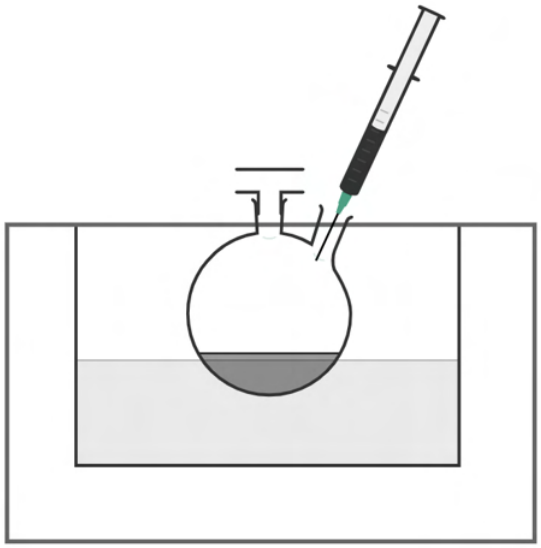

Figure A.5: Schematic overview of the setup used.

Figure A.6: Reactor used for calcination and reduction experiments

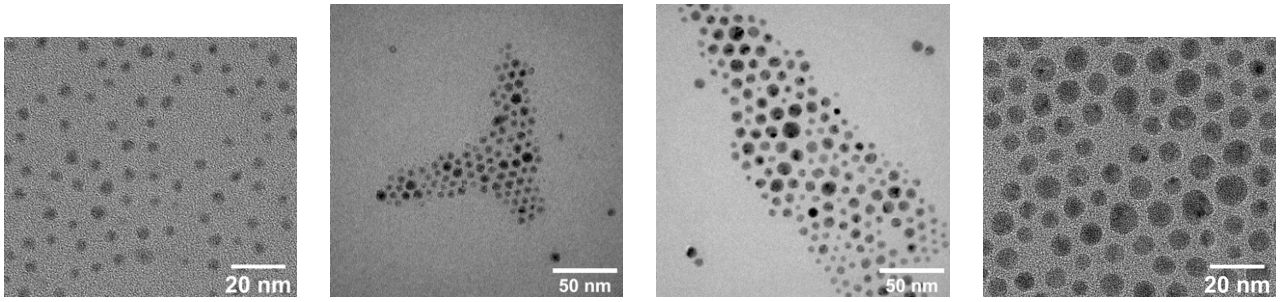

(a) TEM image of Ni nanoparticles with a mean particle diameter of 4.5 ± 1.2 nm. Concentration of $Ni(acac)_2$ was 0.050 mmol/L. Figure A.8a shows the corresponding size distribution.

(b) TEM image of Ni nanoparticles with a mean particle diameter of 4.7 ± 1.7 nm. Concentration of $Ni(acac)_2$ was 0.066 mmol/L. Figure A.8b shows the corresponding size distribution.

(c) TEM image of Ni nanoparticles with a mean particle diameter of 6.5 ± 2 nm. Concentration of $Ni(acac)_2$ was 0.1 mmol/L. Figure A.8c shows the corresponding size distribution.

(d) TEM image of Ni nanoparticles with a mean particle diameter of 6.5 ± 1.7 nm. Concentration of $Ni(acac)_2$ was 0.1 mmol/L. Figure A.8d shows the corresponding size distribution.

Figure A.7: TEM images of various Ni colloids synthesized by varying $Ni(acac)_2$ concentration in the growth solution.

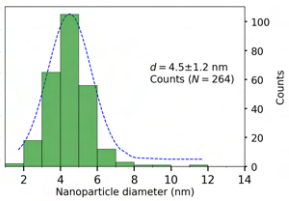

(a) Size distribution of Ni nanoparticles with a mean particle diameter of 4.5 ± 1.2 nm. Concentration of $Ni(acac)_2$ was 0.050 mmol/L.

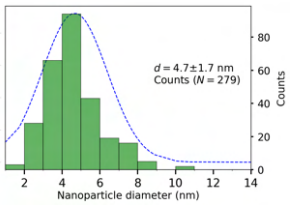

(b) Size distribution of Ni nanoparticles with a mean particle diameter of 4.7 ± 1.7 nm. Concentration of $Ni(acac)_2$ was 0.066 mmol/L.

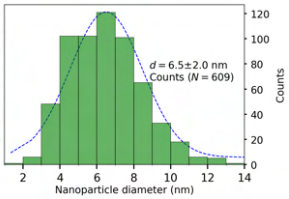

(c) Size distribution of Ni nanoparticles with a mean particle diameter of 6.5 ± 2 nm. Concentration of $Ni(acac)_2$ was 0.1 mmol/L.

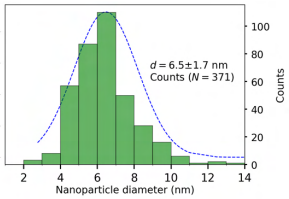

(d) Size distribution of Ni nanoparticles with a mean particle diameter of 6.5 ± 1.7 nm. Concentration of $Ni(acac)_2$ was 0.1 mmol/L.

Figure A.8: Overview of size distributions of various Ni colloids synthesized by varying $Ni(acac)_2$ concentration in the growth solution.

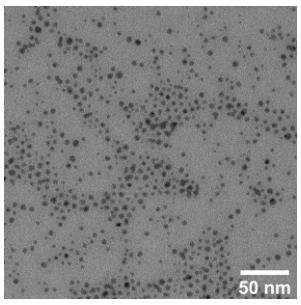

(a) TEM image of Ni nanoparticles with a mean particle diameter of 6.7 ± 1.7 nm. Concentration of $Ni(acac)_2$ was 0.1 mmol/L. $Ni(acac)_2$ growth/seeds ratio = 1. Figure A.10a shows the corresponding size distribution.

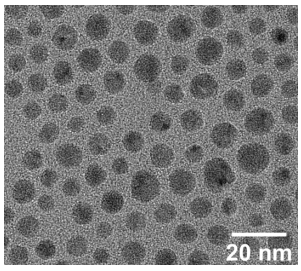

(b) TEM image of Ni nanoparticles with a mean particle diameter of 6.5 ± 1.7 nm. Concentration of $Ni(acac)_2$ was 0.2 mmol/L. $Ni(acac)_2$ growth/seeds ratio = 2. Figure A.10b shows the corresponding size distribution

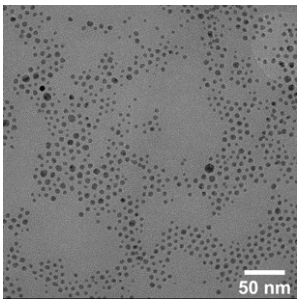

(c) TEM image of Ni nanoparticles with a mean particle diameter of 6.1 ± 1.3 nm. Concentration of $Ni(acac)_2$ was 0.20 mmol/L. $Ni(acac)_2$ growth/seeds ratio = 3. Figure A.10c shows the corresponding size distribution

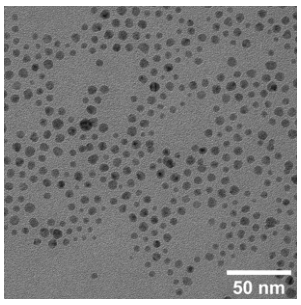

(d) TEM image of Ni nanoparticles with a mean particle diameter of 7.1 ± 1.1 nm. Concentration of $Ni(acac)_2$ was 0.20 mmol/L. $Ni(acac)_2$ growth/seeds ratio = 4. Figure A.10d shows the corresponding size distribution

Figure A.9: Overview of size distributions of various Ni colloids synthesized by varying $Ni(acac)_2$ amount in the growth solution compared to the $Ni(acac)_2$ used to synthesize the Ni seeds.

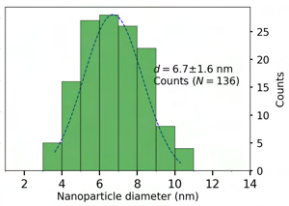

(a) Size distribution of Ni nanoparticles with a mean particle diameter of 6.7 ± 1.7 nm. Concentration of $Ni(acac)_2$ was 0.1 mmol/L. $Ni(acac)_2$ growth/seeds ratio = 1.

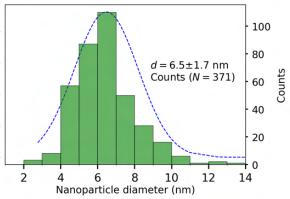

(b) Size distribution of Ni nanoparticles with a mean particle diameter of 6.5 ± 1.7 nm. Concentration of $Ni(acac)_2$ was 0.2 mmol/L. $Ni(acac)_2$ growth/seeds ratio = 2.

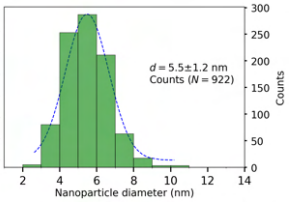

(c) Size distribution of Ni nanoparticles with a mean particle diameter of 6.1 ± 1.3 nm. Concentration of $Ni(acac)_2$ was 0.20 mmol/L. $Ni(acac)_2$ growth/seeds ratio = 3.

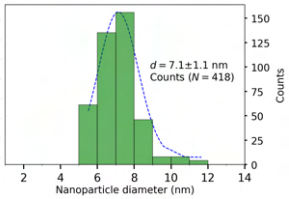

(d) Size distribution of Ni nanoparticles with a mean particle diameter of 7.1 ± 1.1 nm. Concentration of $Ni(acac)_2$ was 0.20 mmol/L. $Ni(acac)_2$ growth/seeds ratio = 4.

Figure A.10: Overview of size distributions of various Ni colloids synthesized by varying $Ni(acac)_2$ amount in the growth solution compared to the $Ni(acac)_2$ used to synthesize the Ni seeds.

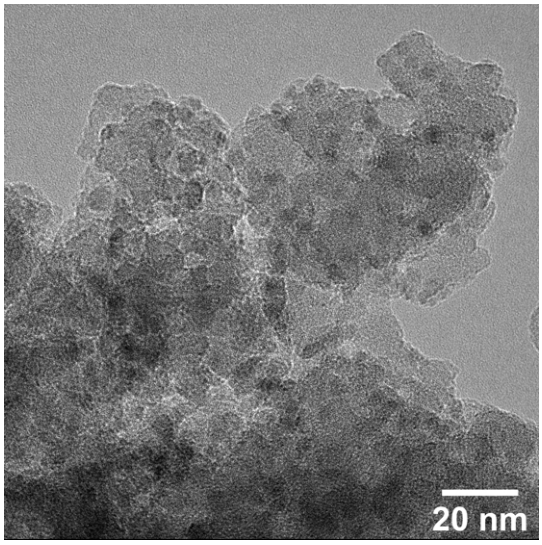

(a) TEM image of Ni NPs on SiO_2. Particles appear well-distributed across the support.

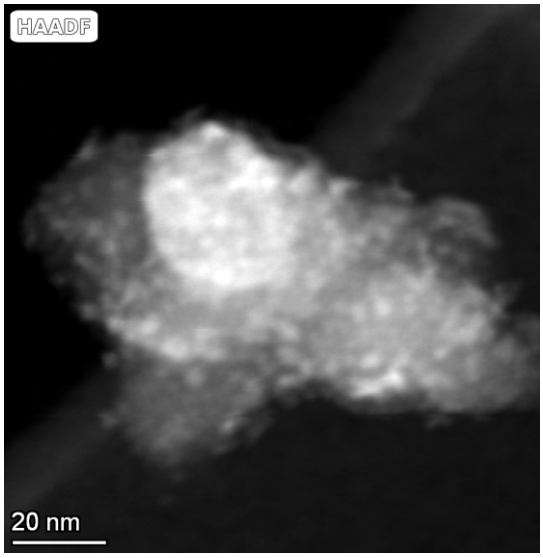

(b) HAADF-STEM image of Ni NPs on SiO_2. A Ni agglomerate is observed. This region was used for EDX-imaging.

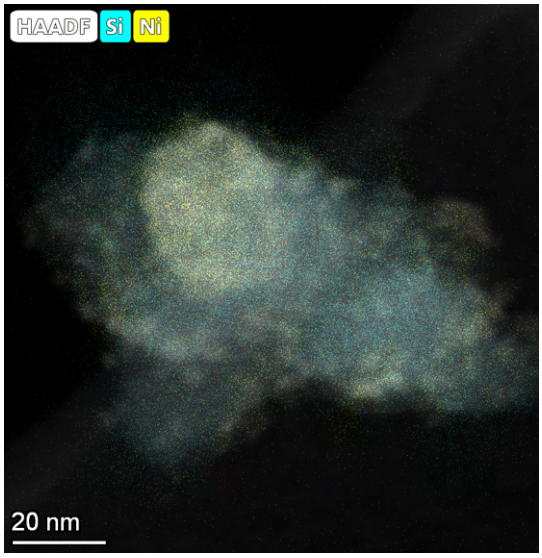

(c) EDX mapping of the HAADF-STEM image of the region presented in Figure A.11b. Blue indicates Si, and yellow indicates Ni. An agglomerate of Ni is found, indicating an inhomogeneous distribution of Ni across the sample.

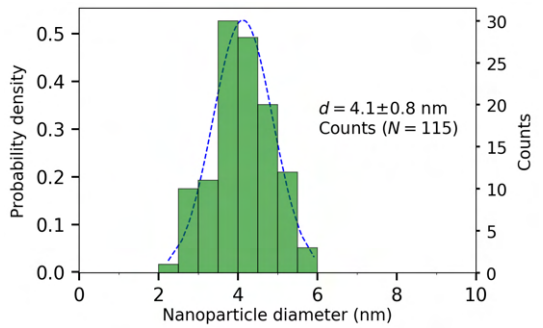

(d) Size distribution of Ni/SiO_2 with an average diameter of 4.1 ± 0.8 nm.

Figure A.11: TEM and HAADF-STEM images of 4.1 ± 0.8 nm Ni/SiO_2 with a Ni wt-% of 0.6 % prepared through a slow-evaporation method. wt-% is calculated according to Equation (2.1). The corresponding TPR profile is shown in Figure A.19.

101

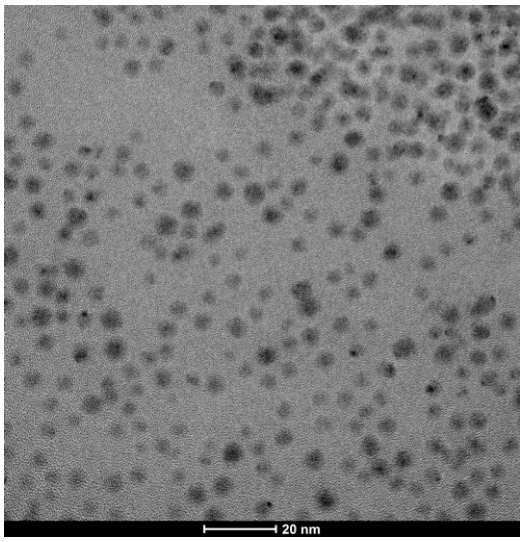

Figure A.12: TEM image of Ni colloids in toluene. Sample was made by hot-injection with BTB (Section 2.1.2) at 90°C. Monodisperse Ni nanoparticles with a mean size of 4.2 ± 0.4 nm are found.

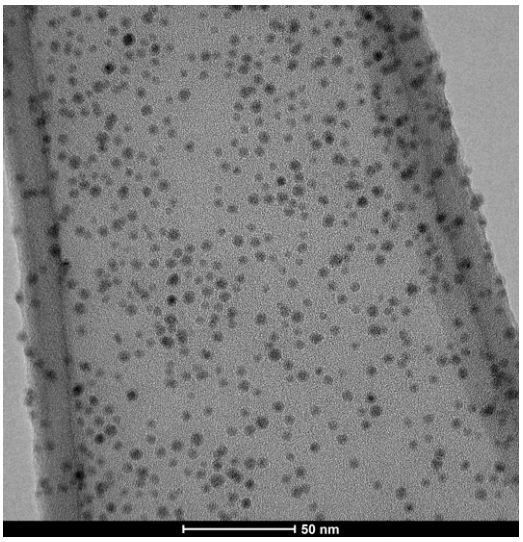

Figure A.13: TEM image of Ni colloids in toluene. Sample was made by hot-injection with BTB (Section 2.1.2) at 90°C. Monodisperse nanoparticles with a mean size of 4.5 ± 0.8 nm are found.

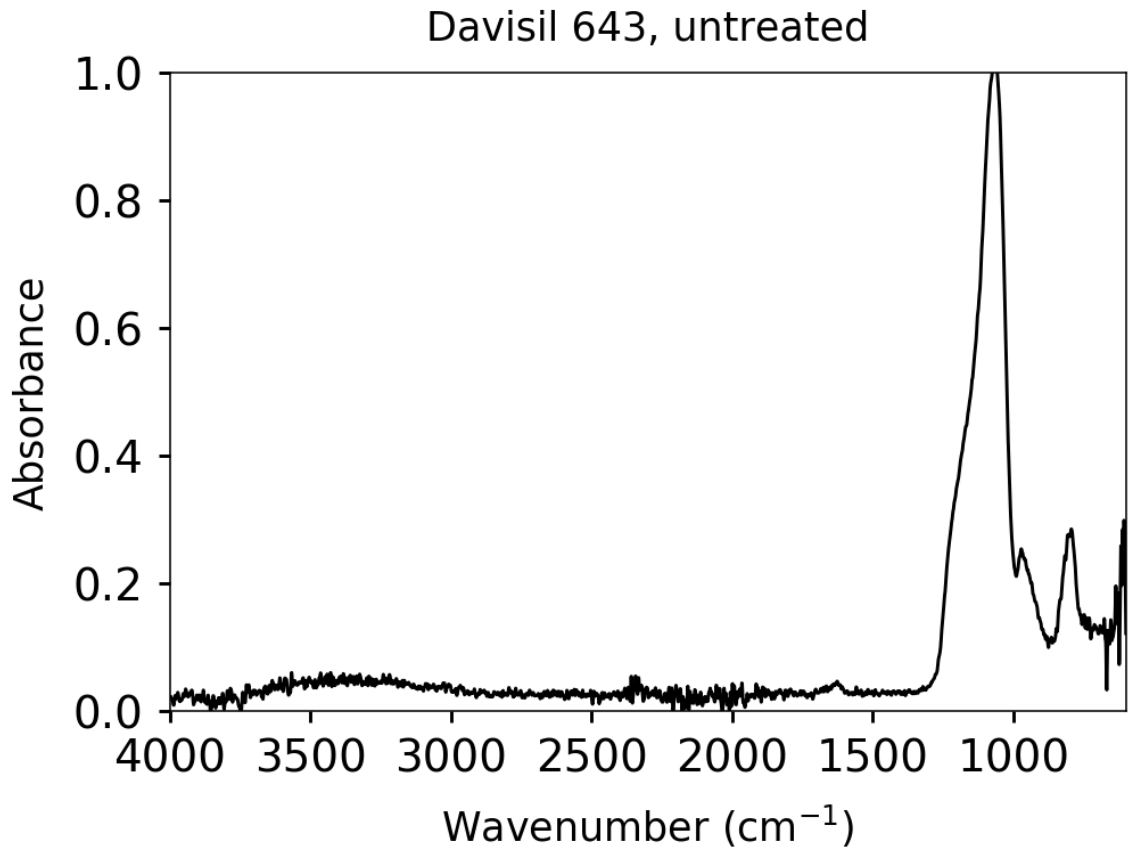

Figure A.14: IR spectroscopic data of untreated Davisil 643 SiO_2 support.

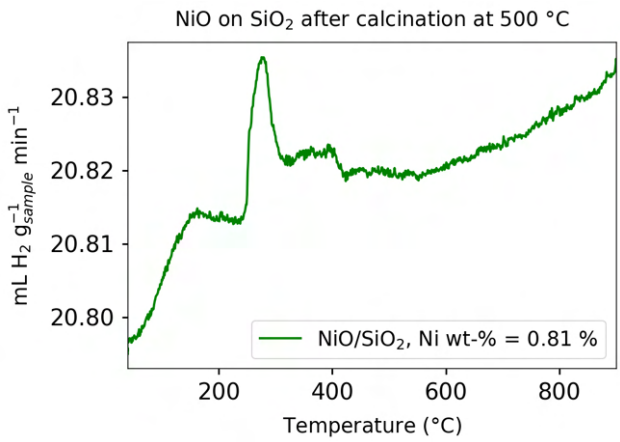

Figure A.15: TPR profile of 8.8 ± 2.7 nm Ni nanoparticles supported on SiO_2 using slow-evaporation.

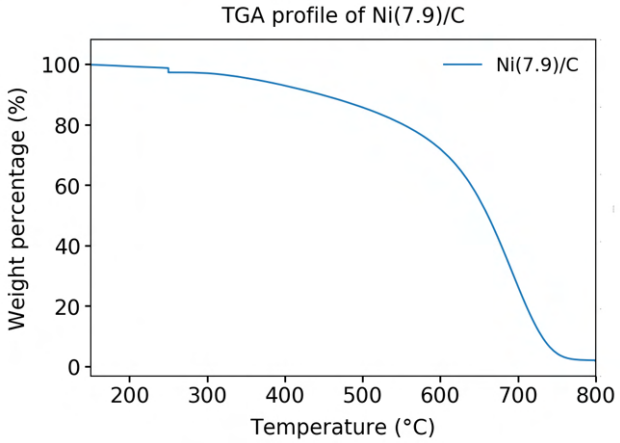

Figure A.16: TGA profile of 7.9 ± 2.3 nm Ni nanoparticles supported on carbon using slow-evaporation. Relative mass loss was investigated at a large range of temperatures in O_2.

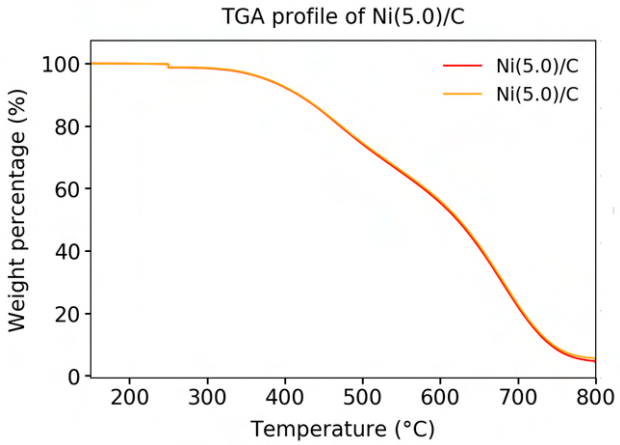

Figure A.17: TGA profile of 4.9 ± 0.8 nm Ni nanoparticles supported on carbon using sonication-assisted deposition. Relative mass loss was investigated at a large range of temperatures in O_2.

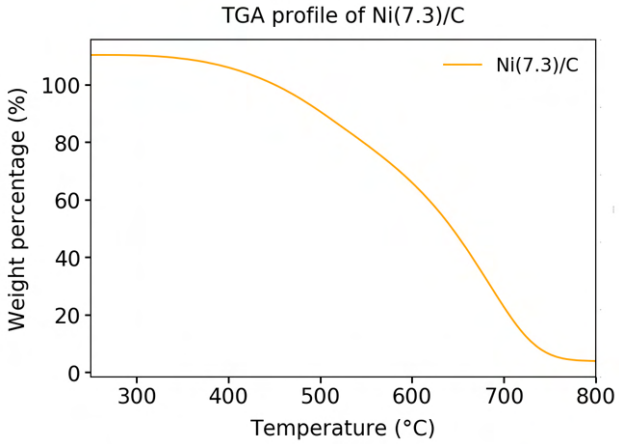

Figure A.18: TGA profile of 8.0 ± 1.7 nm Ni nanoparticles supported on carbon using sonication-assisted deposition. Relative mass loss was investigated at a large range of temperatures in O_2.

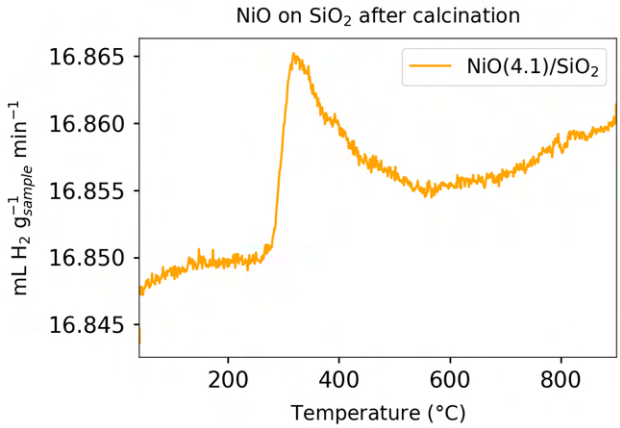

Figure A.19: TPR of 4.1 ± 0.8 nm Ni/SiO_2 with a Ni wt-% of 0.6 % prepared through slow-evaporation method. wt-% is calculated according to Equation (2.1).

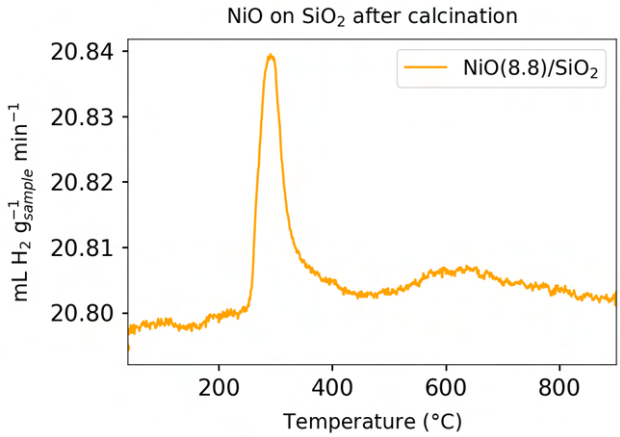

Figure A.20: TPR of $NiO(8.8)/SiO_2$ prepared through sonication-assisted deposition with a Ni wt-% of 0.69 %. Ni wt-% is calculated according to Equation (2.1).

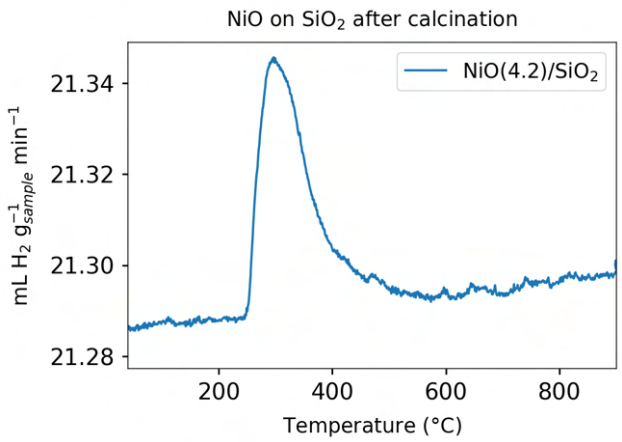

Figure A.21: TPR of NiO(4.2)/SiO_2 through sonication-assisted deposition with a Ni wt-% of 1.51 according to ICP-OES and a Ni wt-% of 1.96 % according to TPR. Ni wt-% is calculated according to Equation (2.1).

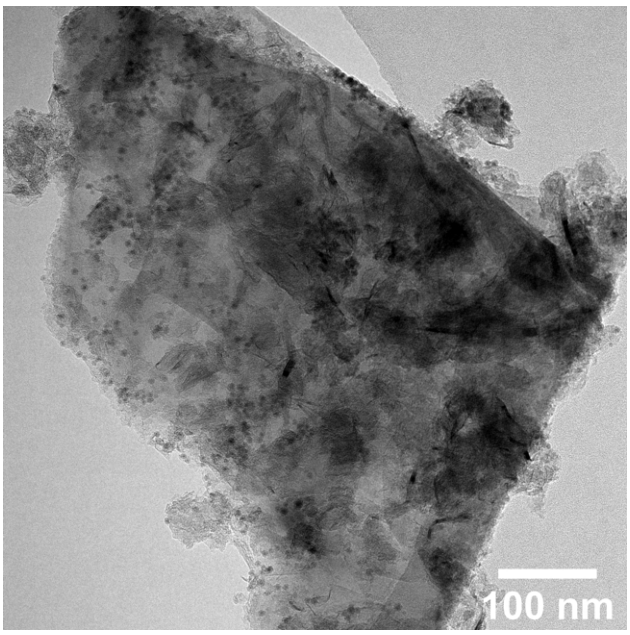

Figure A.22: TEM image of Ni/C prepared through sonication-assisted deposition by first adding toluene and sonicating.

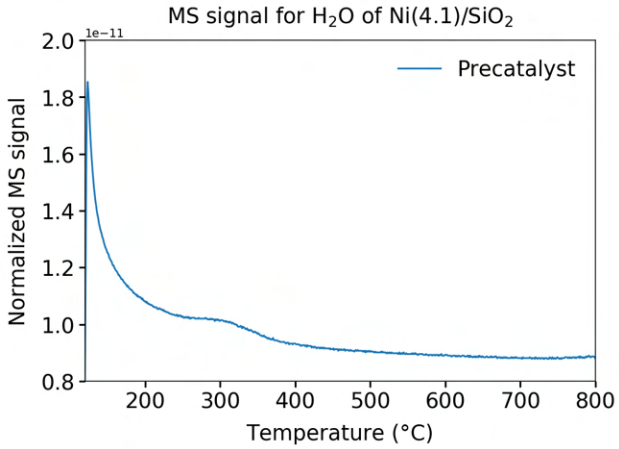

Figure A.23: MS signal for H_2O of untreated Ni(4.1)/SiO_2 with a Ni wt-% of 0.60 %. Initial peak corresponds to evaporation of the majority of water, with subsequent signal corresponding to the evaporation of water from the pores.

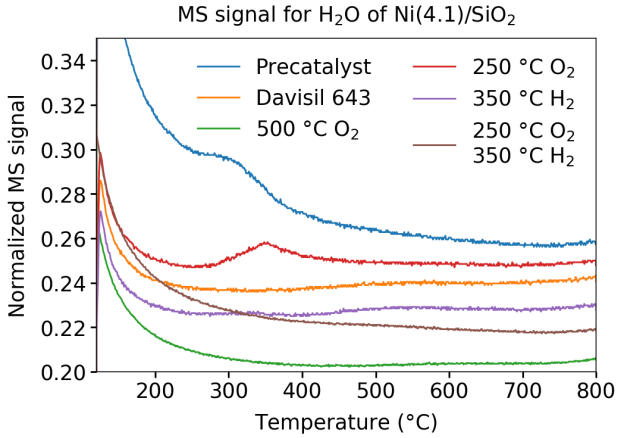

Figure A.24: MS signal for H_2O of untreated Ni(4.1)/SiO_2 with a Ni wt-% of 0.60 %. Initial peak corresponds to evaporation of the majority of water, with subsequent signal corresponding to the evaporation of water from the pores.

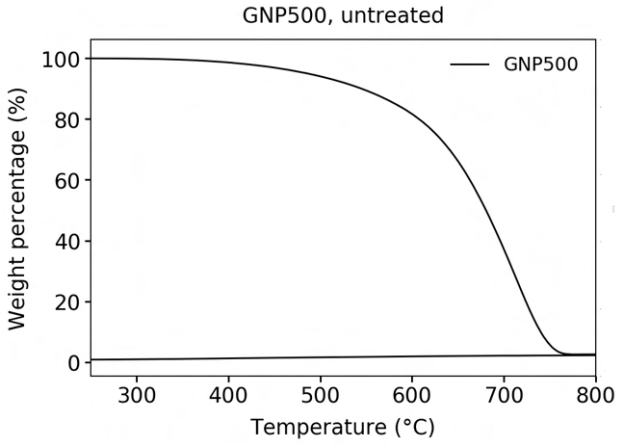

Figure A.25: TGA profile of untreated GNP500 carbon support material in O_2.

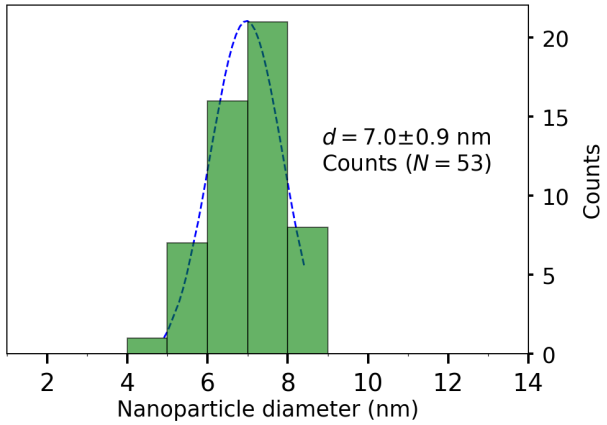

Figure A.26: Size distribution of Ni(7.0)/SiO_2 synthesized using TOP after calcination at 500 °C in O_2 for 2 h and reduction in H_2 at 350 °C for 2 h.

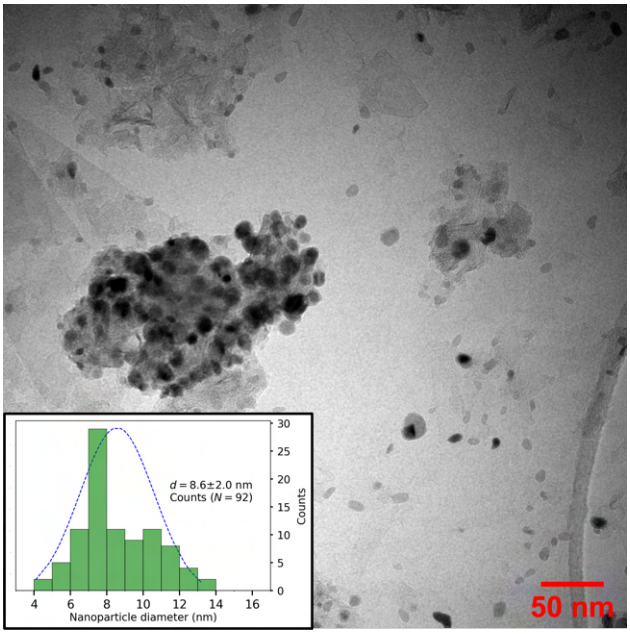

Figure A.27: Ni(8.6)/C after calcination at 250 °C in O_2 for 2 h and reduction in H_2 at 350 °C for 2 h. Ni wt-% was 4.1 %.

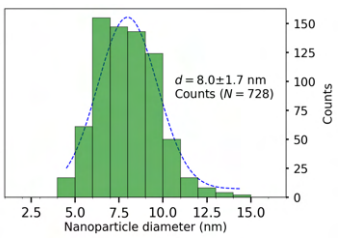

(a) Ni/C, corresponding Figure 4.16c.

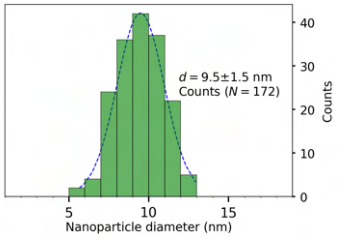

(b) NiO/C, corresponding to Figure 4.16b.

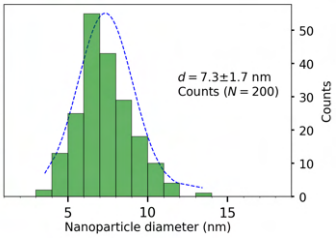

(c) Ni/C, corresponding to Figure 4.4.

Figure A.28: Size distributions of Ni/C with a Ni wt-% of 2.7 %. a) Precatalyst, b) after calcination at 250 °C in O_2 for 2 h and c) after calcination at 250 °C in O_2 for 2 h and after reduction at 350 °C in H_2 for 2 h.

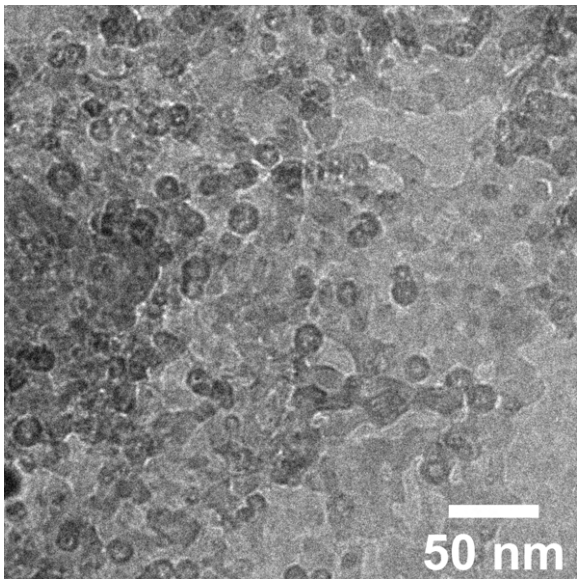

Figure A.29: TEM image of the region shown in Figure 5.3 directly after the *in situ* oxidation experiment. The deteriorated carbon was thought to be caused by the interaction of water with the high energy electron beam with the support material. Water might adsorb to the carbon material when it was again brought under vacuum by being pulled through small leaks in the *in situ* gas cell. This in turn could have had a destructive influence on the carbon material.

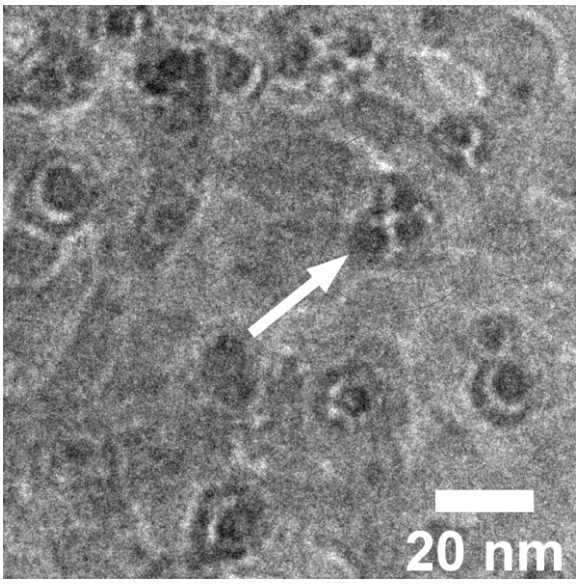

Figure A.30: TEM image of Ni/C after *in situ* TEM reduction experiment following the *in situ* oxidation experiment shown in Figure 5.3. The sample was heated to 350 °C at a rate of 0.1 °C/s. The image shown here was taken after 70 minutes. The particles shown here all still show a Ni spot on the inside of a shell material and remained hollow. This is in stark contrast to the *ex situ* result shown in Figure 5.2c and the *in situ* experiment shown in Figure 5.4. Some particles appeared to have multiple Ni spots present at the inside of the shell.

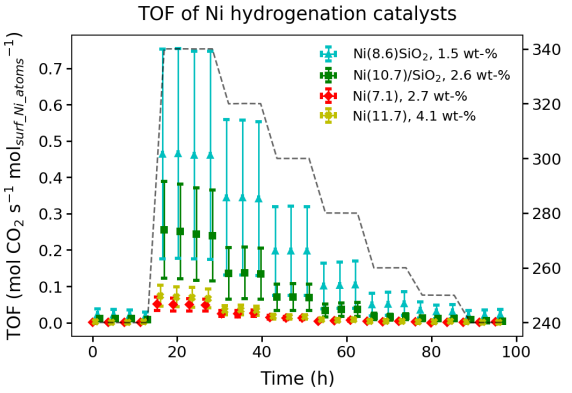

Figure A.31: Turnover frequencies of various catalysts. Large errorbars due to uncertainty in particle diameter make it difficult to compare catalysts in this manner. Reaction conditions: GHSV = 6000 mL g^{-1} h^{-1}, p = 30 bar, reaction mixture (in vol-%) = 5 % He, 75.64 % H_2 and 19.36 % CO_2. Temperatures ranged from 240 °C up to 340 °C, as indicated by the dotted black line.

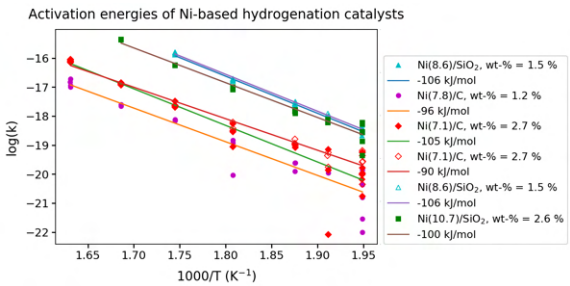

Figure A.32: log(k) vs 1/T plot to determine activation energies of various tested catalysts at conversions below 50 %. Ni/C and Ni/SiO_2 show similar activation energies. Reaction conditions: GHSV = 6000 mL g^{-1} h^{-1}, p = 30 bar, reaction mixture (in vol-%) = 5 % He, 75.64 % H_2 and 19.36 % CO_2. Temperatures ranged from 240 °C up to 340 °C.

108

List of Tables